OXIDATIVE MOLECULAR LAYER DEPOSITION OF REDOX-ACTIVE THIN-FILM POLYMERS

A Dissertation

presented to

the Faculty of the Graduate School

at the University of Missouri-Columbia

In Partial Fulfillment

of the Requirements for the Degree

Doctor of Philosophy

---

by

QUINTON K. WYATT

Dr. Matthias J. Young, Supervisor

DEC 2022

The undersigned, appointed by the dean of the Graduate School, have examined the dissertation entitled

OXIDATIVE MOLECULAR LAYER DEPOSITION OF REDOX-ACTIVE THIN-FILM POLYMERS

presented by Quinton K. Wyatt,

a candidate for the degree of Doctor of Philosophy in Chemistry,

and hereby certify that, in their opinion, it is worthy of acceptance.

Professor Matthias J. Young

Professor Gary Baker

Professor Wesley Bernskoetter

Professor Reginald Rogers

Professor Matthew Maschmann

ACKNOWLEDGEMENTS

I would like to acknowledge my advisor, Matthias J. Young, who made all this work possible. His guidance and advice carried me through all the stages of research and writings for all my academic projects. I would also like to thank my committee members for letting my defense be an enjoyable moment, and for your brilliant comments and suggestions, though-out my academic career here, at University of Missouri.

TABLE OF CONTENTS

LIST OF ILLUSTRATIONS

OXIDATIVE MOLECULAR LAYER DEPOSITION OF REDOX-ACTIVE THIN-FILM POLYMERS

Quinton K. Wyatt

Dr. Matthias J. Young, Thesis Supervisor

ABSTRACT

Thin film materials research for a more sustainable future is growing rapidly and new techniques for depositing these films are beginning to surface. One such technique is highlight in this body of work using gaseous precursors to grow bottom-up molecularly controlled polymers, Oxidative molecular layer deposition (oMLD). oMLD promises to enable molecular-level control of polymer structure through monomer-by-monomer growth via sequential, self-limiting, gas-phase surface reactions of monomer(s) and oxidant(s). However, only a few oMLD growth chemistry's have been demonstrated to date and limited mechanistic understanding is impairing progress in this field. Here, we establish key insights into the surface reaction mechanisms underlying oMLD growth. We identify the importance of a two-electron chemical oxidant with sufficient oxidation strength to oxidize both a surface and a gas-phase monomer to enable oMLD growth. The mechanistic insights we report will support rational molecular assembly of co-polymer structures to starkly improve the electrochemical capacity. This work is foundational to unlock molecular-level control of redox-active polymer structure and will enable the study of previously intractable questions regarding the molecular origins of polymer properties, allowing us to control and optimize polymer properties for energy storage, water desalination, and sensors.

Chapter 1

INTRODUCTION

1.1 Background

With the world's population steadily increasing to an estimated 8 billion people by 2025[1, 2], consumer demand for essential goods and services has heavily stressed the world's water supply[3, 4]. Only two percent of accessible water is available as freshwater[5]; less than one percent is readily processable potable water for human consumption[6]. Most of these freshwater supplies rely on steady rainfall or resupply of the water basin to keep up with continued use[7]. Water supplies that have been used for millennia are becoming highly strained around developing countries across the world. In 2014, Cape Town, South Africa, realized water usage was draining the lake that supplies fresh water (Figure 1.1, Left) to the surrounding communities. Thus they began rationing water to their citizens in a desperate attempt to prevent the absolute collapse of their civilizations[8]. With the threat of being without a fresh water supply, the local South African governments placed a countdown timer till such drastic devastation would happen entitled "Day Zero (0)". More than half of the world (¡ 50%) will be living in water-stressed areas by the year 2025[9], with 1 billion people currently without access to safe drinking water[10], spiking health issues[11] and environmental threats[12]. South African coastal regions are the hardest affected by draining water supplies (Figure 1.1, Right), while coastal access to seawater requires desalination technologies[9]. In 2014, the "Bill and Melinda Gates foundation' started funding large community projects to develop adequate housing, extensive public health programs, and water treatment for developing countries worldwide[13, 14]. Many areas are beginning to outgrow or over-consume their current supplies[15].

Most available water supplies are lakes, rivers, and groundwater, and dissolved contaminants such as micro-organisms, organics, and salts can reach higher than the recommended ppm values (500 ppm, Salts, WHO), making processing this supply difficult and energy intensive[16]. With the

remaining 98 percent of the world's water supply retained as sea or brackish (30,000 ppm, and 1,000 ppm, salt respectively) water, desalination garnered attention as a technology in need of development to address the world's water crisis[17, 18]. Saline or saline solutions refer to dissolved salt in water, so desalinating removes the salt from water, producing clean, potable water. With more communities adopting desalination as a reliable source of drinking water over the past several decades[19], but these methods can be improved with newer technologies and devices. Desalination over the years has developed into several dominant forms, with electrical, filtration/membrane, and thermal being the main contributors to the current processes[20, 21]. One of the oldest forms of water desalination is evaporative process that utilizes large water depositories or water evaporator tanks. This thermal desalination technique was among the first to be available for commercialization scale-up for more large-scale communities. This process generally uses large ponds/tanks that allow thermal energy from the sun or supplied power source to evaporate the water into purified water tanks, draining saturated salt brine and particulates into waste or runoff. Higher concentrations of contaminants or salts come higher evaporation energies causing slower production and higher energy consumption[22].

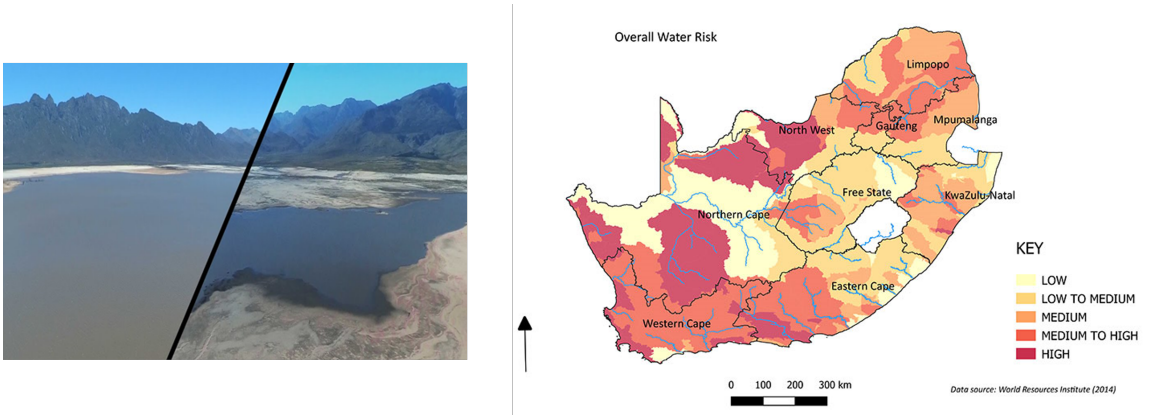

Figure 1.1: Left Figure: Image of South African water supply in 2015 (LEFT) and 2019 (RIGHT) with extreme heat and use, the supply is nearing empty, Right Figure: Map Of South African water needs with average stress levels above medium.

1.2 Current Desalination Technology

Of all desalination techniques, Reverse Osmosis (RO) is one of the most well-known desalination techniques that continuously receives new updates and improvements, which contributes to lowering the energy consumption over the desalination process. RO utilizes filters, or membranes, that require deferential pressure to push saline water through semi-permeable membranes, capturing salt

and other contaminants, as fresh water is produced on the effluent flow. This energetic process of pressure driven desalination is independent of influent salt concentrations, making RO desalination energetically ideal for high salt concentration, as seen in Figure 1.2 (left), and is one of the most widely adopted desalination processes for reliable fresh water supply [23].

Although RO is a high-volume throughput technique and is available for deployment now, thermal or mechanical energy-driven desalination techniques have native energy losses to the overall process, including energy stored in the waste brine solution[24]. New technologies are needed to increase the overall efficiency of desalination in low-cost, low-energy operations. Capacitive desalination (CDI) is an electrical desalination process that is newer than RO, with only 30 years of research and development[25]. It utilizes charged electrodes to pull charged ions out of the water (Salts: NaCl, NaNO2) and produce fresh water. The initial research and development of CDI was conducted in the 1960s and spearheaded by Blair and Murphy to develop a way to use graphite to remove salt ions from water[26].

Typically, a CDI system consists of an anode and cathode (porous carbon, graphite) with an electrolyte solution (i.e., Salts) that is controlled by a power supply (Potentiostat). When power is given to the electrodes, it creates two opposite-charged electrodes (cathode and anode), in which the ions of the same charge from the solution adsorb onto the same charged carbon electrodes and form a double layer or charge buildup. These electrostatic double layers accumulate cations and anions on the cathode and anode. Once the electrodes are saturated with ions, the feed water can be released, and the charged plates can have a voltage polarity swap, repelling the charged ions back into the solution. This voltage shift allows for a significant portion of the initial voltage supplied to the electrodes to be recovered and used again, increasing the overall efficiency of CDI compared to other desalination techniques [27].

Capacitive deionization cells are designed to allow water to flow through a channel, where the top and bottom of this channel are electrode materials exposed to the flowing salt water (Figure 1.3), or there is an ion exchange membrane separator between the water and electrodes[26]. These membranes can be ion, size or charge-dependent, allowing for enhanced adsorption of respective ions. The sides of the channel are electrically insulating (non-conductive); its thickness determines the channel size and separation between electrodes. As water is allowed to flow through the desalination channels and charge build-up occurs on the exposed porous electrode, this electrostatic double layer is equivalent to an electrochemical double-layer capacitor[28]. A graphite current collector is commonly used for its inertness to reactions and to provide electrode materials with the necessary charge current to supply active material exposed to saline solution. As the saline solution flows in the channel between the

two electrodes with applied electric fields, ions from the solution are attracted to their corresponding opposite-charged fields. These ions are removed from the solution until the cell is discharged or the potential difference between electrodes subsides. The effluent (exiting water) from this CDI process is partially deionized compared to the influent feed water. This effluent can be recycled over and over to bring deionization down further or further processing. The charged electrodes can then be discharged (i.e. battery cell), recovering energy from stored faradaic interactions with ions and allows for future cycling of the cell[27].

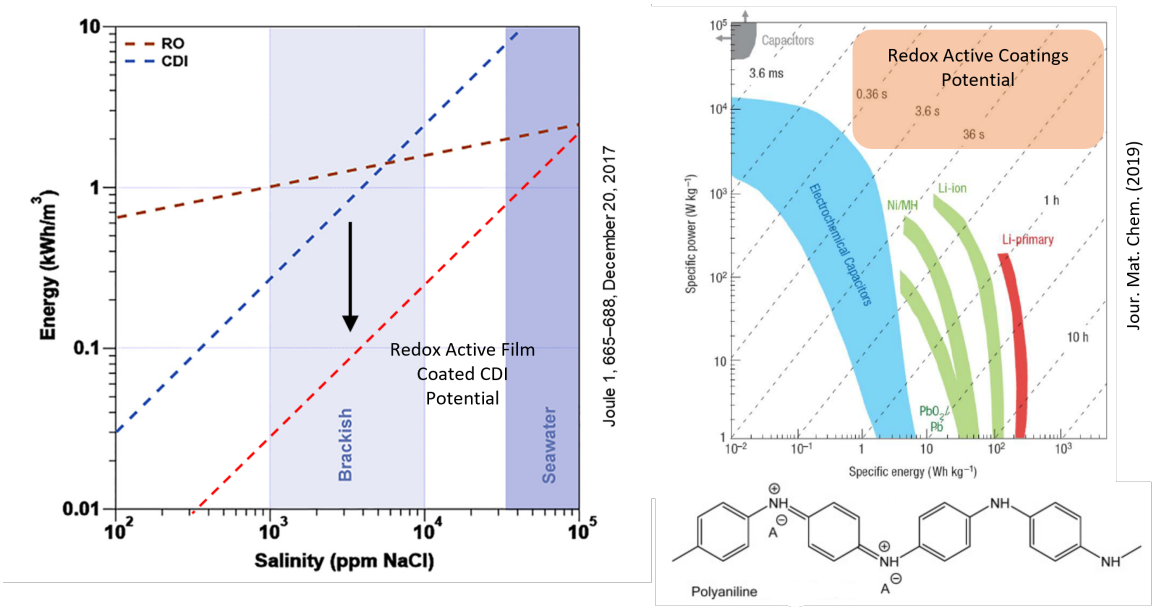

Figure 1.2: Figure Left: Graph of energy versus salinity for reverse Osmosis (Maroon) and CDI (Blue) systems, where RO outperforms CDI for high salinity concentrations. Red Dashed line indicates potential of improving efficiencies of CDI using redox active conducting polymers. Figure Right: Ragone plot comparing previously reported materials and the potential for increased charge rates and capacities with redox active polymer coating.

The regeneration of the electrode material allows CDI processes to be more energy-efficient system overall than that of RO[26]. Current CDI technologies' main limitations fall on efficient desalination of high-volume sea/saline water. Electrode capacities for the feed water concentration overwhelm CDI systems utilizing current technology. Use of CDI with lower concentrations of saline water (i.e. brackish) for desalination is more energy efficient than RO. RO desalination process, although sustainable and increasingly more efficient, the energy demand of an RO system is vastly more significant, with little ways to recover lost energy because of disposal of this stored energy in the form of high salt brine's [24]. With enhancements to current CDI technology (dashed red line, Figure 1.2, Left), the desalination process could help improve the RO process's lost energy[29]. In addition, materials for CDI development will bring higher energy density and power output for rapid charge

storage, as illustrated in Figure 1.2 (Right). Mechanical/thermal desalination has native, built-in, energy losses[23] that compares to the relationship found between internal combustion engine (ICE) and fuel cells (FC). ICE's main energetic losses come from moving mechanics and energy loss to surrounding system environment, whereas FC are an all-in-closed single unit allowing direct energy conductance with minimal energy losses[30]. Making CDI a fast-growing research field in recent years for enhancing desalination efficiency and output to match or supersede RO's current state.

1.3 Capacitive Deionization

Electrode materials in a typical CDI device consist of porous electrodes with various porosity densities for overall surface area control. These carbon-based electrode materials derive their capacities from the available surface area in the pores to enhance the electrostatic double layer capacity and thickness of this active layer exposed to feed solution, as seen in Figure 1.3. With the goal of CDI to maximize the uptake of ions from solution, there have been many attempts to enhance these two (2) components, surface area, and thickness. Changes to the pore sizes of the carbon electrode come with changes to the surface area. These pore sizes can begin hindering ion mobility due to the size restriction of ions diffusing. This distribution in size dramatically limits the rate of charging and energy needed to charge the system completely. Electrodes with high ion diffusion limitations also have slow charge/discharge rates restricting the rate of flowthrough and processable feed water. Functionalization of carbon electrodes have produced increased capacities of 300 F/g, compared to 100 F/g standard carbon CDI electrodes[31].

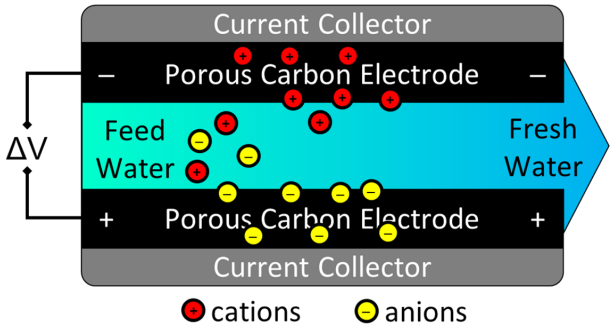

Figure 1.3: Depiction of CDI flow cell device, where feed water (saline solution) passes over porous carbon electrodes with an applied voltage, binding ions from solution. once cell is fully charged the resulting water leaves the cell as fresh water.

To achieve efficiencies and high-volume flow through on the scale of RO, and other technologies, current CDI technologies need to be more energy efficient and cost- effective way of desalinating saline water greater than brackish concentrations. The improvements to CDI enhancement come in two forms: improving the capacitive behavior of these electrode materials for faster and more efficient charge storage or modifying operating systems surrounding the material and desalinating process[32].

With the active electrode surface being the most important for direct molecular action and rates, this dissertation will focus on improving this active material layer to enhance charge capacities and rates for CDI desalination porous electrodes. Carbon-based electrodes such as activated carbon, carbon aerogel and 3D graphene are commonly used in CDI electrode materials[33]. Although these carbon-based electrodes have high surface areas for high capacities, they can be costly and complicated to produce on a larger scale [34]. Reduction of electrode cost and enhancement in activity and capacity is of importance for CDI development. Functionalizing these porous electrodes with organic-based functional groups capable of covalent interactions with a substrate for long-term stability, with enhanced material capacities, are a possible route to reach the long-term implementation of CDI worldwide.

1.4 Reduction-Oxidation (Redox Activity)

Organic-based functional groups, such as ketones (R=O) and amines (R-NH2), have electrochemical properties that allow them to be oxidized and reduced, creating negatively charged ketones ($R-0^-$) and positively charged amines ($R-N^+H2$). These organic functional groups can functionalize electrode materials for enhanced faradic ion charge storage capacities compared to an electrostatic double layer on a carbon surface[35]. Many organic functional groups capable of these charged states have oxidation and reduction potentials within the electrochemical limits of waters, before H_2 or O_2 generation, as seen in Figure 1.4. For CDI desalination to be a viable means for high volume fresh water supply, all activity of the materials in the system must be within the splitting potentials of water under an applied voltage. Water has a stable electrochemical potential window between 1 and -1, depending on the pH of the feed water[36]. Seawater and brackish water are slightly basic (8.1 pH)[37], and the feed water oxidation potential window is between -0.5 V and 0.8 V vs SHE[36]. Materials with organic functional groups with oxidation and reduction potentials between the redox limits of sea water make suitable electrode enhancement materials. These functional group can even be conformally coated

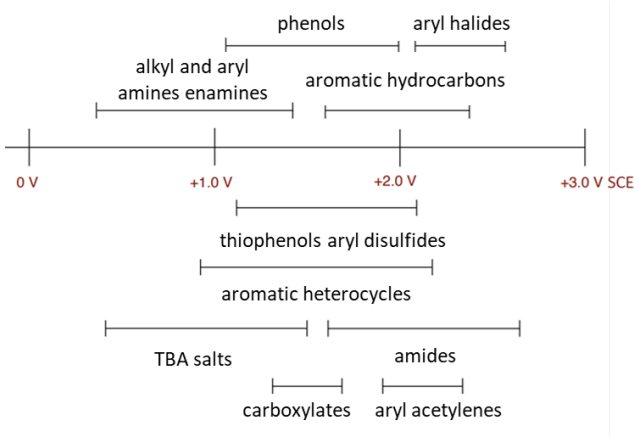

Figure 1.4: Oxdiation potentials of organic molecules and functional groups capable of redox activity.

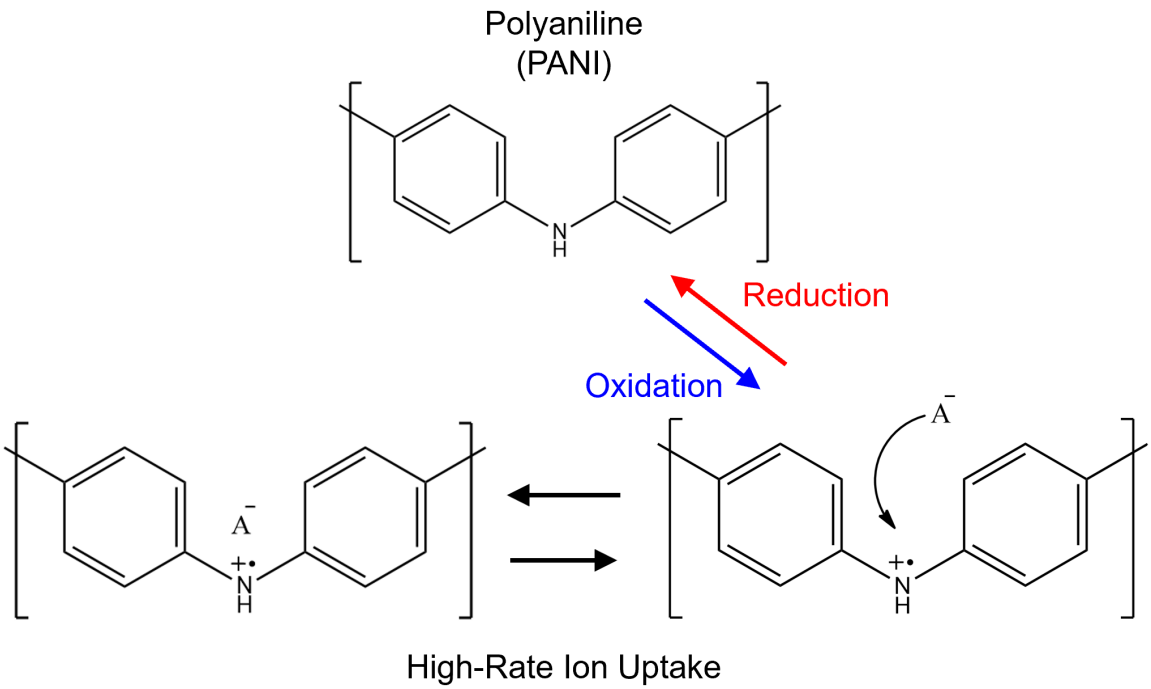

Figure 1.5: Scheme depicting Oxidation and reduction of poly(aniline) with rapid electrostatic ion uptake

onto

porous substrates already in use and theoretically enhance electrode performance. Figure 1.5 depicts a coating scheme for CDI electrode materials with redox-active functional materials for enhanced desalination performance. These redox active functionalized coatings can be deposited only molecules thick or thicker bulk materials, becoming the main active layer of the CDI process[38]. These new reduction-oxidation films can continuously be grown thicker for higher capacities, with max thicknesses between 850-1200 nm thick, while optimal thicknesses of redox active films are below 100 nm[39]. By increasing the thickness of active material, the capacity scales proportionally to the ion mobility and diffusion limitations; energy is lost during constant adsorb/desorb of already bound ions and heat generation[40].

Thus, adjusting the thickness of active material alone is not enough to overcome all obstacles. However, depositing a thin film material with high energy densities (redox) and capacitive charge storage behavior along with thickness control can ultimately reach these goals[39]. Redox-active materials use less material (nanoscale) for faster charging (Capacitive Behavior) and higher energy efficiency. Inorganic (metal oxide) redox materials previous use in CDI devices have been known to degrade over time as the crystalline ionic structure slowly dissolves away as lattice structures rearrange

to permit ion transport in and out of the structure[41]. Thus, making them less ideal for a sustainable desalination process. Redox-active organic functional groups allow for stable covalent bonds between material and substrate support. In order to create a high energy-dense network of a functional group capable of binding ions of the specific charge, these functionalities need to be connected for the lowest energy losses and mobile electron transport. Incorporating these functional groups while electronically connected led to the development of redox active conjugated conductive polymers such as Polyaniline, polypyrrole, and thiophene for desalination applications. These polymers are monomer units with functional groups with active oxidation and reduction sites to form positively or negatively charged species for ion absorption[35]. Depending on the functional group and molecular environment, Nitrogen (N) and oxygen (O) are the active redox centers of each monomer unit. These functional groups tend to be most favorable in forming positively and negatively charged electrodes for CDI desalination. With N and O being so abundant, their availability as redox-active polymers is in plentiful supply. Determining the polymer material for desalination devices and depositing this active material unto carbon supports is a momentous task. The redox potentials of the organic functional groups can change drastically depending on the surrounding molecular environment, making growing films onto 3D substrates challenging[42].

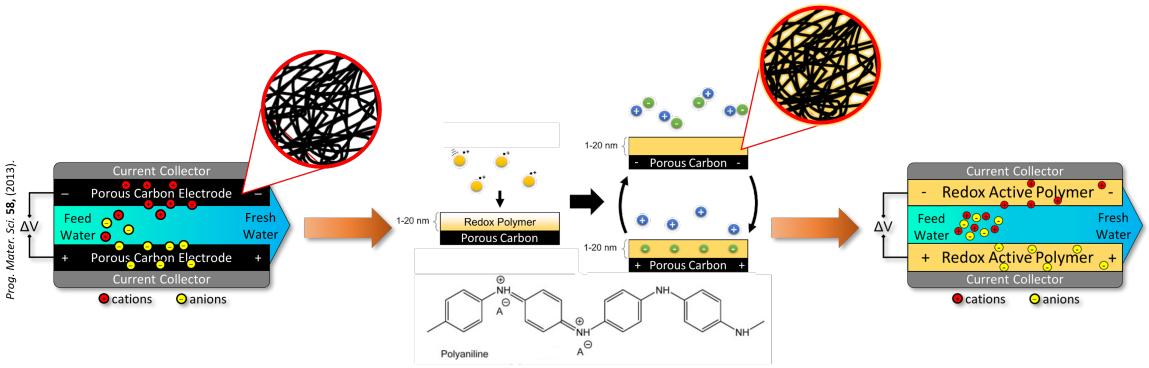

Figure 1.6: Scheme depicting CDI porous carbon electrode systems (left), growth of conformal redox active thin-film polymer using oMLD for capacitive charge storage (middle), and implementation of these redox active polymers into desalination CDI devices

Gas phase coating chemistry's have been used for decades in industrial space for developing new films and coating for semi-conductor and sensor manufacturing. Gas phase coating allows for pristine films/coating that are conformal, uniform, and pinhole free on 3D substrates and structures. One such technique for counting films in such ways is oxidative molecular layer deposition which can be used in conjunction with redox-active polymers for coating electrode material[43].

1.5 Atomic/Molecular Layer Depostion (ALD/MLD)

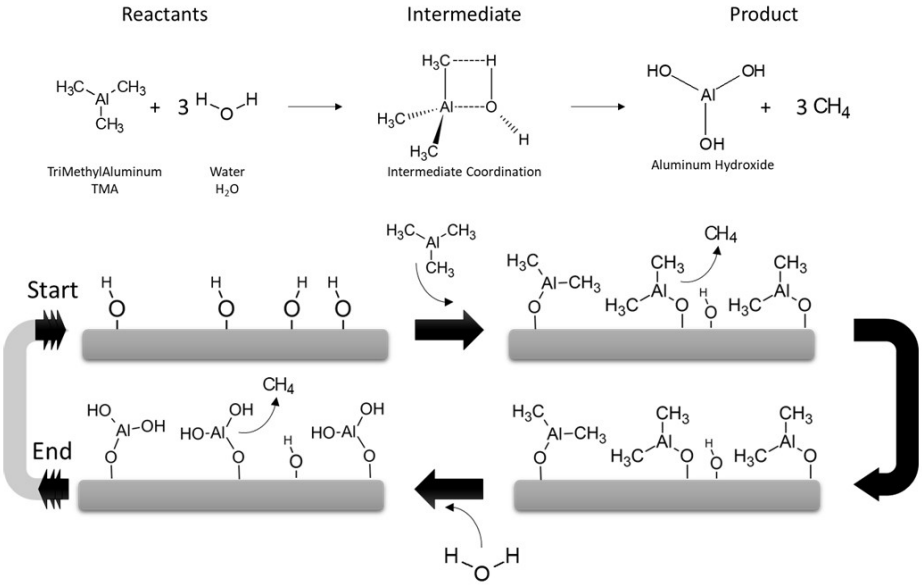

Figure 1.7: SEM image produces by S.M. George of conformal aluminum oxide (bright, upper) coating of 3D substrate (dark, lower).

Atomic layer deposition (ALD) is a leading gas phase technique for depositing thin film materials like metal oxides (i.e., AlO2) with high precision thickness control and conformal, pinhole-free coatings, as observed in Figure 1.6. ALD is a surface reaction technique that reacts with hydroxyls (-OH) or defects in material that allows for tightly packed formation during film growth. Chemicals typically used for depositing films via ALD are highly energetic and unstable under atmospheric conditions, i.e., Trimethylaluminum (TMA); thus, these chemicals need special treatment and containment for experimentation. ALD uses sequential doses of chemical gas followed by purge gas to prevent reactions with other dosing chemicals. For example, in the growth of aluminum oxide (AlO2) via ALD, two chemicals are dosed sequentially. The development of AlO2 utilizes water (H2O) and TMA that are dosed sequentially with a career gas purge between each chemical dose. A typical ALD cycle of AlO2 with TMA and Water is 1s dose followed by 10 seconds argon purge. Since this deposition technique is a surface reaction technique, TMA when first dosed, reacts with available OH or other function defects, as seen in the figure, replacing the methyl groups on aluminum with hydroxyls. With TMA having such high reactivity and affinity to oxygen, the reaction on the substrate surface is spontaneous, needing only to purge produced methane gas from TMA reaction with OH. Water can then be dosed after this purge period to remove the remaining methyl from aluminum centers

and to replace them with OH for further reactions with TMA. This cycle of TMA:purge:Water:Purge can be repeated, growing aluminum at a rate of 114 per cycle. This atomic placement of aluminum and oxygen is slow but controllable atomic level[44].

For faster deposition of films, the control needs to be shifted to the molecular scale. With molecular scale control, you can place already synthesized molecules, such as p-benzoquinone and p-Phenylenediamine, with the same benefits of ALD just in molecular layer deposition (MLD). MLD utilizes stored energetics between two molecules to spark the reaction to completion, like that of a Schiff base reaction between p-benzoquinone (pBQ) and p-Phenylenediamine (pPDA). This purposed reaction would look similar to ALD TMA:H2O reactions scheme (TMA:purge:Water:Purge) with pBQ and pPDA taking TMA and Water place, respectively. Ultimately for pure sourced, single monomer polymers to be grown via gas phase while maintaining the conformal, uniform, pinhole-free benefits of ALD and MLD for coating 3D substrates, there is an oxidative molecular layer deposition gas phase (oMLD) technique. oMLD is similar to MLD where instead of using the stored energy from both chemicals, like with pBQ and pPDA in their schiff base reaction, an oxidant is used, and only one chemical determines reaction energetics. If pBQ was replaced with oxidant [O] and then reacted with pPDA, the strength of the [O] would supply the energetics to polymerize pPDA one monomer per cycle until desired thicknesses are achieved[45].

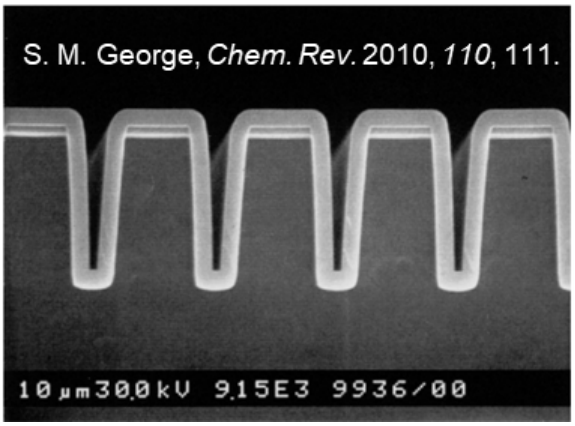

Figure 1.8: SEM image produces by S.M. George of conformal aluminum oxide (bright, upper) coating of 3D substrate (dark, lower).

1.6 Oxidative Molecular Layer Deposition (oMLD)

oMLD was first coined in 2014 by Atanasov et al.[46] when conducting oMLD gas phase chemistry with MoCl5, as the oxidant, and 3,4-ethylene dioxythiophene (EDOT), as the monomer, or molecular

unit, to grow Poly(3,4- ethylene dioxythiophene (PEDOT) on Si and Quartz rod substrates in a hot walled ALD reactor. Growth of PEDOT we observed via quartz crystal microbalance (QCM) over several temperature ranges, with the largest growth observed was for lower temperatures but higher conductivity's were observed at elevated temperatures[46]. Although PEDOT films have been deposited using other gas phase techniques such as vapor phase polymerization (VPP)[47] and chemical vapor deposition (CVD)[48], these techniques still lacked fully conformal, uniform, and pinhole-free coating for three-dimensional substrates[49]. oMLD deposited PEDOT films reached conductivity's of 5300 S cm-1 with films deposited at 150 oC, compared to 100-2500 S cm-1 in all other reported studies of gas phase deposition of PEDOT[46]. With the change in conductivity as a function of deposition temperature, x-ray diffraction (XRD) analysis of films deposited at temperatures 100 oC and 150 oC observed a higher degree of crystalline structure or long-range order of the stacking of the monomer units in the 150 oC sample[46]. With the deposition of conformal, uniform and highly conductive PEDOT films being the first to lay the groundwork for oMLD chemistry, little is known about the viability of this technique to be used on similar oxidants and monomers.

This dissertation sets the groundwork for expanding the understanding of oMLD chemistry mechanisms and the ability to expand into other polymer films. More specifically, this works to understand the effects of oxidant (MoCl5) and polymerization mechanism with hetero atoms containing aromatic conjugated monomers such as Pyrrole, Aniline, Thiophene, Furan, and EDOT. Oxidants and monomers will be sequentially dosed in the same manner as ALD chemistry allowing for controlled growth of polymer films as depicted in Figure 1.7. oMLD in this work was conducted with a lab-assembled hot-walled gas phase flow reactor, designed and built by the founding graduate students of the Matthias J. Young lab group, and a schematic of the reactor overview can be observed

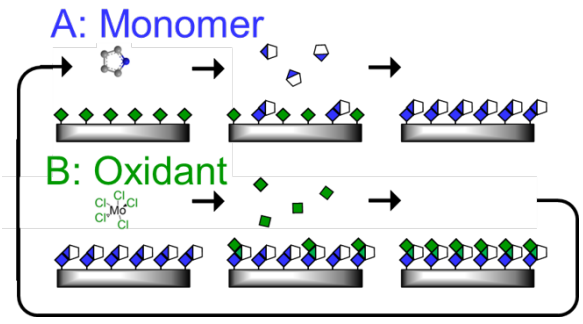

Figure 1.9: oMLD reaction scheme with representative monomer units reacting with MoCl5 as the oxidant. An oMLD reaction cycle consists of alternating AB cycles where for each cycle (A or B) there is a chemical dose followed by carrier gas purge. This AB cycles can be repeated, growing polymer chains on the molecular level.

in Figure 1.8 (Left). Chemicals such as EDOT and pBQ need to be heated to produce sufficient vapor pressures for gas phase dosing. Hot source ovens were designed to keep chemicals at elevated temperatures of 30-150 oC to allow for adequate dosing of all chemical precursors. The reactor body and hot source ovens are wrapped with voltage-regulated heat tape and monitored by LabVIEW PID controlling software to maintain consistent temperatures throughout film depositions. The reactor exhaust is equipped with a three-stage stainless steel mesh filtration system for reactor pumps and external exhaust (house exhaust) longevity. Reactor pressures for oMLD chemistry were maintained between 800-1000 mTorr with a 200 sccm flow rate of argon carrier gas through the reactor system. All chemical precursor doses were controlled with pneumatic valves set to permanently be closed unless signaled for dose regulated by the computer LabView system. The thermal gradient down the length of the reactor was maintained in three sections; chemical, reactor body, and exhaust, where chemical temperatures were held lower than that of the reactor body, and the reactor body lower than exhaust. This thermal gradient is necessary to prevent condensation of chemical precursors (i.e. MoCl5) on the reactor delivery lines causing condensation of precursors leading to uncontrollable dosing of chemicals. Many oMLD polymers films grow faster (nm/cycle) than ALD metal oxide chemistry's, so excess polymer film buildup is removed every 10-15 reactor experiments to maintain constant growth outcomes without introducing side reactions and defects.

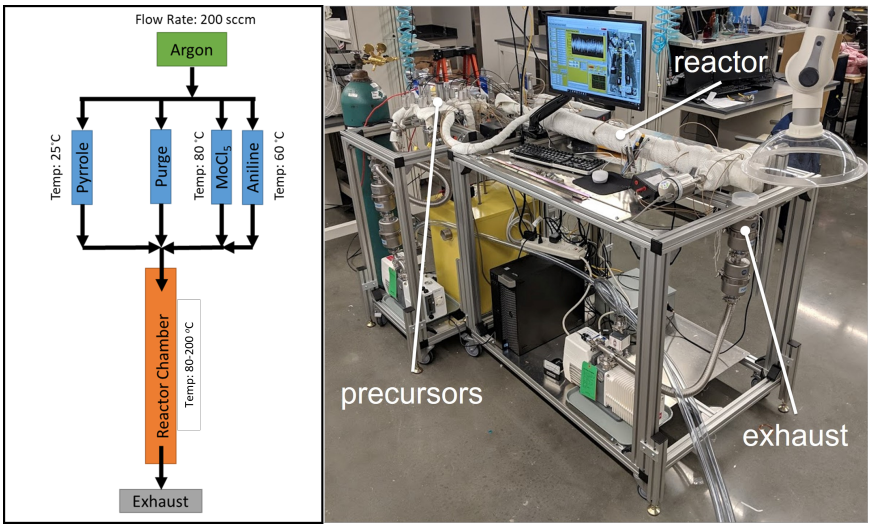

Figure 1.10: Figure Left: schematic depiction of reactor layout and flow design. Figure Right: Picture of assembled reactor and its labelled components.

1.7 oMLD Polymer Chemistry

Prior to our work in oMLD polymer chemistry, there was only one reported oMLD chemistry[46]. This previously reported work carried out by Atanasov et. al. in 2014 consisted of using ALD/MLD chemistry styled techniques with the addition of gas phase oxidant, $MoCl_5$ and was named "Oxidative Molecular Layer Deposition". With only one available study for oMLD polymer chemistry, there was limited information about: a) The mechanisms by which these polymers form/propagate, b) whether these materials have long range order or densely packed oligomers, c) the effect of materials thickness on bulk properties, and d) deposited films being redox active. Another gas phase chemical technique known for gas phase polymerization and controllable film growth is oxidative chemical vapor deposition (oCVD). oCVD uses an oxidant and monomer source, like that of oMLD, however, oCVD doses oxidant and monomer together, allowing the reactions to begin in the gas phase and transfer to the target substrate[50].

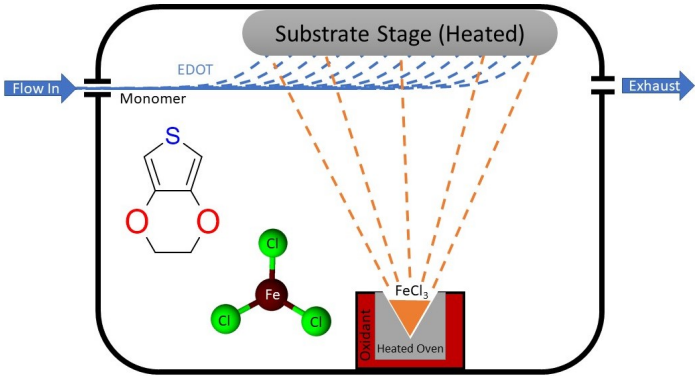

Figure 1.11: Schematic of oCVD Technique

oCVD polymer chemistries produce high quality redox active polymer films, however the bulk materials can produce high surface roughness[51], making oCVD a nonviable option for coating porous electrode materials. oMLD allows for sequential doses of oxidant and monomer where neither are dosed at the same time, even more, these doses are separated by time where argon gas purges previous chemicals from reaction chamber. this sequential dosing of precursors is made possible by heterogenous reaction conditions where gas phase precursors are reacting with bound surface species. These reactions are self-limiting, surface reactions where precursors only react with available surface sites on exposed substrate. This unique process of sequential doses of self-limiting, surface reactions, allows for molecular layer control of polymer growth with more conformal and smoother films, like that of ALD chemistry's[44]. Although oCVD has been demonstrated for other polymers, it is unclear if these polymers can be grown by oMLD chemistry.

With oMLD chemistry being a new technique for depositing polymer films, there were many unknowns needing to be addressed before future materials can be produced via oMLD. With many

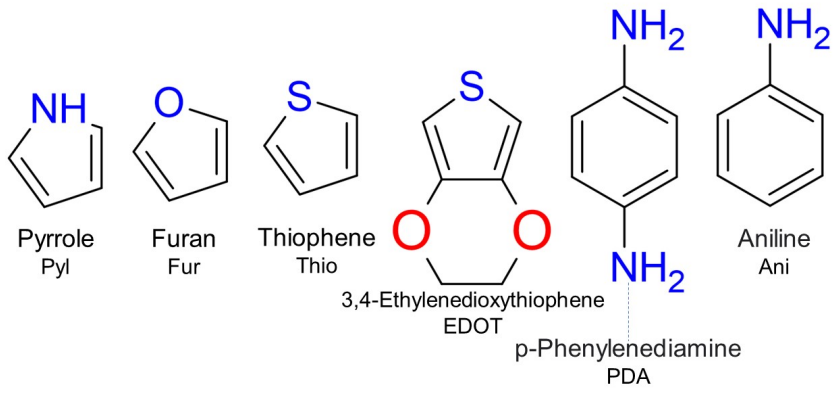

Figure 1.12: Monomers of interest for oMLD Chemistry

polymerization techniques and pathways for propagation well studied it is unclear the reaction pathway for polymer film growth for heterogeneous surface reactions in an oMLD process. Previously reported polymerization schemes observed mechanistic propagation of polymers in a homogenous environment allowing for reaction site rearrangement and continued polymer growth[52], were-as heterogenous surface reactions are static requiring more specific reactions. With oMLD utilizing sequential dosing scheme with a strong oxidant (MoCl5), and high vapor pressure monomers, the reaction pathways for polymerizing redox active films under high vacuum and temperatures are unclear. The mechanism for oMLD gas phase polymer growth is of importance as it aids in the advancement of future redox active materials and their properties. With the use of a strong oxidant and known solution phase polymer catalyst (MoCl5)[53], many reaction pathways with monomers, EDOT (S, O) and pyrrole (NH), hetero-atom centers, consisting of ring openings, aromatic saturations, and other side reactions, can be hypothesized. Understanding the role Mo(V), as an oxidant, plays in the oMLD polymerization mechanistic pathway of the controlled growth of polymer films previously reported.

Another area of interest during polymer film growth utilizing oMLD chemistry, is whether molecular layer control Is maintained throughout the entire deposition process, leading to long range communication (one continues polymer from substrate to exposed surface) in redox active polymer films with low polydispersity and low molecular weight. It is unclear if oMLD molecular layer control is maintained continuously throughout entire film growth, limiting the bulk composition of material to be comprised of short chain oligomers, that when stressed or solvated, begin to degrade the deposited film material. With the above-mentioned side reactions still possible during

oMLD film growth, the final composition of polymer films is unknown. Maintaining monomer integrity through out the film growth process provides long range redox communication throughout the entirety of the bulk polymer during electrochemical cycling. With oMLD of PEDOT being the first reported oMLD technique, it was not readily known if the deposited film maintained their redox active functionalities as in its electrodeposited form, or chemical oxidation, polymer films. As the films propagate using an oxidant, reactions such as ring opening, and saturation of conjugated systems preventing long rang control of redox moieties. Ideally films grown with oMLD technique will follow a propagation sequence like that of solution phase chemical oxidation, producing redox active polymer films without branching and dendritic polymer formation causing loss of redox response. With the length scale of redox communication and molecular layer control of oMLD processes unclear, the final properties of deposited films may be limited to thicknesses where continues molecular layer control is maintained. In this work we address the mechanistic process of oMLD polymer film growth, and its effect on deposited film structure and final redox properties.

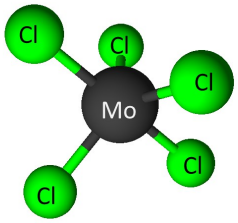

Figure 1.13: Molecular depiction of Oxidant $MoCl_5$

Our initial work, in chapter 2, focused on electrodeposition of polyaniline as a control study to benchmark future oMLD chemistries final properties and electrochemical activity. Electrodeposition of pAni films was conducted using previously established conditions from literature for constant current, constant voltage, and cyclic voltammetry, deposition techniques in aqueous electrolyte. These previously reported techniques failed to produce the level of control needed for uniform, nanoscale, films. Our work outlined in chapter 2, explains a new high voltage pulse deposition technique for uniform and nanoscale control of pAni films. This uniform coating process allowed for a controlled study of polymer properties as a function of the films thickness, where higher specific capacities can be reached with thinner polymer films. This electrochemical deposition of pAni imparted many insights into the head-to-tail polymerization mechanism needed for polymer film growth and their expected electrochemical response (CV). This work outlined the importance of thin-film polymers with redox functionalities provide higher specific capacities than thicker polymer films, requiring less overall energy while utilizing reversible redox process.

After successfully obtaining benchmark studies for electrodeposited pAni films, a gas phase

ALD/MLD/oMLD reactor, as seen in Figure 1.10, was constructed for oMLD studies of oxidative polymerization in gas phase chemistries. Details of reactor can be found in Chapter 3. oMLD of pAni thin films was conducted using a modified procedure from previously reported oMLD work by Parsons et. al. The resulting polymer film was non-conformal and possessed low redox response compared to electrodeposited pAni and is outlined in chapter 3. For comparison, oMLD of EDOT, and polypyrrole (pPyl) were conducted using the same reaction conditions, i.e., pAni oMLD conditions, and produced redox active polymer films with molecular layer control over film thickness. Depositing pPyl via oMLD, with self-limiting surface reactions, produces uniform, smooth, conformal polymer films, like that of similar chemistries (i.e., ALD. MLD). Electrochemical capacities of pPyl utilizing oMLD versus electrodeposition provides a viable film deposition technique for three dimensional substrates with high capacities and charge rates. The work in chapter 3 carries on discussing the prevention of head-to-tail polymerization reaction of pAni with the addition of amino functional groups to anilines para-position. Blocking head-to-tail polymerization pathway resulted in uniform, redox active polymer films inline with EDOT and pPyl oMLD depositions. Molecular scale substitutions of functional groups on monomers for oMLD chemistries, have bulk property implications of final properties.

With synthesized polymers utilizing oMLD chemistry being limited to just a few, little information is available for monomers/polymers capable of redox active film growth using MoCl5. With successful oMLD depositions of EDOT, pPDA, and pPyl, other five membered, hetero atom containing, aromatic rings with similar polymerization pathways, i.e., Furan and Thiophene. oMLD of poly(Furan) and poly(Thiophene) resulted in no observable growth of polymer films nor their respective redox activities. With in-situ quartz crystal microbalance (QCM) studies and ex-situ film characterizations, the relationship between the oxidant and monomer during oMLD polymerization was examined for their role in polymer propagation in gas phase growth. oMLD gas phase mechanisms in early studies have depicted polymer growth as homogenous polymerization, where in fact these reactions are limited to heterogeneous surface reactions. In chapter 4 we establish key insights into the oMLD growth mechanism to help explain inhibited growth of polymer films (i.e., poly(furan) and poly(thiophene)) with MoCl5, as the oxidant.

In Chapter 5, thin film pEDOT electrochemical properties, formed by oMLD, were examined as a function of the polymer films thickness. Although the electronic properties of pEDOT formed by oCVD and oMLD have been studied extensively, only a few studies have examined the electrochemical charge storage properties of these pEDOT films. The impact of polymer film thickness on charge storage properties were examined as structural moieties begin to shift during polymer growth of

pEDOT films.

Chapters 2 through 5 are detailed, published articles detailing the work outlined above.

Chapter 2

PULSED ELECTRODEPOSITION OF ULTRATHIN POLYANILINE FILMS AND MECHANISTIC UNDERSTANDING OF THEIR ANION-MEDIATED ELECTROCHEMICAL BEHAVIOR

2.1 Abstract

Electrode materials which undergo anion insertion are of interest for next-generation energy storage devices and electrochemical water desalination. Polyaniline (PANI) is a robust and well-studied electrode material for anion insertion, but to date we have been unable to establish the electrochemical and anion-binding performance of PANI at nanoscale thicknesses because these thicknesses are not obtainable using standard PANI deposition procedures. Here, we report a new pulsed electrodeposition procedure for the controlled growth of PANI thin films with nanometer-scale thickness control. Using this pulsing technique, we deposit nanoscale ($<$ 100 nm) thin films of PANI onto stainless steel (SS) disks and gold electrochemical quartz crystal microbalance (EQCM) crystals. We examine the charge rate and anion-binding properties as a function of nanoscale thickness, and reveal previously undescribed insights into the charge storage and anion binding mechanisms of PANI. In particular, we identify that $<$ 10 nm PANI films provide rapid chloride ion uptake for desalination applications, and that thicker 100 nm PANI films are able to achieve rapid charge storage in sulfate solutions due to SO42-/HSO4- embedded within the PANI acting as a proton donor/acceptor. The results we report will inform the use of PANI thin films for energy storage and desalination applications.

2.2 Introduction

In recent years, interest in electrode materials which bind negatively charged anions has been growing. This interest is motivated by the emergence of anion and dual-ion batteries,[54, 55, 56, 57] enhanced electrochemical desalination based on capacitive deionization with redox-active electrodes[58, 59, 60, 61, 62], and by the need for sensors to detect and capture a range of emerging anionic contaminants in water streams[63, 64, 65, 66]. In each of these application spaces, we need high-performance anion-binding electrode materials. One of the most robust and well-studied materials which binds negatively-charged anions under electrochemical bias is polyaniline (PANI). PANI is a redox-active, electrically-conducting polymer which was discovered more than 150 years ago [67]. PANI exhibits both high specific capacitance ($>$ 500 F/g and up to 2000 F/g),[68, 69, 70, 71] and high electrical conductivity (>580 S/cm)[72], making it an attractive candidate for anion insertion electrochemistry.PANI's high-rate redox activity has motivated the extensive study of PANI as an electrode material for electrochemical supercapacitors[68, 69, 70, 71, 73], and the anion-mediated charge behavior of PANI has been shown to enhance anion removal in desalination electrodes[74]. However, in each of these application spaces, the effect of the PANI film thickness on performance has not been well-characterized. To improve the charge rate of PANI for energy storage and desalination, it is desirable to deposit a thin film of PANI onto a high-surface-area electrically-conductive electrode support. This minimizes the length scale for slow solid-state ion diffusion while maintaining electrical conductivity to the active material through the electrically-conductive support. Although the advantages of thin polymer films have been recognized in previous literature[71, 75], and the effect of PANI thickness on electrochemical performance has been examined in select studies[75, 76], the PANI thicknesses examined in these studies have been consistently greater than 100 nm. Little work has been done to characterize and understand how the PANI film thickness impacts the anion-binding capacity and rate for nanoscale thicknesses ($i.e./ < 100nm$). One might expect that reducing the PANI film thickness below 100 nm should enhance charge rate of PANI, in line with observations for pseudocapacitive manganese oxide thin-film electrodes which identify a maximum rate capability at a film thickness of 10-50 nm.[61, 77] In the present work, we examine the electrochemical properties of ultrathin PANI films to understand how the thickness of PANI impacts the ion uptake capacity and rate in varying anion solutions. To examine the electrochemical properties of ultrathin (¡ 100 nm) PANI films, we must first be able to control the PANI film thickness in this range. The two most common methods for PANI synthesis are chemical oxidation, and electrochemical formation.[78, 79]

Unfortunately, these synthesis routes provide only minimal control of the thickness and uniformity of PANI.[80, 81, 82, 83, 84, 85, 86] Electrodeposition has been reported to form nonuniform 3D architectures during electrochemical deposition.[87, 88, 89, 90] Similar effects have been observed for chemical oxidation.[82, 83, 84, 85, 86] Although recent work has improved upon standard homogeneous chemical oxidation to provide improved thickness control of PANI, this approach still only provides about 1 m thickness resolution, and results in porous and fibrous films.[91, 92] Without a means to precisely control the film thickness of electrodeposited PANI, prior reports have been unable to investigate how the nanoscale thickness of the PANI film impacts the electrochemical mechanisms it undergoes.Here, we deposit PANI nanoscale thin films using a pulsed electrochemical technique which provides improved film uniformity and control of PANI film thickness over prior electrodeposition studies. Our approach is comparable to recent work demonstrating precise thickness control of lithium metal by electrodeposition.[93] We examine the chemical effects leading to improved uniformity using the pulsed deposition technique. We then take advantage of the improved thickness control achieved using the pulse deposition technique to characterize the electrochemical performance of nanoscale PANI thin-films. The thin dense PANI layers we form enable the use of EQCM to provide insight into how the PANI thickness impacts the electrochemical mechanisms occurring in electrodeposited PANI thin films. We evaluate the anion binding mechanisms and rates, and examine the impact of anion identity on the observed electrochemical behavior. We also examine how the electrochemical mechanisms change as the PANI thickness changes. The understanding of the specific chemical mechanisms during electrochemical cycling of PANI will help inform improved performance of PANI as an electrode material in energy storage and desalination electrodes.

2.3 Materials And Methods

2.3.1 PANI Electrodeposition

PANI thin-films were electrodeposited onto a 1.2 cm2 area of 5/8" diameter 316L stainless steel (SS) discs (Pred Materials) using a Biologic SP-150 potentiostat. A fresh 1.0 L bulk aniline solution consisting of 0.1 M aniline and 1.0 M H2SO4 was prepared at the start of each set of experiments, degassed vigorously with argon for 20 minutes, then set to slowly bubble for the remainder of the experiments. Each deposition used 10 mL of degassed aniline solution in a custom glass electrochemical cell for flats evaluation with a graphite rod counter electrode, Ag/AgCl reference electrode, and SS working electrode. All experiments were conducted at ambient conditions. The electrochemical

deposition of PANI was carried out using an initial nucleation pulse of 1.3-1.7 V for 1-3 seconds followed by a pulse-rest cycle series of 0.0 V and 0.8 V vs. Ag/AgCl for 1.5 seconds each, repeated varying numbers of times. The initial pulse at 1.3 V vs. Ag/AgCl was used in an effort to rapidly oxidize aniline molecules close to the surface and enable nucleation of PANI. The subsequent pulsing at 0.8 V vs. Ag/AgCl deposited further PANI on this nucleation layer, while the hold at 0.0 V vs. Ag/AgCl was intended to replenish the depleted layer of aniline near the surface so that oxidizing pulses provided a uniform coating of PANI. SS substrates were coated with PANI using between 5 and 30 pulse-rest loop cycles.

2.3.2 Spectroscopic Ellipsometry

After electrodeposition, samples were rinsed with DI water and methanol and blown dry using filtered air. The thicknesses of the electrodeposited PANI films were analyzed using spectroscopic ellipsometry (SE) as measured using a J.A. Wollam Alpha-SE ellipsometer at wavelengths from 380 nm to 900 nm, and analyzed using the CompleteEASE software package. The samples were measured at incident angle of 65○ with a 10 s acquisition time. Films were modeled using a previously reported model for PANI films between 10-150 nm comprised of four Lorentz oscillators to arrive at modeled thicknesses.[94]

2.3.3 Atomic Force Microscopy

Atomic force microscopy (AFM) was conducted using a Bruker Innova atomic force microscope. PANI films deposited on SS discs were scanned over a 5µm x 5µm area at a rate of 1.00 MHz. The data was then transferred and processed by Gwyddion software to calculate RMS roughness and 3D film topography.

2.3.4 SEM Film Analysis

SEM thickness evaluation was performed with FEI Scios DualBeam FIB SEM, where a 500 nm X 100 nm layer of platinum (Pt) was deposited on top of the PANI film, then the surface was ion beam etched away to form a trench to expose the PANI layer. High contrast SEM images of the PANI film between the Pt layer and SS substrate were collected and the thickness of the PANI layer was measured over multiple points along the profile using ImageJ. Reported SEM thicknesses are average values where error bars represent the variation in thickness observed from these measurements.

2.3.5 Electrochemical Quartz Crystal Microbalance

Electrochemical quartz crystal microbalance (EQCM) measurements were performed with a Stanford Research Systems QCM200 interfaced with a Biologic SP-150 potentiostat. Gold-plated 5 MHz EQCM crystal were held within the QCM200 sample holder and submerged in 100 mL of degassed aniline solution and treated using pulse/rest cycles at 0.8V/0.0 V vs. Ag/AgCl to deposit PANI films. The EQCM crystal was then removed from solution and rinsed with DI water and methanol. The rinsed EQCM crystal was then submerged into a degassed 0.1 M NaCl solution at a pH 3.5, and EQCM/CV analysis was performed at a sweep rate of 50mV/s over a potential window of 0.0-1.0 V vs. Ag/AgCl. During the EQCM analysis, the change in frequency was recorded for both PANI deposition and ion binding and converted to mass assuming Sauerbrey behavior.[95] These data were used to evaluate the change in mass with respect to the change in potential to understand PANI growth and ion uptake.

2.3.6 X-ray Photoelectron Spectroscopy

PANI films were evaluated with X-ray photoelectron spectroscopy (XPS, Kratos Axis 165) to investigate the composition and redox state of the films during the deposition process. A monochromatic Al K X-ray source was employed with charge neutralization. High-resolution scans of C 1s and N 1s regions were performed with a 200 s acquisition time, 500 ms dwell time, 40 eV pass energy, and 100 meV step size. The peak locations were charge-corrected with the C 1s peak centered at an energy of 284.6 eV. The final XPS spectra were analyzed using the XPSpeak4.1 and Origin software to establish the chemical state of N during various stages of the pulsed electrochemical deposition.

2.4 Results And Discussion

PANI Electrochemical Nucleation Layer In the first part of this work, we report on a pulsed nucleation/growth electrodeposition technique which enables improved uniformity and thickness control of electrochemically-deposited PANI thin films on SS substrates. Prior electrodeposition studies have used constant current, constant potential or sweeping CV methods to deposit PANI on SS.[96] However, these techniques produce rough films with poor uniformity and lack of thickness control, as described in the introduction. Here, we improve on these prior techniques by (1) employing a nucleation step where we pulse at higher voltages (1.3-1.7 Volts vs. Ag/AgCl) for short periods of time (1-3 seconds) to assist in nucleation on SS substrates and then (2) using a series of pulse-rest

cycles consisting of 0.8 V and 0.0 V vs Ag/AgCl for 1.5 seconds each to grow the PANI film to a desired thickness as described in the Materials and Methods section. We note that the multi-step pulsed voltage procedure we employ is distinct from previously-reported pulsed current deposition of PANI, which resulted in fibrous and porous PANI films.[97] The two-stage pulsed voltage deposition procedure we employ was found to provide uniform deposition with nanometer-scale control of the PANI film thickness as described further below. In Figure 1, we compare the deposition of PANI films on SS substrates using constant-voltage deposition techniques from the literature and the pulsed deposition technique we report here. Figure 1a depicts the thickness of PANI films as measured by SE at 20 points across the line-scans for each sample depicted in the insets of Figure 1a. The PANI film deposited using a constant voltage in Figure 1a is non-uniform with variations in thickness from 30 nm and 50 nm across the line-scan of the deposition area, and some areas with no deposition. The variation in thickness over the sample area for the sample deposited with constant voltage can also be visually observed in the photograph of the SS disc labeled "Constant V" in the inset of Figure 1a. The PANI film deposited using the pulsing technique we report has visually-improved uniformity vs. the constant voltage growth procedure as shown in the photograph labeled "Pulsed" in the inset of Figure 1a. For 17 of the 20 locations measured along the line scan of the PANI film deposited using the pulsed technique, the thickness was measured to be between 42 nm to 45 nm. The three points which fall outside this thickness range are in the region of the sample surface near the edge which was covered by an o-ring seal in the electrochemical cell and was not exposed to the electrolyte solution during the deposition procedure.

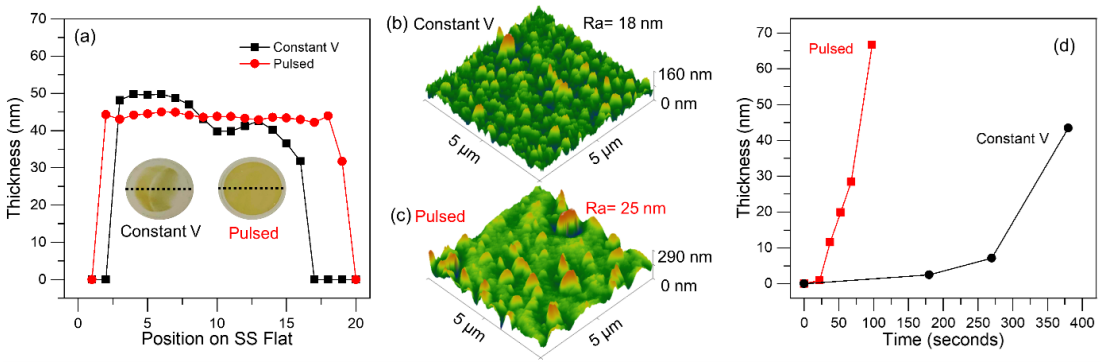

Figure 2.1: Comparison of electrodeposited PANI films using constant voltage or pulsed technique showing differences in (a) surface uniformity, (b) and (c) surface roughness, and (d) deposition time.

The surface roughness of the electrodeposited films was characterized by AFM for PANI films deposited using constant voltage (Figure 1b), and the pulse technique (Figure 1c). From these

AFM measurements, the root mean squared surface roughness (Ra) was determined to be 18 nm for the sample deposited using constant voltage, and 25 nm for the PANI deposited using the pulsed technique. We attribute the larger roughness of the sample deposited using the pulsed technique to isolated formation of large particles across the film as discussed in further detail below. In the regions between these isolated particles, we observe a much lower roughness of 6.7 nm for the pulsed PANI film. We also attempted depositing PANI on SS using only pulsing cycles without the nucleation step of 1-3 seconds at >1.3 V (not shown), and observed non-uniform PANI deposition closely resembling to the profile of PANI film deposited using constant voltage. This procedure also resulted in thicknesses ranging between 30 and 50 nm over the deposition area in line with the constant voltage procedure depicted in Figure 1. The nucleation pulse pretreatment provides more uniform deposition of the polymer over the sample surface. In addition to the uniform deposition characteristics we observe by pretreating SS with a nucleation pulse at >1.3 V vs. Ag/AgCl, the time for deposition is significantly shortened, providing more rapid film preparation. In Figure 1c, we compare the deposition time required to reach specific thicknesses using our pulse deposition technique we report here compared to a constant voltage deposition technique commonly employed in the literature 43. When applying constant voltage, six minutes was needed to deposit a film thickness > 20 nm, whereas the pulse technique we report required 90 seconds. We also note that the PANI films we deposited using conventional deposition techniques were delicate and frequently delaminated from the SS during handling. The pulsed deposition procedure we report seemed to remedy this issue and the resulting PANI films were stable during handling even with friction applied to the surface. The differences in mechanical stability of these films is surprising and we plan to explore this further in future work. PANI Deposition Mechanism To understand the mechanism for improved growth uniformity using a pulsed electrochemical technique, we employed XPS, SE, and electrochemical impedance spectroscopy (EIS) measurements. Using XPS we are able to examine the nitrogen (N) species found in the PANI film during each phase of deposition and provide insight into the evolution of the chemical environment in the PANI film during the high-voltage pulse and subsequent growth. SE and EIS provided complementary information about the polymer film growth and electrochemical properties of the PANI films from nucleation to final steady state growth. We first examined the characteristics of the surface following the high-voltage nucleation pulse at 1.3-1.7 V vs. Ag/AgCl without subsequent growth pulses. During the high voltage pulse, we expect to generate an excess of active oxidized aniline species which will react on the SS substrate to form short chain oligomers.[82, 98] We note that we observed a yellow cloud form near the surface of the SS surface (extending about 1 mm into the electrolyte) during the high voltage nucleation

pulse, confirming the rapid generation of active monomers. This cloud was easily removed by either agitating the aniline solution or during rinsing after substrate removal from electrochemical cell, and the material from the yellow cloud was not incorporated into the final PANI films. From ex situ SE on the SS substrate following the nucleation pulse, we determined that this initial pulse resulted in the rapid deposition of a uniform 5 nm thick film across the SS surface. To examine the properties and composition of this layer formed during the nucleation pulse, we performed EIS and XPS. EIS analysis following the nucleation pulse revealed a decrease in interfacial charge transfer resistance by many orders of magnitude compared with the bare SS substrate. The interfacial resistance of the bare SS substrate was measured to be 115 k, whereas a value of 3.9 k was measured following deposition of the nucleation layer. The dramatic decrease in interfacial charge transfer resistance may indicate that the nucleation layer enables facile charge transfer to the aniline solution during subsequent pulse cycles, allowing early stage functionalization and subsequent growth. We performed XPS analysis to identify the origins of this decreased charge transfer resistance. These XPS measurements in Figure 2a,d revealed that the film formed during the high-voltage nucleation pulse contained an excess of oxidized quinoid-imine (R-N=R) species, which represented more than 50% of the N content in the initial film. The remaining N content consisted of 30% unoxidized secondary amine (R-NH-R) and 17% charge-carrying amine radical cation (R-N•+H-R) species. The oxidized R-N=R species are expected to provide extended pi conjugation and form a connective network for charge transport through the polymer film for subsequent polymer growth. We expect that this electrical conductivity helps contribute to the facile nucleation of PANI following the nucleation pulse. Likewise, the blend of R-NH-R and R-N•+H-R species both provide anchors for subsequent polymer growth, and the R-N•+H-R species also provide charge carriers for electrical conductivity. We note that the high voltage pulse may also impact the SS surface chemistry, either by removing carbonaceous species from the surface or by modifying the functional groups on the SS surface. Evidence of these mechanisms was not observed ex situ by XPS, but these effects may occur transiently during the high voltage nucleation step.

To confirm our interpretation that the high voltage nucleation pulse generated an electrically-conductive layer which enabled polymer growth, we examined how the properties of the polymer film evolved during subsequent growth. Interestingly, during the first five pulse-rest cycles following the nucleation pulse, the film thickness was found to decrease from 5 nm to 1 nm as depicted in Figure 2e. (Note that each pulse-rest cycle consists of holding the potential at 0.8 V vs. Ag/AgCl for 1.5 s and then at 0 V vs. Ag/AgCl for 1.5 s as described above). The loss in thickness is accompanied

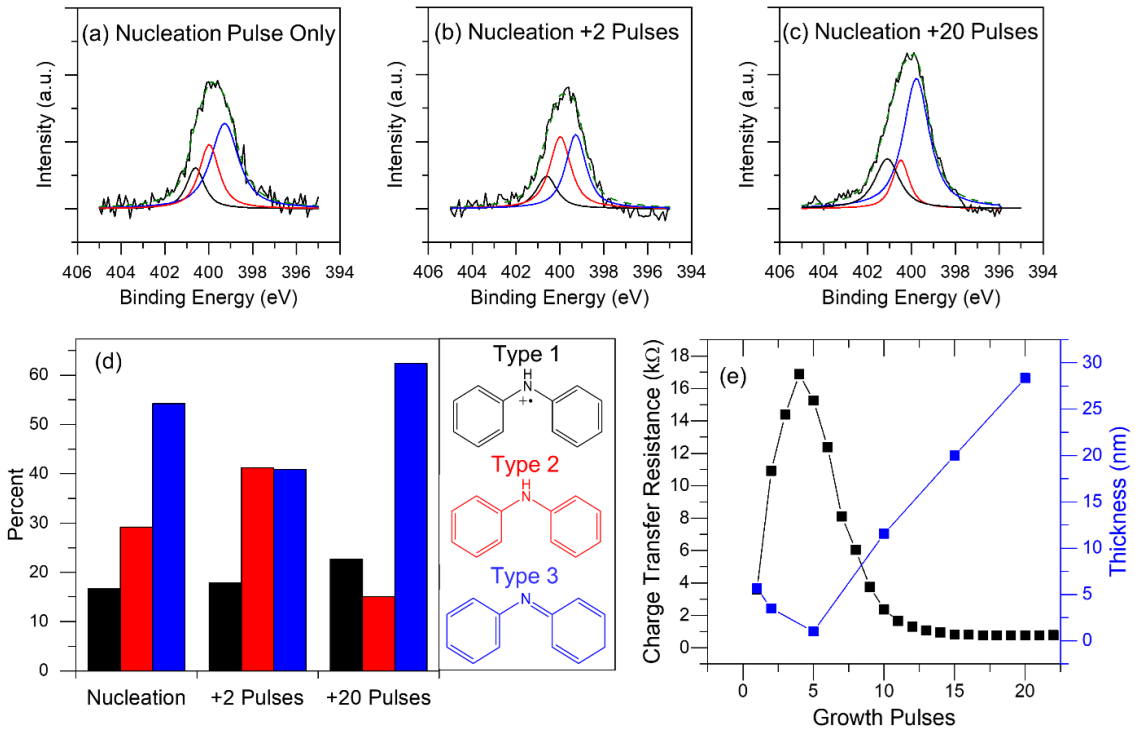

Figure 2.2: CXPS measurement of the N 1s region on electrodeposited thin films (a) following high-voltage nucleation pulse, (b) following nucleation pulse and 2 growth pulses, and (c) following nucleation pulse and 20 growth pulses, yielding (d) speciation of nitrogen from fitted XPS curves at each growth stage. These XPS data are connected with changes in (e) thickness (blue) and charge transfer resistance (black) during first 25 pulses of deposition.

by an increase in charge transfer resistance for every pulse cycle up to the fifth pulse-rest cycle. To understand the origins of the decrease in thickness and concomitant impedance increase, we examined the composition of the PANI film by XPS following two growth pulses after the nucleation step in Figure 2b,d. We observe that the fraction of R-N=R species diminishes and the fraction of R-NH-R species increases relative to the film formed during the nucleation pulse. We attribute the increased fraction of R-NH-R to the reduction of R-N•+H-R groups during the 0.0 V vs. Ag/AgCl pulse. While the complexation of additional aniline monomers to the electrode surface during the 0.8 V vs. Ag/AgCl pulse could also contribute to this effect, we do not expect this to be the case considering the overall decrease in film thickness during this phase of growth. Although the increase in interfacial charge transfer resistance during the first five growth pulses is consistent with the loss of electrically-conductive R-N=R groups and increase in electrically-resistive R-NH-R as we observe by XPS, the origins of the loss of PANI thickness during the first five growth pulses following nucleation is unclear. We suspect that short-chain oligomers form on the surface during the nucleation pulse and some fraction of these desorb during the first five growth pulses after nucleation. Following the

first five growth pulse after nucleation, the PANI film thickness was found to increase in a roughly linear trend with the number of growth pulses up to a final thickness of 28.4 nm at 20 growth pulses, corresponding to a growth rate of 2 nm/pulse between 5 and 20 growth pulses. The charge transfer resistance of the deposited film (as measured by EIS measurements and reported in Figure 2e) approaches a constant value of 2 k with increasing thickness during the growth from 5 to 20 growth pulses. The final 30 nm film is comprised primarily of R-N=R (60%), with the lowest composition of R-NH-R (15%) and the highest composition of R-N•+H-R (25%) as compared with the films formed during the first five growth cycles. We expect this increase in charge-carrying R-N•+H-R and conjugated R-N=R species produces a lower resistance in the bulk PANI film. Thickness Control of PANI To evaluate thickness control using the pulsed nucleation/growth technique described here, we performed a series of both ex situ thickness measurements on SS samples using SE and in situ mass measurements using EQCM during electrodeposition. The mass gain (EQCM) and thickness (SE) of the PANI films are plotted against the number of 1.5 second oxidation pulses at 0.8 V vs. Ag/AgCl in Figure 3c. We note that the gold EQCM crystal did not require the initial nucleation pulse at > 1.3 V vs. Ag/AgCl for nucleation. This may arise from differences in the contact resistance at the electrode/electrolyte interface between SS and Au. SS is known to have a Cr2O3 surface layer which may influence charge transfer at this interface.[99, 94] Although the Au EQCM crystal did not require a nucleation pulse to initiate growth, we did observe a nucleation delay during the first 10 pulses on the Au EQCM crystal as depicted in Figure 3c in line with the delayed growth observed on SS following the nucleation pulse. After this nucleation delay, the mass gain increased in a roughly linear trend with pulse number in line with observations on SS substrates following the nucleation pulse and five growth pulses at 0.8 V vs. Ag/AgCl. After this nucleation delay, the mass and thickness of the PANI films both increased linearly with pulse number. We also verified the thickness of the PANI films by SEM (as described in the Materials and Methods section) for samples deposited using 20 and 30 oxidation pulses. By dividing the EQCM mass gain after 30 growth pulses (5.2 ng/cm2) by the SE thickness on the SS substrate after 30 growth pulses (67 nm), we arrived at a predicted density of the PANI film of 0.776 g/cm3. This value is the same order of magnitude, but is 38% lower than the value of 1.245 g/cm3 expected for PANI base.[95] This discrepancy may arise because the values of thickness and mass are taken from different substrates (SS and Au EQCM crystals, respectively). These different substrates may yield different nucleation/growth behavior. Additionally, the roughness and nonuniform thickness of the PANI films on the SS substrates as observed by AFM may impact the measured SE thickness. We also note that the viscoelastic properties of the PANI film may impact the mass gain measurement from EQCM.[100, 101] The overall growth patterns of

EQCM and SS depositions correlate well with each other, and both indicate roughly linear growth of PANI films following a nucleation period, providing nanometer resolution in thickness control using the pulsing procedure reported here.

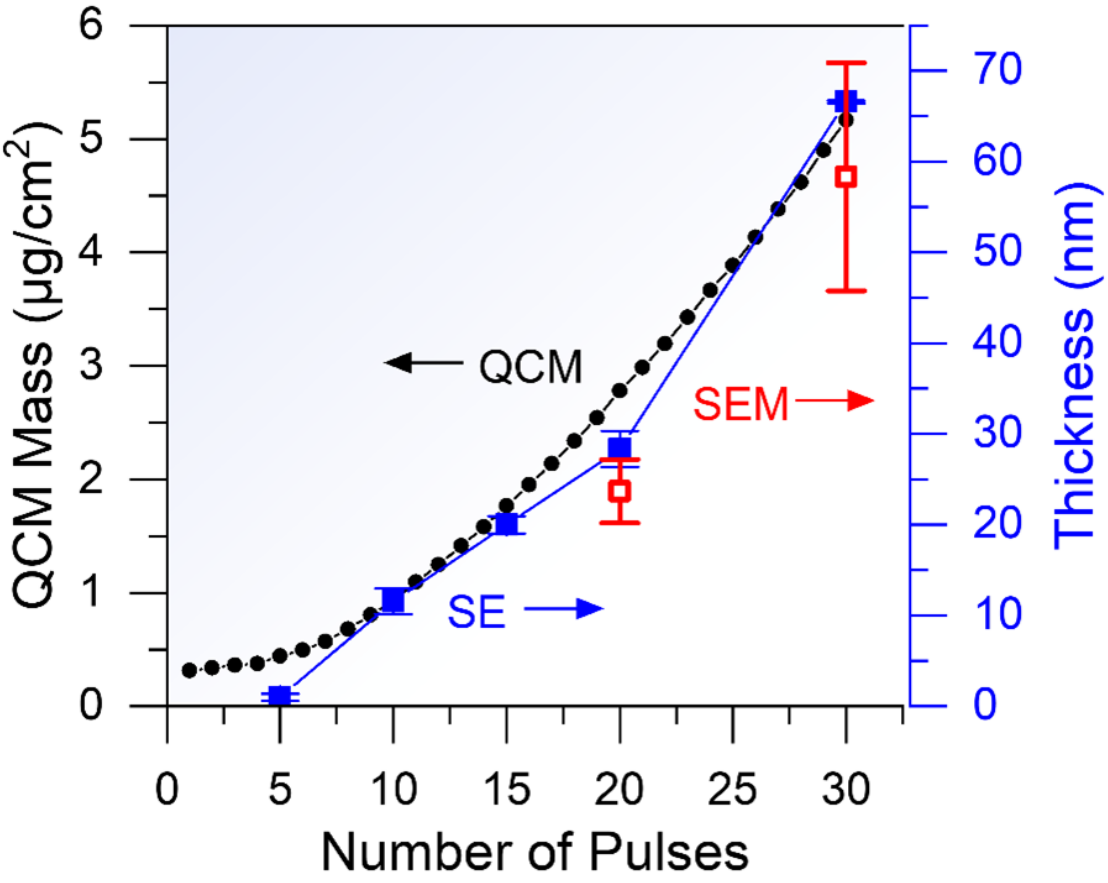

Figure 2.3: Plot of EQCM mass (filled black circles) and SE thickness (filled blue squares) versus number of deposition pulses. SE thickness measurements were benchmarked against thicknesses from SEM cross-sections after 20 and 30 pulses (open red squares).

Impact of PANI Thickness on Charge Rate Upon establishing the ability to control the thickness of PANI films with nanometer resolution using the pulsed deposition technique we report here, we then set out to examine how the PANI thickness impacts the electrochemical properties of the PANI films. The electrochemical redox activity of the PANI films of various thicknesses was first evaluated using CV measurements as depicted in Figure 4. For each of these measurements, the sample was removed from the growth solution, and CV was performed in 1 M H2SO4 before returning the sample to the growth solution for continued growth. We observed CV peaks with equilibrium potentials at 0.2, 0.5, and 0.7 V vs. Ag/AgCl in this 1 M H2SO4 solution (pH of 1.5) for all of the PANI thicknesses

examined, where the peak heights increase with increasing PANI thickness. These peak locations agree closely with previously reported literature [102, 103, 104, 105, 106] and indicate formation of redox-active PANI films. We also observed characteristic electrochromic changes in the PANI films when cycled between 0.0-0.9 V vs Ag/AgCl, as depicted in previous reports.[107, 108, 109] Following initial studies in 1.0M H2SO4, PANI films were further analyzed in 0.1 M NaCl and HCl solution (pH of 3.5) and reported below. A NaCl(aq) solution was employed here to study the ion binding characteristics of PANI to Na+ and Cl^- for their relevance to desalination applications, and a pH of 3.5 was employed instead of a higher pH to enhance the redox properties of PANI films.[110] Prior work has established that changing the pH and ionic strength and charge significantly impacts the electrochemical properties of PANI.[111, 112, 113, 114] Consistent with prior studies,[110] we observed that at pH's higher than 3.5 (not shown), the redox peaks near 0.2 and 0.7 V are not present, and the peak at 0.5 V increases compared with the peak height observed in 1.0 M H2SO4. This shift in electrochemical behavior has been attributed to a change in redox mechanism related to the interaction of PANI redox sites with Na+ and Cl^- ions.[111, 112, 113, 114,] Because PANI redox properties are proton-mediated, the change in electrochemical properties in higher pH electrolytes is expected.[115, 116, 117, 118, 119] While the pH is known to influence the redox properties of PANI, our main focus here is to understand how the PANI thickness influences the electrochemical properties.

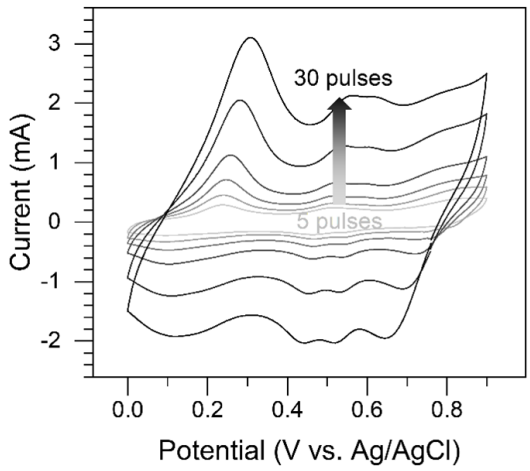

Figure 2.4: CV measurements on PANI films in 1 M H2SO4 following varying numbers of deposition pulses, with traces shown after every 5 deposition pulses.

To understand the impact of PANI film thickness on its electrochemical properties, we evaluated the charge storage capacity on SS discs with varying thickness of PANI using CV of sweep rates ranging from 10 mV/s to 500 mV/s. In Figure 5a, we report the total charge versus thickness for each of the measured sweep rates from 10-500 mVs-1. The highest charge capacity for each film was observed at the slowest sweep rate (10 mV/s). This low sweep rate allows sufficient time for kinetically slow processes to proceed and results in a higher measured capacity. Taking a linear fit of the data collected at a sweep rate of 10 mV/s (red dashed line in Figure 5a) yields a slope of 0.07 mC/nm. Accounting for the exposed electrode surface area of 1.2 cm2, and

taking the PANI density to be 1.245 g/cm3 (as described above), this corresponds to a charge capacity of 130 mAh/g, and a specific capacitance of 520 F/g over the 0.9 V potential window. This value is in line with previous reports on the specific capacitance of PANI in excess of 500 F/g.15–17 For the 4 nm PANI thickness, we measure a charge capacity of 1.09 mC, which corresponds to a specific capacity of 500 mAh/g and a specific capacitance of 2000 F/g using the same conversions as reported above. We note that these values may be inflated by a larger contribution of double-layer capacity at this lower film thickness, but are in line with values of up to 2000 F/g measured for nanoscale PANI composites in prior work.18 We also note that a 10 mV/s sweep rate corresponds to a 90s charge time, or a charge rate of 40 C. The high capacity and rate capability we report for thin PANI films highlight the potential of PANI in enabling high rate energy storage, and rapid desalination.

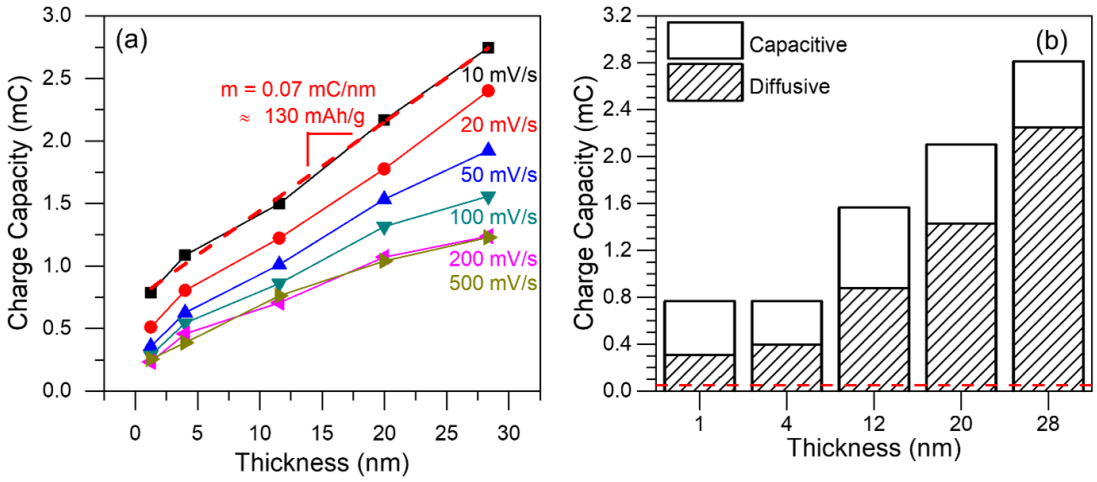

Figure 2.5: Evaluation of rate capability of nanoscale PANI thin films of 1-30 nm established by performing (a) CV at sweep rates of 10-500 mV/s in 0.1 M NaCl solution at pH 3.5 and analyzing this data to (b) separate capacitive and diffusive charge properties of the PANI films. The horizontal red dashed line in (b) represents the charge capacity for a bare SS disc.

To understand the high capacity and rate capability reported above, we further evaluated the fraction of capacitive and diffusive charge storage behavior at each PANI thickness using a log-log analysis method developed previously.[120] In Figure 5b, we report the capacitive and diffusive contributions to charge storage at each PANI thickness using this analysis technique. For the 4 nm film thickness we observe 50% capacitive charge storage, whereas for the 28 nm film thickness we observe only 20% capacitive charge storage, with the remaining 80% of charge storage restricted by diffusion limitations. We observe a relatively constant contribution of capacitive charge storage (0.5 mC) across all thicknesses in Figure 5b suggests that the outermost PANI surface undergoes rapid

redox while the bulk material is limited by slow ion diffusion through the PANI film. (The diffusivity of anions in PANI is on the order of 10-15 cm2/s at room temperature.[121, 122, 123]) Multiplying the fraction of capacitive charge storage by the PANI film thickness, we estimate that 5.8 ± 0.6 nm of PANI film thickness is responsible for the rapid capacitive processes. (This value is an average value calculated using the 12, 20, and 28 nm thick PANI films). Based on this result, we suggest that employing 6 nm PANI thickness will minimize diffusion-limitations and provide the highest rate of charge storage in PANI films. This is in line with the result reported above in the discussion of Figure 5a, suggesting that up to 2000 F/g were achievable for a PANI film thickness of 4 nm. Impact of PANI Thickness on Anion Binding Mechanisms To inform the use of PANI coatings as ion binding electrodes for desalination, we were interested to understand how the trends in charge capacity with PANI thickness translated to ion binding performance. Ion binding was analyzed for various thicknesses of PANI films using EQCM. PANI films were deposited onto gold EQCM crystals and analyzed in NaCl under the same conditions as described above (0.1 M NaCl adjusted to a pH of 3.5). The change in the EQCM resonant frequency was recorded during electrochemical measurements and converted into mass using the Sauerbrey equation to observe the charge and discharge of ions from the polymer film under electrochemical potential. In Figure 6a, we plot the change in mass versus the change in Q for four PANI thicknesses (9.7 24.6, 51.3, and 98.5 nm – nominally 10, 25, 50, and 100 nm). As the samples were cycled, the trace of mass change versus Q remained consistent over five consecutive CV cycles. In prior reports on PANI, the electrochemical mechanism has been reported to involve the uptake of anions (e.g. Cl^-) coupled with protonation of the nitrogen along the polymer chain.[103, 111, 112, 113, 114, 124, 125, 115] Our results are generally consistent with these prior reports, but the refined control of the PANI thickness provided by the pulsed deposition technique allows us to reveal additional insights into the charging behavior of PANI films as discussed below.

For all PANI thicknesses in Figure 6a, as the potential is swept from 0.0 V vs. Ag/AgCl (Q = 0) to more positive potentials (larger Q), electrons are withdrawn (oxidation) and mass increases. The increase in mass with oxidation (positive slope) up to 0.5 V indicates the uptake of anions into the PANI film over this region, as depicted in Figure 6b,c. For each PANI thickness, we observed a maximum value of mass at a potential of 0.5 V vs. Ag/AgCl. The specific charge state (moles of electrons) where this maximum mass was observed in Figure 6a varies with PANI thickness because thicker PANI films absorb more charge. We performed a linear fit of mass vs. charge for the 10 nm film over the potential region from 0-0.5 V vs. Ag/AgCl in Figure 6a, where the slope is largest, and

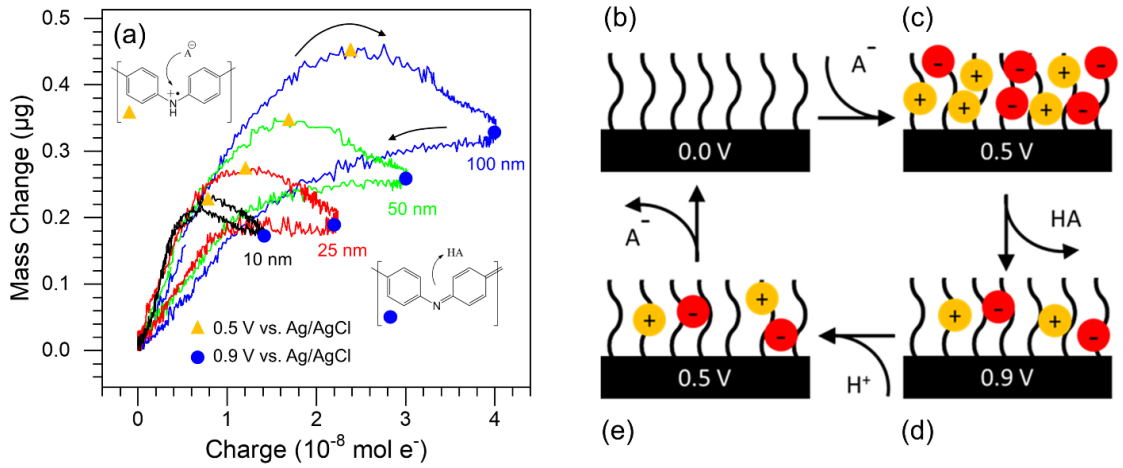

Figure 2.6: (a) EQCM measurements during CV of PANI films of 10-100 nm at 50 mV/s in 0.1 M NaCl solution at pH 3.5. EQCM data indicates mechanistic changes with PANI thickness. PANI film gains anions from solution as the potential is swept from 0.0 V to 0.5 V vs. Ag/AgCl(b-c). Under further oxidation from 0.5 V to 0.9 V vs. Ag/AgCl (c-d) PANI film releases anions back into bulk solution. Sweeping back to 0.5 V from 0.9 V vs. Ag/AgCl (d-e) the film begins to protonate and uptakes different amounts of ions depending on film thickness before releasing all bound ions as the potential is swept to 0.0 V vs. Ag/AgCl (b).

we measure the slope to be 38 g/mol e-. This value decreases with increasing film thickness, and was measured to be 29.7 g/mol e- for the 100 nm PANI film. The value expected for stoichiometric Cl^- uptake is 35.5 g/mol e-. In general, our data is consistent with electrochemical uptake of the Cl^- anion. The higher values of slope we observe for lower thickness may arise from deviation from ideal Sauerbrey behavior,49,50 and/or from a superstoichiometric amount of Cl^- ions binding to the surface of PANI at ultrathin film thicknesses, analogous to prior findings on thin-film sodium manganese oxide.8 Oxidation continues as the potential is swept from 0.5 V to 0.9 V vs. Ag/AgCl in Figure 6a, and the mass decreases for each sample until a potential of 0.9 V vs. Ag/AgCl. This behavior is consistent with the over-oxidation of PANI and the release of anions, as depicted in Figure 6c,d and reported in previous work.[126] Generally, the anion loss during over-oxidation is important to consider because it suggests that for ion binding applications (e.g. electrochemical desalination) the operational potential window for PANI should be restricted to $<$ 0.5 V vs. Ag/AgCl to prevent over-oxidation of PANI and limit unintended ion release. Interestingly, on the reverse (reducing) sweep (as the potential is swept from 0.9-0.0 V vs. Ag/AgCl in Figure 6a) we observe differences in the mass change behavior depending on the PANI thickness. For the thinnest films (especially for the 10 nm PANI thickness) we observe that the reverse trace in mass (during reduction) follows the forward trace in mass (during oxidation) with minimal hysteresis. The increase in mass in the 10 nm PANI film when sweeping the potential from 0.9 to 0.5 V vs. Ag/AgCl suggests that the

over-oxidation is reversible, i.e. that anions released during over-oxidation are able to re-bind to the PANI film before being released again as the potential is swept from 0.5 to 0.0 V vs. Ag/AgCl. In other words, the behavior of these thin polymer films is consistent with a path from Figure 6d, then to Figure 6c and back to Figure 6b. This is distinctly different from the behavior observed for the thickest (e.g. 50 and 100 nm) PANI films. For the 100 nm film in Figure 6a, the trace in mass on the forward sweep (oxidation) does not align with the trace in mass on the reverse sweep (reduction), but instead shows notable hysteresis. For these thicker PANI films, the mass loss from over-oxidation is not recovered, and the mass monotonically decreases as the potential is swept from 0.9 V to 0.0 V vs. Ag/AgCl. The trace of mass vs. charge for these thickest films is consistent with a progression from Figure 6d to Figure 6e and back to Figure 6b. These data suggest that the thinnest (10 nm) PANI films are able to recover from over-oxidation and may be more suitable for electrochemical devices aimed at extracting ions from solution. We attribute the hysteresis described above for the thickest PANI films to kinetic limitations arising from slow ion diffusion in the bulk PANI layers. We note that the diffusion of anions in the PANI film is slow—the diffusivity of the chloride anion [121] and other monovalent anions[122, 123] in PANI have been measured to be 10-15 cm^2/s at room temperature. We expect that Cl^- ions collect at the outer surface of the thickest PANI films during the over-oxidation step, and slow bulk diffusion limits the rate of binding of subsequent Cl^- into the subsurface of the PANI film. Finally, we examine the electrochemical mechanism of ultrathin PANI films in electrolytes containing sulfate ions. Prior studies have reported conflicting information on the charge rate of PANI in sulfate electrolyte. On one hand, it has been shown that replacing Cl^- with SO_4^{2-} in the electrolyte leads to a higher charge-storage capacity for PANI films, which seems to indicate faster SO_4^{2-} diffusion.[127] On the other hand, SO_4^{2-} has been found to diffuse slower than Cl^- in PANI under applied bias,[128] as well as in water.[129] The slower diffusion of SO_4^{2-} vs. Cl^- in PANI is also supported by the observation that larger ions diffuse slower in PANI.[130] The anionic radius of SO_4^{2-} is greater than that of Cl^- (0.23 vs 0.18 nm).80 In Figure 7 we perform EQCM measurements during CV on the same films as reported in Figure 6a and at the same sweep rate, but in sulfate electrolyte. For a 100 nm PANI film examined at the sweep rate of 50 mV/s in Figure 7a, we observe a charge capacity of 3.8 mC (86 mAh/g) with Cl^- in solution, and 10 mC (222 mAh/g) with SO_4^{2-} in solution, in line with prior reports that sulfate electrolyte enhances the capacity of PANI films. We also observe that in Figure 7a, the qualitative shape of the trace of mass change vs. charge for the 100 nm PANI film in sulfate electrolyte is more in line with the behavior observed for a 10 nm PANI film in chloride electrolyte in Figure 6a, where minimal hysteresis is observed. This seems to suggest that the sulfate ion does diffuse more rapidly within the PANI film, at odds with

prior reports that the diffusivity should be lower for SO_4^{2-}¬ than Cl^-. This interpretation is also in line with the data reported in Figure 7b, where the enhancement in capacity with the sulfate electrolyte is more pronounced for thicker PANI films. The capacities are roughly equivalent for the 10 nm PANI film in Figure 7b, whereas the capacity is > 2.5 times larger with the sulfate electrolyte for the 100 nm PANI film.

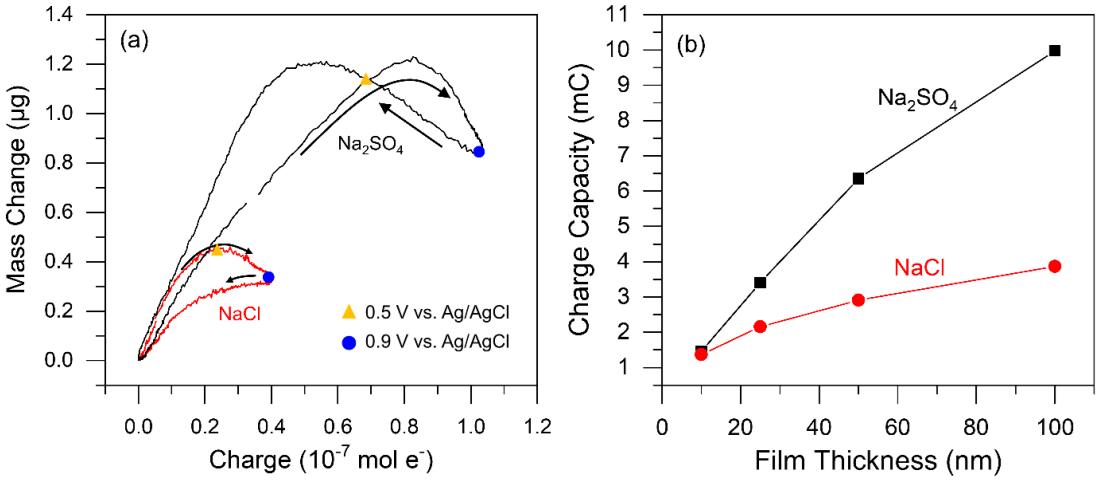

Figure 2.7: Plots of (a) mass versus charge measured using EQCM during electrochemical cycling of a 100 nm thick PANI film in 0.1 M NaCl vs. 0.05 Na2SO4 at a pH of 3.5 and a sweep rate of 50 mV/s and (b) comparison of total charge capacity of varying PANI film thicknesses in the same Na2SO4 and NaCl electrolytes as in (a).

Another potential contribution to the higher capacity observed for PANI in sulfate electrolyte versus chloride electrolyte could be the different charge states of sulfate vs. chloride. Each SO_4^{2-} anion is expected to be able to balance charge with two R-N•+H-R groups, whereas each Cl^- is expected to only able to balance charge with one R-N•+H-R group. Assuming that these ions occupy similar volumes within the PANI structure, one would expect to observe more charge storage in PANI with SO_4^{2-} anions incorporated into the structure vs. Cl^- anions, because more R-N•+H-R groups would be stable along the polymer backbone. However, the anionic radius of SO_4^{2-} is greater than that of Cl^- (0.23 vs 0.18 nm).[131] Assuming spherical anions, these radii correspond to a volume of 51 $Å^3$ for one SO_4^{2-} anion and a volume of 24 $Å^3$ for one Cl^- anion. Based on these volumes, two Cl^- anions would occupy approximately the same volume as one SO_4^{2-} anion within the PANI structure. We therefore conclude that the greater charge state of the sulfate anions would not necessarily produce a higher capacity or redox activity in the PANI films. Based on this analysis, rapid sulfate diffusion seems to be the only reasonable explanation, despite experimental

evidence indicating that sulfate should diffuse more slowly than chloride. However, upon closer examination of the data in Figure 7a, we identify another possible explanation. We note that the slope of mass change vs. charge on the oxidizing sweep from 0-0.5 V vs. Ag/AgCl in sulfate electrolyte in Figure 7a is inconsistent with the expectations for rapid stoichiometric insertion of sulfate anions. The maximum slope observed over this region in Figure 7a is 22.4 g/mol e- (versus 30 g/mol e- in the chloride electrolyte). If the sulfate anion were electrochemically and stoichiometrically inserting into the PANI film, one would expect the slope of mass change vs. charge in Figure 7a to correspond to the mass-to-charge ratio of the sulfate anion, as observed above in Figure 6a for chloride electrolyte. The SO_4^{2-} anion has a molecular weight of 96 g/mol, and at a charge state of negative two, one would expect a slope of 48 g/mol e- for the sulfate trace in Figure 7a. The slope we observe is 54% lower than expected. We extracted maximum slopes (occurring between 0 and 0.5 V vs. Ag/AgCl) on both the oxidizing and reducing sweeps from EQCM data (not shown) of each PANI film thickness in sulfate electrolyte and plot these values in Figure 8. From these data, we identify that the mass change on both the oxidizing and reducing sweep in sulfate electrolyte is $>$ 45% lower than expected on the oxidation sweep and $>$ 15% lower than expected on the reducing sweep for the 25, 50, and 100 nm films. For the 10 nm film, we observe a slope of 68 g/mol e- on the reducing sweep and 53 g/mol e- on the oxidizing sweep. These values are both larger than the value expected for SO_4^{2-} insertion, and indicate that some HSO_4^- may be involved in anion insertion in these thinner films. Based on the data presented in Figure 8, we propose a new explanation for the rapid charge rate of PANI in sulfate electrolyte. Specifically, we suggest that for thicker films of PANI, SO_4^{2-} anions within the PANI layer take on protons which are lost from the PANI during oxidation to form the monovalent hydrogen sulfate anion (HSO_4^-). These HSO_4^- anions can then remain within the PANI structure to both (a) balance the charge of cationic R-N•+H-R groups in the PANI structure

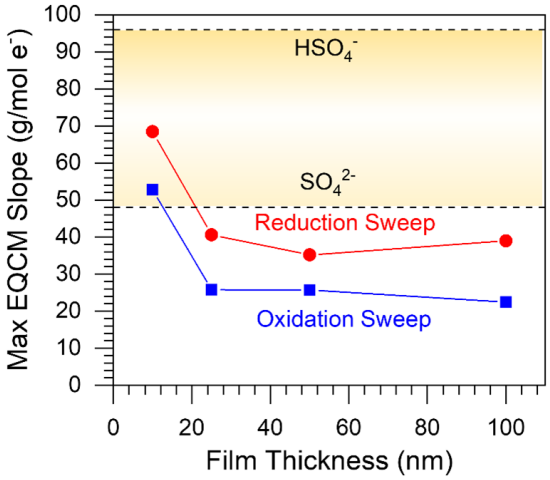

Figure 2.8: Maximum slope measured by EQCM over the potential window from 0-0.5 V vs. Ag/AgCl for varying PANI thicknesses on the oxidation sweep (blue) and reducing sweep (red). The range of expected values based on stoichiometric electrochemical anion insertion is highlighted in yellow with dashed lines for SO_4^{2-} and HSO_4^- bounding the lower, and upper bounds on the expected slope, respectively.

and (b) act as embedded proton donors during PANI redox electrochemistry. We propose that the lower-than-expected mass changes reported in Figure 8 arise because a fraction of sulfate anions remains within the PANI film. We therefore attribute the higher capacity in sulfate electrolyte vs. chloride electrolyte in Figure 7b to these sulfate anions embedded within the PANI layer which can act as proton donors/acceptors. We also expect that the SO_4^{2-}/HSO_4^- proton donor/acceptor couple enables improve the reversibility of the electrochemical processes even for thicker PANI films. This helps to explain why the hysteresis effect observed in chloride electrolyte in thick PANI films in Figure 6a is absent when using sulfate electrolyte in Figure 7a. We attribute the minimal hysteresis in the thick 100 nm PANI film to the presence of the SO_4^{2-}/HSO_4^- proton donor/acceptor couple, which allows for rapid reprotonation of the PANI polymer from HSO_4^- ions stored within the polymer structure. This embedded SO_4^{2-}/HSO_4^- proton donor/acceptor couple circumvents a mechanistic pathway which requires slow bulk ion diffusion and enables rapid reprotonation of the PANI backbone to provide high electrochemical capacity.

2.5 Conclusion

In this work, we report a new pulsed deposition technique for rapid and uniform growth of ultrathin (<100 nm thick) PANI layers with nanometer-scale thickness control, and employ this deposition technique to study the electrochemical behavior of ultrathin PANI films. On SS substrates, we identify the need for a nucleation pulse at > 1.3 V vs. Ag/AgCl to enable uniform film growth. This nucleation pulse produces an electrically conductive, quinoid-imine-rich layer on the SS surface that degrades upon the subsequent five growth pulses, but allows for facile PANI film growth thereafter. This pulsed deposition procedure provides improved uniformity and thickness control over existing electrochemical PANI deposition procedures, and may help enable the deposition of ultrathin PANI onto metal parts for a range of applications, including for corrosion protection[130, 132] and sensor applications.[132, 133] The improved thickness control afforded by the pulsed deposition technique we report allowed us to establish an understanding of the electrochemical properties of PANI films between 1 and 100 nm in thickness. We identify that the outer 6 nm of the PANI films (i.e. the near-surface layer) provides rapid charge storage with minimal diffusion limitations. Consistent with this observation, we measured a specific capacitance of 2000 F/g for a 4 nm thick PANI film at a sweep rate of 10 mV/s (a charge rate of 40 C), matching the highest measured values of specific capacitance for a composite PANI material.[71] The high specific capacitance of these nanoscale PANI films is in line with conventional expectations for a pseudocapacitive material [68, 134, 135]

and motivates the development of new procedures to achieve a uniform ultrathin (5 nm) PANI thickness onto a porous conductive electrodes. If procedures can be established to achieve this, it is expected to provide a maximal charge rate and be beneficial for high-rate energy storage and desalination applications. Finally, we examined the anion-insertion behavior of ultrathin PANI films using EQCM and identified previously undescribed phenomena that will inform the use of PANI layers for desalination and energy storage applications. In chloride solutions, we found that the thinnest (10 nm) PANI films are able to recover from over-oxidation and rapidly re-bind anions that are released upon over-oxidation. However, thicker PANI films did not exhibit this same recovery. We suspect that slow chloride diffusion in bulk PANI layers prevents recovery from over oxidation. In sulfate solutions, EQCM results suggested that some fraction of sulfate anions reside within the PANI layer during electrochemical cycling. We propose that these embedded sulfate anions react with protons through the SO42-/HSO4- couple and act as proton donors/acceptors to enable rapid charge/discharge of PANI. This helps to explain elevated capacitance values for PANI in sulfate solutions vs. chloride solutions.[127] These results motivate (1) the use of ultrathin 5-10 nm PANI layers for desalination applications to allow for rapid ion uptake and recovery from overoxidation and (2) the use of sulfate electrolytes and thicker PANI layers for energy storage applications, where sulfate ions embedded within the PANI layers allow for higher capacity and more rapid charge/discharge. This new mechanistic understanding is also expected to inform new studies and device designs to further understand and harness these effects for improved electrochemical performance.

Chapter 3

OXIDATIVE MOLECULAR LAYER DEPOSITION OF CONJUGATED AMINE POLYMER THIN FILMS

3.1 Abstract

Conjugated amine polymers such as polypyrrole (pPy), and polyaniline (pAni) exhibit high electrochemical capacities, making them appealing as electrode materials for energy storage, electrochemical desalination, and chemical sensing. Nanoscale thin films of these polymers are attractive to provide lower weight, faster charging, and higher sensitivity in these applications. This report describes the first demonstration of molecular layer-by-layer growth of conjugated amine polymers using alternating gas-phase exposures of amine monomers and MoCl5 oxidant in a process termed oxidative molecular layer deposition (oMLD). Pyrrole (Py) and MoCl5 undergo self-limiting surface reactions by oMLD to form conformal pPy thin films, but oMLD using aniline (Ani) and p-phenylenediamine (PDA) monomers yield unexpected azo functionality. This is attributed to a MoCl5-amine surface adduct that directs polymerization near amine groups, producing azo groups for primary amines. oMLD pPy exhibits record 282 mAh/g capacity in aqueous electrolyte, and PDA/MoCl5 oMLD yields azo-polymers of interest as anode materials for alkali-ion batteries. Alternating between Py and PDA monomers during oMLD produces molecularly mixed copolymers with qualitatively different electrochemical responses from the isolated monomer structures. This work lays the foundation for the growth of conformal thin films of conjugated amine polymers with molecular-level control of composition and thickness.

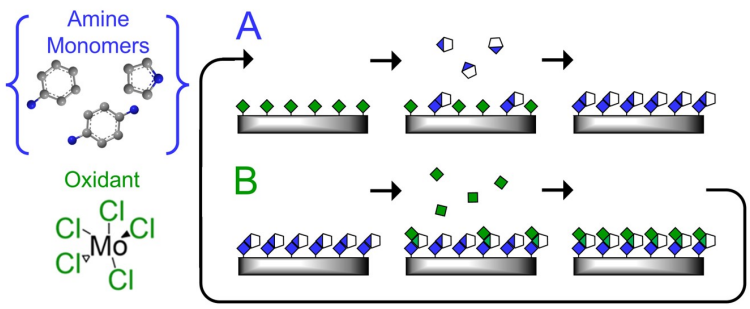

Figure 3.1: This work reports the first molecular layer-by-layer growth of redox-active amine polymers. This provides nanoscale conformal polymer films with rapid electrochemical charging, yielding record electrochemical capacities for polypyrrole. This process also provides molecular level control of polymer structure through the use of varying monomers, yielding polymers with tunable electrochemical properties over a wide range of potentials.

3.2 Introduction

Conjugated amine polymers formed from nitrogen-containing monomers are among the best-performing and lowest-cost active compounds for electrochemical energy storage[136], electrochemical desalination[137], and chemical sensors[138]. Polyaniline (pAni) and polypyrrole (pPy) are two of the most robust and well-studied conjugated amine polymers, initially discovered more than 150 years ago[139, 140]. Amine groups in these polymers undergo reversible electrochemical redox reactions under applied potential to switch between lone-pair and cation-radical configurations, yielding high electrochemical capacity of 150 mAh/g or 400 F/g (theoretically >400 mAh/g or >1500 F/g)[141]. These redox reactions also produce charge-carriers (electrons and holes) that travel down the conjugated backbone of these polymers to produce moderate electronic conductivities of 100s of S/cm[142, 143]. Following the recent demonstration of desalination batteries[144, 145] and anion-based batteries[146, 147], conjugated amine polymers have also gained renewed interest for their ability to reversibly bind anionic molecules from solution during electrochemical cycling (where the cation-radical form of amines attract and bind negatively charged anions). However, in a fully charged or fully discharged state, conjugated amine polymers become electrically resistive[148, 149] and require a conductive underlayer to realize their full electrochemical capacities. Anions also diffuse slowly through these polymers (solid state diffusivity of 10-15 cm^2/s at room temperature), introducing overpotentials in bulk polymers and leading to poor device performance[150, 151, 152]. As such, delivering thin-film conjugated amine polymer coatings onto powder or porous conductive supports is attractive to maximize power and energy density. Unfortunately, traditional approaches for conjugated amine polymer synthesis struggle to deliver uniform thin film coatings onto 3D substrates. Conjugated

amine polymer synthesis is traditionally performed by solution-phase homogeneous oxidation using chemical oxidants such as ammonium persulfate (APS) or Iron(III) chloride (FeCl3)[153]. The polymerization process is initiated through chemical oxidation of monomers, followed by combination with other monomers or short chain oligomers to continue chain propagation[154, 155, 156]. However, this synthesis approach does not easily allow for formation of polymer films – instead yielding irregularly-shaped particles or nanofibers[157, 158], which must be dissolved, e.g. in m-cresol, and spin-coated to produce ($>$ 1 m roughness) films[159, 160]. This approach is not easily applied to 3D substrates. Conjugated amine polymer synthesis can also be achieved using electrodeposition, which provides some control over polymer film thickness, e.g. by pulse deposition[161], but this approach is restricted to a subset of conductive substrates and delivering coatings onto porous supports via electrodeposition is challenging[162, 163]. Over the last 30 years, vapor-phase polymerization (VPP) has been under development to form conjugated polymers in the gas phase, absent of solution[164, 39, 165]. These studies have primarily focused on homogeneous vapor-phase mixing of monomer and oxidant in a process termed oxidative chemical vapor deposition (oCVD). Vapor-phase oCVD has been demonstrated for pPy[166], pAni[39], and polyethylenedioxythiophene (pEDOT)[167], yielding properties superior to solution-phase polymerization due to the absence of side-chains or additives needed for solution processing[168]. While VPP provides a route for greater control over the uniformity and thickness of conjugated amine polymer films, established oCVD deposition techniques are limited in their application to 3D substrates by the line-of-sight nature of this deposition process[169]. More recently, it was demonstrated that the gas phase precursors used in oCVD can be delivered as alternating chemical exposures separated by an inert purge step to grow films, in a process termed oxidative molecular layer deposition (oMLD)[170, 171]. oMLD stems conceptually from atomic layer deposition (ALD)[172, 173, 174] and is an extension of the sub-class of ALD known as molecular layer deposition (MLD)[175, 176, 177, 175]. In ALD, organometallic precursors and coreactants (e.g. water) are dosed in sequential gas-phase exposures and undergo self-limiting (typically ligand exchange) surface reactions to produce thin films with atomic-scale control of thickness. In MLD, the process is analogous to ALD, but employs molecular reactants, where complementary bifunctional organic molecules are delivered in sequential gas-phase exposures to grow polymer films. For example, alternating exposures of adipoyl chloride (a bifunctional acyl halide) with 1,6 hexanediamene (a bifunctional primary amine) react to form R-C-O-N-C-R linkages at the surface and produce the nylon 66 polymer[175].The self-terminating surface reactions in this process allow for the formation of uniform coatings on complex 3D surfaces[171, 178, 179]. oMLD is similar to conventional MLD, but employs a monomer and gas-phase chemical oxidant to oxidize

surface monomers and drive radical polymerization. To date, pEDOT is the only polymer that has been demonstrated using the oMLD technique[170]. oMLD of pEDOT promotes greater packing densities producing more crystalline pEDOT with higher electronic conductivities relative to solution phase formation, and by the nature of the process, can be easily applied to 3D substrates[145]. Here, we study whether conjugated amine polymers including pPy and pAni can be formed by oMLD. These conjugated amine polymers have maximum theoretical charge storage capacities of 412 mAh/g (1850 F/g) and 294 mAh/g (1500 F/g), respectively assuming that every monomer is active. These values are 50-100% larger than the maximum value of 191 mAh/g (860 F/g) for pEDOT. (We note that in practice, only one third to one half of monomers are found to be active for these redox-active polymers such that practical limits for charge storage are lower than these values[141].) In addition to the higher theoretical charge-storage capacities of polymers made from pyrrole (Py) and aniline (Ani), these monomers are lower-cost and offer improved environmental safety over ethylenedioxythiophene (EDOT). However, prior to the present work, it was unclear whether amine-based monomers would be viable for growth by oMLD. In this work, we examine (1) the self-limiting nature of these oMLD chemistries, (2) the chemical mechanism for oMLD growth using amine-based monomers, and (3) the electrochemical properties of the resulting films. We reveal new insights into the chemical mechanisms for oMLD using amine monomers and identify monomer-dependent differences in growth yielding unexpected polymer structures with valuable electrochemical properties. oMLD reactions were conducted in a hot walled ALD-type reactor[180], utilizing sequentially dosed chemical precursors separated by argon carrier gas at reduced pressures (0.8 Torr). Purging of the reactor between doses removes any excess monomer, oxidant, or volatile species formed during reaction. FeCl3 is a common oxidant for polymerization, however its low vapor pressure makes it less suitable for oMLD. A more volatile oxidant, such as the MoCl¬5 oxidant used in this work, is better suited for this gas-phase polymerization technique[170].

3.3 Materials And Methods

3.3.1 oMLD Reactor Conditions

oMLD in this work was carried out using a custom hot-walled viscous-flow MLD reactor. The deposition temperature of the main reaction chamber was held at temperatures between 100°C and 200°C using PID temperature controllers. Py (98%, Fischer Scientific) was held at room temp, while Ani (99.9%, Fischer Scientific), PDA (97+%, Fischer Scientific), and MoCl5 (99.6%, Fischer

Scientific) were held at 80 °C, each in a jacketed flow-over precursor bubbler with PID temperature control. The peak dose pressures of Py, Ani, PDA, and MoCl5 were 100 mTorr, 15 mTorr, 10 mTorr, and ¡5 mTorr, respectively. 200 sccm of continuous Ar carrier gas flow was used during depositions to maintain a baseline pressure of 0.8 Torr. Prior to each deposition, the reactor and sample tray were passivated with at least 150 oMLD cycles of the target chemistry. Substrates used for various depositions included Si pieces (Silicon Valley Microelectronics), AAO membranes (InRedox), quartz wafers (Valley Design), and PGS (Newark). The samples were pre-heated in the reaction chamber under inert carrier gas purge for at least 30 min prior to deposition. During each oMLD growth, the monomer (A) and oxidant (B) were dosed sequentially in A/B precursor cycles, with a purge step between each precursor dose. A typical dosing scheme for one oMLD cycle consisted of 10 s of monomer dose, 100 s of Ar purge, 100 s of MoCl5 oxidant dose, and 100 s of purge. These cycles were repeated to increase the thickness of the resulting polymer films. Dose and purge times varied based on monomer and temperature used during deposition, as indicated in the manuscript text.

3.3.2 Electrochemical Measurements

Three-electrode electrochemical measurements were carried out on PGS substrates in a custom electrochemical cell. The electrochemical cell provided an o-ring seal on the sample surface to expose a defined 1.21 cm2 surface area to the electrolyte solution. 0.1 M NaCl aqueous electrolyte adjusted to a pH of 3.5 was used for aqueous electrochemical experiments. The electrolyte solution was purged for at least 30 minutes prior to electrochemical measurements, and a continuous Ar purge was used in the head-space of the electrochemical cell during electrochemical measurements. A graphite rod counter electrode (99.999%, Fischer Scientific) and Ag/AgCl reference electrode were used. CV experiments were performed at a sweep rate of 50 mV/s over a potential range of -0.75 to 0.75 V vs. Ag/AgCl unless otherwise noted. Non-aqueous electrochemical experiments were performed under inert argon atmosphere (¡0.5 ppm H2O, ¡0.3 ppm O2) in a glovebox. A 0.1 M NaClO4 in anhydrous, amine free acetonitrile (Alfa Aesar, 99.9%) was employed as an electrolyte. A custom glass three-electrode cell was used for electrochemical experiments with a graphite rod as the counter electrode (99.5%) and a non-aqueous Ag/AgNO3 reference electrode (BASi). CV experiments were performed at a scan rate of 20 mV/s within a voltage window no greater than -3.0 V and 1.0 V vs Ag/AgNO3. The Ag/AgNO3 reference potential was calibrated using ferrocene to report potentials vs. Na/Na+. The specific capacity, CC, and specific capacitance, CF, of films reported in the text were calculated as $C_C = Q/Ah$ and $C_F = Q/VAh$, where Q is the total charge transferred on

the charging sweep (cathodic sweep for aqueous electrolyte, and as-specified above for nonaqueous experiments), V is the potential window (1.45 V, -0.75 +0.70 V vs. Ag/AgCl for aqueous electrolyte, and as-specified above for non-aqueous experiments), is the density of the film (taken as 1.5 g/cm3 for pPy [181, 182] and 1.1 g/cm3 for pPDA based on typical pAni densities[183, 184], and 1.3 g/cm3 for the molecular-mixed copolymers), A is the cross-sectional area of film exposed to the electrolyte (1.27 cm2), and h is the film thickness for each sample as measured by SE on Si witness wafers, and benchmarked using NR and SEM.

3.3.3 Neutron Spectroscopy

NR data was obtained using the Grazing Incidence Neutron Spectrometer (GANS) at the University of Missouri Research Reactor (MURR)[184]. Analysis was done through the Reflpak suite[185] which uses the Parratt method[186]that recursively accounts for the film layers and interfaces to construct a final film density profile. The fringe spacing in the reflectivity curves is a product of the layer thickness.

3.3.4 Scanning electron microscopy (SEM)

Scanning electron microscopy (SEM) was used to evaluate deposited thickness using a FEI Scios Dual Beam FIB SEM. High contrast SEM images of the deposited polymer film were visualized under 5 keV under high vacuum inert conditions. PGS and AAO samples were cleaved to visualize film thickness. The film thicknesses were measured using ImageJ.

3.3.5 Spectroscopic ellipsometry (SE)

Spectroscopic ellipsometry (SE) analysis and modeling were conducted using an Alpha SE system (J.A. Woollam) at an incident angle of 65o, at room temperature and open to the air and modeled using the CompleteEASE software package. The optical properties and thickness were modeled using a Cauchy-Urbach dispersion model of the form $n() = A + B/2 + C/4 and k() = exp((12400(1/ - 1/)))$ where is the wavelength; A, B, C, , and are fitted constants to minimize error relative to NR measurements; and is the band edge wavelength, taken as 350 nm for oxidized pPy.[187] Fitted values for pPy at 100°C were A= 1.678, B = 1.631 × 10-2, C = 4.0814 × 10-3, = 2.4052 × 10-1, =6.17 × 10-1. Fitted values for pPy at 150°C were A= 1.807, B = 1.297 × 10-1, C = -1.506 × 10-2, = 5.8083 × 10-1, =2.618.

3.3.6 Raman spectroscopy

Raman spectroscopy was conducted with a Renishaw inVia Raman spectrometer using excitation from a 633 nm laser and Raman spectra were collected over 500-2000 cm-1 with a spectral resolution of 10 cm-1. Spectra were acquired using a sweeping scan of 10 cm-1/s and a laser power of 10.1 mW.

3.4 Results And Discussion

3.4.1 Benchmarking oMLD Growth of Polypyrrole

Figure 1 depicts in situ quartz crystal microbalance (QCM) results during steady-state oMLD growth of Py/MoCl5 at 100°C using an 8 s Py dose 200 s Ar purge, 55 s MoCl5 dose, and 200 s purge for each oMLD cycle. The steady state mass gain per cycle (MGPC) over the 22 oMLD cycles shown in Figure 1a is 113 ng/cm2/cycle. In Figure 1b and 1c, we show average QCM traces during MoCl5 and Py doses. These QCM data represent average traces at steady state following 50 oMLD cycles. We observe self-limiting behavior during both the MoCl5 dose (Figure 1b) and the Py dose (Figure 1c). During the MoCl5 dose (Figure 1b), we see that the mass increases and plateaus, yielding a final mass gain of 300 ± 4.6 ng/cm2 after 100 s of MoCl¬5 dose time, or about 1.5 monolayers (taking the height of an MoCl5 octahedron to be 4.546 Å, the Cl- ionic radius to be 1.81 Å, and the density of MoCl5 to be 2.48 g/cm3)[188, 189, 190]. Following 60 s of MoCl5 dose, the mass gain has reached 85% of the final value, suggesting that a 60 s dose time is sufficient to provide a saturating dose of MoCl5. We also observe a 20 s lag in the QCM data before the mass starts to increase in Figure 1b, which we attribute to the low (<5 mTorr) partial pressure of the MoCl5 precursor. We expect that the low vapor pressure of MoCl5 necessitates a longer dose time to titrate the reactor walls and react on the QCM crystal placed downstream in the reactor. During the Py dose (Figure 1c), we see that the mass decreases and plateaus, yielding a final mass loss of 93 ± 2.3 ng/cm2 after 8 s of Py dose time. We expect the mass loss arises because MoClx and/or HCl is liberated when Py reacts on the surface and is oxidized by MoCl5 to form a Py-Py dimer. After 6 s of Py dose time, the mass loss has reached 87.3% of the final value, indicating that 6 s of Py dose is sufficient to provide a saturating dose of Py. Based on the results in Figure 1b and 1c, a MoCl5 dose time of 60 s and a Py dose time of 6 s was used in subsequent depositions. The linear increase in mass with increasing oMLD cycle numbers in Figure 1a, and the saturating and self-limiting behavior during MoCl5 and Py doses in Figure 1b/1c are hallmarks of ALD/MLD processes[172, 173, 174] and suggest that the Py/MoCl5 oMLD chemistry can be used to form uniform and conformal thin films on high surface

area substrates with nanoscale control of thickness.

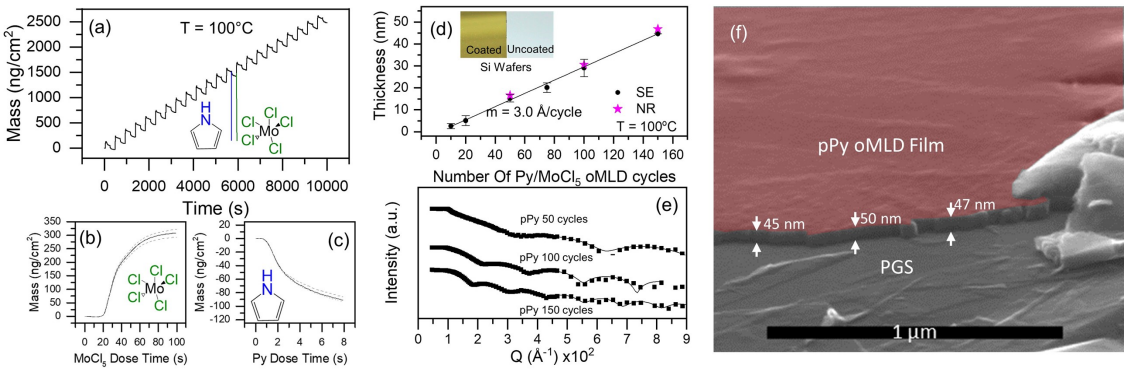

Figure 3.2: Characterization of Py/MoCl5 oMLD at 100o C including (a) QCM during 22 Py/MoCl5 oMLD cycles, (b) QCM mass change during MoCl5 dose averaged over 5 oMLD cycles at steady-state, (c) QCM mass change during Py dose averaged over 5 oMLD cycles at steady-state, (d) thickness vs. number of Py/MoCl5 oMLD cycles as measured by SE and NR with inset showing photographs of Si coated with 100 oMLD cycles of Py/MoCl5 vs. uncoated Si wafer, and (e) raw NR data for 50, 100, and 150 oMLD cycles of Py/MoCl5 including model fits corresponding to thicknesses shown in (d). Also shown (f) is SEM imaging (colorized) of cleaved PGS with pPy oMLD film formed by 150 Py/MoCl5 oMLD cycles at 100 °C showing uniform conformal coating.

Based on the linear growth and saturating exposures observed in Figure 1a-c, we expect to be able to control film thickness of polypyrrole (pPy) films by adjusting the number of Py/MoCl5 oMLD cycles. To confirm the control over film thickness, we performed varying numbers of oMLD cycles on silicon (Si) wafers and evaluated the resulting film thickness ex situ using spectroscopic ellipsometry (SE) and neutron reflectivity (NR) in Figure 1d. In Figure 1d, we observe a linear increase in film thickness with an increasing number of oMLD growth cycles—as expected for controlled MLD growth. A linear fit of the SE data in Figure 1d yields a growth rate of 3.0 Å/cycle. This corresponds closely to the diameter of a Py monomer of 3.91 Å,[191, 192] and indicates that 0.8 monolayers of pPy is formed per oMLD growth cycle at 100°C. We also show the raw NR data (background subtracted, footprint corrected, and normalized) with model fits for select pPy films in Figure 1e. These NR data show an increased number of Kiessig fringes over the same Q-range with an increased number of oMLD cycles, indicating an increased film thickness. The well-defined Kiessig fringes are indicative of smooth films, and indeed, modeling of this NR data yielded an RMS roughnesses of 0.86 nm for a 46.2 nm thick film (150 oMLD cycles). The NR and SE thicknesses agree closely in Figure 1d. In Figure 1f, we also confirmed by scanning electron microscopy (SEM) that the thickness of oMLD films deposited on Si wafers in Figure 1d is consistent with films formed on pyrolytic graphite sheet (PGS) carbon substrates used for electrochemical measurements. In Figure 1f we measure a film thickness of 47 ± 2 nm of pPy on PGS after 150 Py/MoCl5 oMLD cycles at 100°C, which is consisted

with the SE thickness of 44.7 nm measured on Si. To deploy this oMLD pPy growth process to coat high-surface-area (e.g. powder carbon) electrodes (or other high-surface-area substrates), it is necessary to increase the purge times following precursor doses to sufficiently evacuate voids in these three-dimensional porous structures[192, 193]. In this context, it is critical that each precursor exposure in the oMLD results in strong chemisorption/chemical reaction with the substrate surface to enable uniform and conformal growth on 3D substrates even with long purge times. In Figure 2a, we plot the MGPC for the Py/MoCl5 oMLD process versus purge time from 10 to 200 seconds. We find that the MGPC decreases from 561 ng/cm2/cycle at a 10 s purge time down to a constant value of 120 ng/cm2/cycle for purge times 120 s. This suggests that shorter (<120 s) purge times produce gas-phase mixing of precursors to yield uncontrolled chemical vapor deposition (CVD), whereas purge times 120 s result in stable MLD surface reactions[194]. In Figure 2b we plot the thickness observed on Si wafers positioned at 10 cm intervals down the 50 cm length of the sample tray within the reactor. Interestingly, we observe that shorter (<20 s) purge times produce uniform film thicknesses down the length of the reactor despite the CVD-like process at this purge time. We expect that the pyrrole monomers have a short-lived (e.g., multilayer adsorption) process that produces uniform thickness at these shorter purge times.

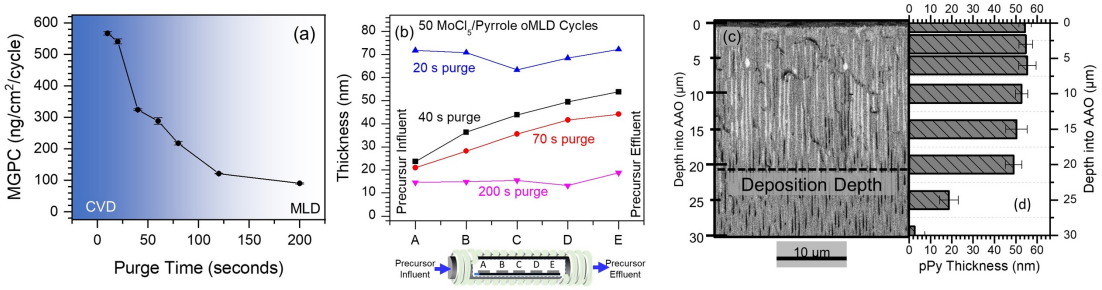

Figure 3.3: Demonstration of stable growth at high purge times, including (a) MGPC vs. purge time for Py/MoCl5 oMLD using constant 10 s Py dose and 100 s MoCl5 dose (b) measurements of thickness of pPy films on Si samples over the length of entire coating chamber after 50 Py/MoCl5 oMLD cycles using different purge times and , (c) SEM profile of pPy film after 150 Py/MoCl5 oMLD cycles on cleaved AAO substrate (side on view) with the pPy thickness vs. depth into the substrate as measured from SEM image.

For purge times of 40 s and 70 s, we observe a gradient in thickness with thinner (20 nm) films closer to the precursor influent and thicker (50 nm) films closer to the effluent in Figure 2b. We attribute this effect to surface species slowly desorbing from the sample surfaces for purge times $>$ 20 s and $<$ 100 s, starting upstream and propagating downstream, resulting in a nonuniform growth profile. For a purge time of 200 s, the thickness profile is constant at 12 $\pm$ 0.67 nm down the length of the reactor, indicating a stable MLD process based on irreversible chemisorption of each

precursor. Based on the indications of stable MLD growth for purge times 120 s in Figure 2a and 2b, a purge time of 120 s was used for all subsequent depositions. Based on the convergence to stable growth at high purge times in Figure 2a and 2b, we expect that this oMLD process should provide uniform growth even on high-surface area porous/3D substrates. To test this, we deposited 150 oMLD cycles of MoCl5/Py onto anodic aluminum oxide (AAO) membrane of 50 m thickness with 200 nm pores running axially through the membrane. In Figure 2c we show a scanning electron microscope (SEM) cross-section of the AAO membrane obtained using backscattered electrons following oMLD deposition. In this SEM image, the oMLD film is visible by contrast as a white layer due to MoClx residue left in the film following deposition (vide infra). The oMLD film is visible down to a depth $>$ 20 m into the AAO membrane. In Figure 2d, the thickness of the oMLD film on the walls of the AAO pores is plotted as a function of depth into the AAO substrate, as measured from the SEM image in Figure 2c. In Figure 2d, the thickness of the pPy film remains at 52 nm $\pm$ 3.4 nm to a depth of 20 m, and drops to a thickness of 19 nm at a depth of 25 m. The thickness of 52 nm after 150 oMLD cycles in Figure 2d corresponds to a growth rate of 3.5 Å/cycle, in close agreement with the value of 3.0 Å/cycle measured on Si in Figure 1d. The uniform 52 nm film formed to a depth of 20 m corresponds to an aspect ratio of 100:1 at the onset of deposition, and an aspect ratio of 200:1 at the end of film growth (50 nm of film thickness on the walls of the pores reduces the pore diameter from 200 nm to 100 nm). Based on diffusion/reaction modeling of ALD within nanoporous structures (not shown)[195, 196], we expect that the aspect ratio of uniform deposition is limited by the low ($<$5 mTorr) partial pressure of the MoCl5 precursor. The ability to grow uniform thin-film pPy materials by oMLD onto carbon substrates as depicted in Figure 1 and onto porous substrates in Figure 2 makes this process attractive for use in generating electrode materials in aqueous energy storage devices, electrochemical desalination, chemical sensors, and other electrochemical applications. Previous work has shown that the deposition of thin-film inorganic redox-active layers by ALD reduces the length-scale for slow solid-state ion diffusion to yield high capacity and high rate energy storage and deionization electrodes[165, 39, 197, 198]. Here, the demonstration of oMLD of pPy provides an analogous route to form redox-active polymer layers with high electrochemical capacities[199, 200], but using organic precursors that are lower cost than organometallic precursors used to form inorganic redox-active layers by ALD. To highlight the benefits of using oMLD to form thin pPy films, we measured the electrochemical capacity in Figure 3 of multiple samples of thinner (5.5 $\pm$ 0.2 nm) pPy thickness deposited on PGS at varying CV sweep rates. In Figure 3a we depict the third CV sweep of these oMLD films at 100 mV/s, 200 mV/s, and 300 mV/s sweep rates. This third-CV sweep rates were used to establish the capacity vs. sweep rate in Figure 3b. We find that a sweep rate of 10 mV/s

(145 s charge time) produces a charge capacity of 282 mAh/g (68% of pPy's theoretical capacity), and the pPy films maintain a charge capacity of 211 mAh/g (50% of pPy's theoretical capacity) at a charge rate of 500 mV/s (2.9 s charge time). Here, increasing the charge rate by 50× from 10 mV/s to 500 mV/s only led to a 25% reduction in charge capacity. A log-log analysis of current vs. sweep rate[39] for the data in Figure 3b (not shown) identifies that the charge storage for these 5.5 nm pPy films exhibits 15% diffusive and 85% capacitive behavior – indicating rapid charging of these thin redox-active layers. We note that the double layer capacity of bare PGS substrates corresponded to only 10% of the total capacity at 10 mV/s sweep rate and 5% of the total capacity at a 500 mV/s sweep rate – a small fraction of the capacitive charge storage from the log-log analysis. These results show promise for using ultra-thin oMLD pPy films to produce high-rate electrochemical devices.

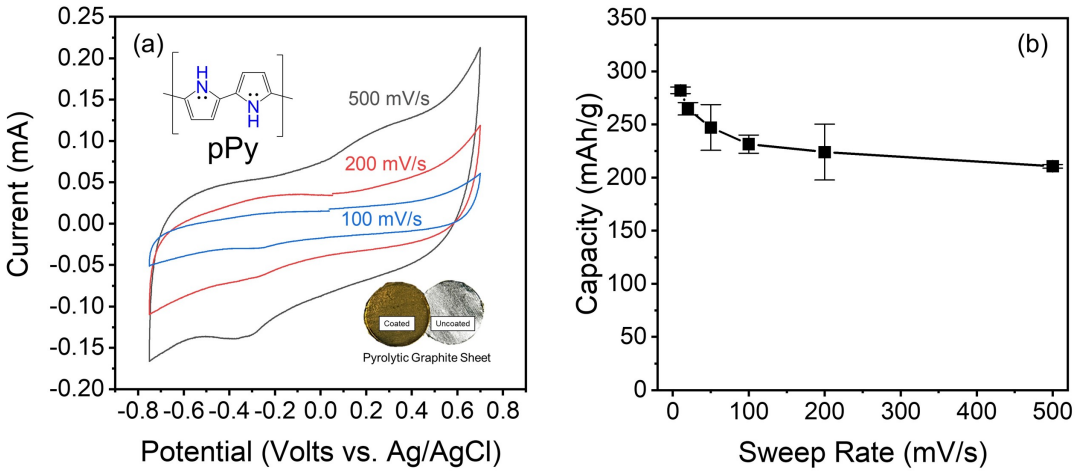

Figure 3.4: Impact of sweep rate on charge storage capacity of 5.5 nm thick pPy films formed by oMLD on PGS at 150°C including (a) example CV curves performed at varying sweep rates and (b) corresponding charge capacities from the third CV cycle for triplicate samples with sweep rates in randomized order between samples. The inset on the bottom-right of (a) shows PGS before and after Py/MoCl5 oMLD with a visible change in color from the deposited film.

We emphasize that the electrochemical capacities we measure in Figure 3 are as high as 282 mAh/g. This is 2× higher than typical values of the electrochemical capacity reported for pPy formed by other synthesis methods. For reference, assuming every nitrogen atom yields one stoichiometric electron transfer, the maximum theoretical specific capacity for pPy is 412 mAh/g. However, typical values of charge storage capacity for pPy are closer to 140 mA/g.[141, 201] The practical limit of 140 mAh/g has been is thought to originate from the electronic configuration of monomers, limiting the activity to 1/3 of amine groups within the polymer[141]. The 2× enhancement in electrochemical capacity for pPy deposited by oMLD relative to other deposition methods suggests that forming ultrathin films

may enable us to access higher capacities than previously thought possible for conjugated polymers. We expect that the uniform, thin-film pPy layers produced here (see Figure 1f) eliminate wasted material, and reduce the length scale for ion and electron transport, allowing for faster charging.

3.4.2 Contrasting oMLD Growth of Aniline and Paraphenylenediamine

After establishing oMLD chemistry for Py using the MoCl5 oxidant, we were interested whether this oMLD scheme was also viable to form polyaniline (pAni) using sequential doses of aniline (Ani) and MoCl5. In Figure 4a, we report the MGPC for oMLD of Py/MoCl5 and Ani/MoCl5 vs. growth temperature. Based on previous description of the oMLD growth mechanism[170], we expected that either Ani or Py would result in similar growth behavior to EDOT. And indeed, the growth of pPy is consistent with our expectations as outlined in Figure 1. However, interestingly Ani/MoCl5 oMLD exhibited exponential/compounding mass gains for Ani/MoCl5 oMLD at low (100°C) temperature, where the mass gain upon each subsequent oMLD cycle was approximately double the value measured on the previous cycle, reaching a value of >1,000 ng/cm2 within 10 oMLD cycles. This behavior yields high variability in MGPC shown in Figure 4a for Ani/MoCl5 oMLD. This exponential increase in mass gains was observed repeatedly on in-situ QCM experiments and confirmed using ex-situ SE measurements on Si wafers. We attributed the exponential growth behavior at 100°C to chemisorption of the MoCl5 precursor to R-NH2 groups throughout the bulk of the film[202, **?**, 203]. At growth temperatures of 150°C and 200°C, we observed a linear growth of 99 and 110 ng/cm2/cycle, respectively, for Ani/MoCl5 oMLD. We expect that these elevated temperatures help to drive off MoCl5 from the film and lead to this linear growth behavior and lower MGPC. However, the MGPC at 200°C is greater than the MGPC measured at 150oC for both Ani and Py monomers, which is not consistent with our expectations based on expected MoCl5 desorption behavior.

To better understand the increase in MGPC at 200°C vs. 150°C in Figure 4a, we performed X-ray photoelectron spectroscopy (XPS) measurements on films grown using Py/MoCl5 oMLD at 100, 150, and 200°C as reported in Figure 4b. The 100°C growth temperature was found to result in 14.6% Mo within the film vs. 3.6% and 3.3% at growth temperatures of 150°C and 200°C, respectively. This is consistent with our expectation that more MoCl5 sorbs into the film at low deposition temperatures. We also note that the highest O content was observed at a deposition temperature of 100°C. This arises from the reaction of residual MoCl5 with air to form MoOxCly, as confirmed by the presence of an O 1s peak at a binding energy of 232 eV in this sample, consistent with MoOx[204]. We find

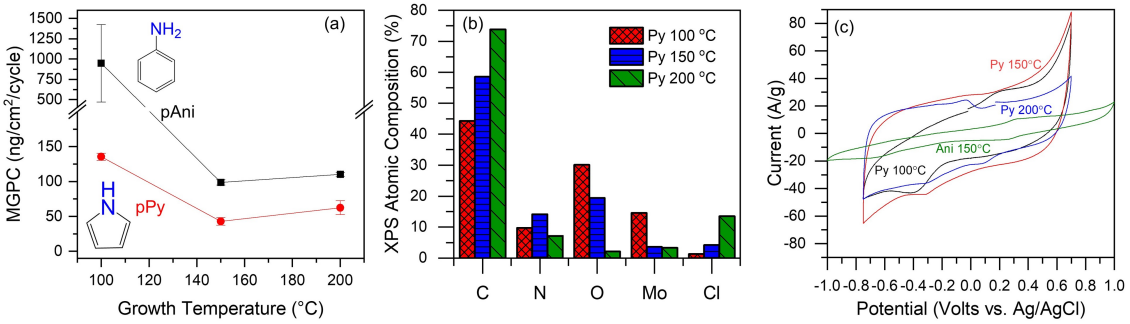

Figure 3.5: Effect of growth temperature on conjugated amine polymer oMLD including (a) MGPC of Ani/MoCl5 and Py/MoCl5 oMLD vs. growth temperature, (b) XPS analysis of oMLD pPy films as deposited at 100, 150, 200o C, and (c) CV of pPy formed at 100, 150, 200o C, and Ani/MoCl5 oMLD film deposited at 150°C. CV experiments in (c) were performed at a sweep rate of 50 mV/s in 0.1 M NaCl electrolyte adjusted to a pH of 3.5.

that the C:N molar ratios for the Py/MoCl5 films deposited at 100°C and 150°C are 4.56 and 4.13, respectively—in close agreement with the value of 4.00 expected for a pPy film. In contrast, the film deposited at 200°C exhibits a C:N molar ratio of 10.33, indicating decomposition of the Py monomers at this elevated temperature. Likewise, the growth temperature of 200°C yields the highest Cl content of 13.54%, suggesting chlorination of the hydrocarbon backbone, as confirmed by Cl 2p peaks at binding energies of 200 and 202 eV, consistent with chlorinated hydrocarbons[205]. Based on these observations, we expect that the increase in growth rate at 200°C vs. 150°C for both Py and Ani arises from thermochemical decomposition of Ani/Py monomers at 200°C during the oMLD growth process. To relate the composition information obtained in Figure 4b with changes in material properties, we performed electrochemical analysis of films deposited at 100°C, 150°C, and 200°C for the Py/MoCl5 oMLD chemistry in Figure 4c. Here, the growth rate varies with temperature, and so we adjusted the number of oMLD cycles at 100 and 150°C such that the final film thickness was roughly equivalent between these samples. We observed little electrochemical response for Py/MoCl5 oMLD films deposited at 200°C, so we increased the film thickness at this deposition temperature. 50, 75, and 200 oMLD cycles at 100, 150, and 200°C yielded films of 7.2, 7.6, and 23.7 nm thickness by SE, respectively in Figure 4c. We found that Py/MoCl5 oMLD films deposited at all three growth temperatures exhibited electrochemical activity. The cyclic voltammetry (CV) cycle in Figure 4c for a growth temperature of 100°C corresponds to a charge storage capacity of 211 mAh/g (524 F/g). We observe irreversible charge storage (a separation between the oxidation and reduction peaks) for this growth temperature, which we attribute to a poorly connected pPy network arising from MoClx residue in the film. This poorly connected pPy network is also supported by the observation of rapid degradation in the specific capacity of the oMLD Py/MoCl5 films grown at 100°C, where 50% of

the capacity was lost within 10 CV cycles. A growth temperature of 150°C for Py/MoCl5 oMLD yielded a specific capacity of 260 mAh/g (646 F/g) for the CV in Figure 4c, and exhibited reversible rectangular-shaped pseudocapacitive behavior, with a visible redox feature at an equilibrium potential of -0.2 V vs. Ag/AgCl—in agreement with the known electrochemical properties of pPy[206]. A growth temperature of 200°C yielded a lower specific capacity of 180 mAh/g (448 F/g), arising from monomer decomposition at this elevated deposition temperature. The electrochemical capacity of oMLD pPy formed at 150°C is 2× higher than typical values of 140 mAh/g (400 F/g over 0.8 V window) for pPy,[207] which we attribute to the thinner films employed here enabled by the oMLD process. While Py/MoCl5 produced redox activity in line with our expectations for the formation of pPy, the Ani/MoCl5 films did not exhibit the expected electrochemical activity in aqueous electrolyte regardless of the growth temperature employed. The CV data for an Ani/MoCl5 film deposited at 150°C is shown in Figure 4c, corresponding to a specific capacitance of <100 mAh/g. The Ani/oMLD film also does not exhibit redox features at 0.13 V and 0.41 V vs. Ag/AgCl expected for pAni at the pH of 3.5 employed in these experiments[208, 209]. The Ani/MoCl5 film deposited at 100°C exhibited lower electrochemical capacity than the control PGS substrate. Based on the limited electrochemical response for Ani/MoCl5 oMLD films relative to the Py/MoCl5 oMLD films, we hypothesize that the local geometry of the monomer influences the reaction pathway for polymerization by oMLD. Specifically, we expect that MoCl5 binds to surface amine groups and forms an –R-NHx-MoCl5 surface adduct[202, **?**, 203], and we postulate that this surface adduct drives polymerization at sites adjacent to the amine, near the MoCl5 surface species. For the Py monomer, the favorable sites for polymerization are at the alpha carbons adjacent to the amine, and an MoCl5 surface adduct is expected to allow coordination of two monomers on the surface to allow this polymerization, as depicted in Figure 5a. In contrast, the favorable polymerization site for the Ani monomer in solution-phase reactions is at the para position on the benzene ring opposite the amine, but when two Ani molecules coordinate with one MoCl5 in a surface adduct, reaction at this para position is not viable, as depicted in Figure 5b.

Based on the analysis of how MoCl5 is expected to coordinate with Py and Ani monomers in Figure 5a and 5b, we hypothesized that although Ani does not react to produce pAni by oMLD, the p-phenylenediamine (PDA) monomer would exhibit oMLD growth with MoCl5 to yield redox-active poly-PDA (pPDA) films as depicted in Figure 5c. The PDA monomer is a derivative of Ani with a second amine group in the para position. The presence of this second amine group in the para position drives favorable polymerization at the four free carbons on the benzene ring highlighted in green in Figure 5c to form phenazine moieties as depicted in Figure 5c[210]. The reaction at these

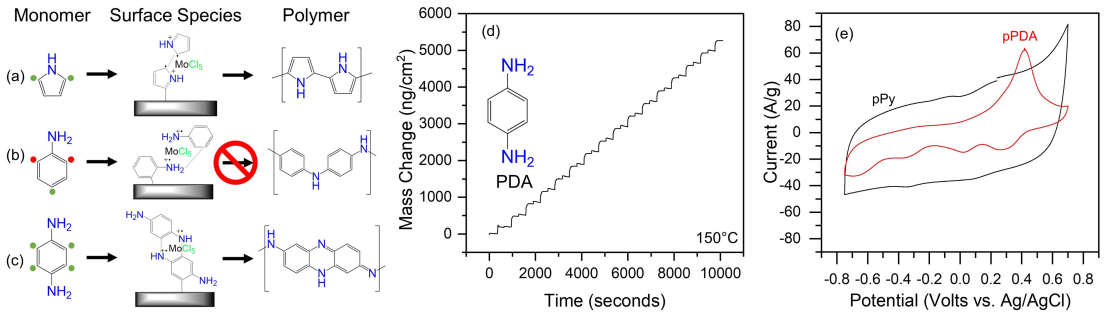

Figure 3.6: Proposed surface species of MoCl5 coordinating with (a) Py, (b) Ani, (c) PDA identifying that Py and PDA commonly react adjacent to the amine but Ani does not. This concept is consistent with (d) QCM growth study of pPDA at 150o C showing facile nucleation and growth of pPDA by oMLD and (e) CV of oMLD pPDA film showing redox activity. CVs in (e) were performed at 50 mV/s in 0.1 M NaCl electrolyte.

sites is also viable based on the surface coordination with MoCl5. In Figure 5d, we depict QCM data of the steady-state oMLD growth of PDA/MoCl5 at 150°C. We observe saturating dose behavior for both precursor exposures, and linear growth with an MGPC of 251 ng/cm2. In Figure 5e we depict CV measurements in aqueous electrolyte for a pPDA film grown by oMLD. We observe four distinct redox features for the pPDA oMLD film on a reducing sweep from +0.70 -0.75 V vs. Ag/AgCl, consistent with a blend of primary amines and phenazine groups within pPDA[211, 212, 213]. This result confirms that oMLD using the PDA monomer is viable for producing redox-active films and supports our hypothesis that the MoCl5 adduct drives polymerization at sites adjacent to the amine. However, interestingly, the capacity of the pPDA oMLD film is 100 mAh/g, only 20% of its maximum theoretical capacity of 500 mAh/g (assuming two redox-active amines per monomer). In contrast, the oMLD pPy film in Figure 5e achieved 63% of the maximum theoretical capacity of pPy.

3.4.3 Formation of Azo Groups for Primary Amines

Based on the understanding that MoCl5 forms a surface adduct with amine groups to drive polymerization adjacent to these groups, we hypothesized that primary amine (R-NH2) groups in Ani and PDA may also react to form azo (R-N=N-R) groups, explaining the limited redox activity for Ani/MoCl5 oMLD films in Figure 4c and PDA/MoCl5 oMLD films in Figure 5e. To examine this, we performed Raman spectroscopy on both Py/MoCl5 and Ani/MoCl5 oMLD films as depicted in Figure 6a-c and compared these against reference spectra for pPy and pAni. The Raman peaks for the Py/MoCl5 oMLD film are all consistent with the peaks expected for pPy as depicted in Figure 5a[214, 213]. Although Ani/MoCl5 oMLD Raman measurements reveal characteristic peaks for pAni in Figure 6b,[215] we also observe a clear peak at 1480 cm-1 in the Ani/MoCl5

Raman spectrum that is consistent with the azo (R-N=N-R) group in azobenzene.[216, 217] Unfortunately, the remainder of the Raman peaks for azobenzene overlap with peaks expected for pAni, except for strong peaks at 1575 and 1580 cm-1[217, 218], and these two peaks overlap with a peak from the pyrolytic graphite sheet (PGS) substrate employed in Figure 6b. To confirm the presence of azobenzene, we performed Raman spectroscopy on an Ani/MoCl5 oMLD film deposited on an AAO substrate in Figure 6c, where the AAO substrate does not interfere with peaks at 1575 and 1580 cm-1. Here, we observe clear features at 1575 and 1580 cm-1 for the Ani/MoCl5 oMLD film deposited on the AAO substrate and features consistent with all the dominant peaks in azobenzene, confirming that Ani/MoCl5 oMLD produces azobenzene. The oxidative formation of azo groups from amines has been described in prior work[219], and recent reports have shown formation of azobenzene by oxidation of aniline on Mo-based catalysts[220]. Despite this, the formation of azo groups by oMLD has not been described to date and provides a route to grow azo-polymers through layer-by-layer deposition using alternating exposures of primary amines and the MoCl5 oxidant. Just as the primary amines in Ani react during Ani/MoCl5 oMLD to produce azobenzene, we expected that the primary amines in PDA will also react with MoCl5 to form azo groups within pPDA – i.e. forming polyazobenzene-like domains[219]. The formation of thin-film polyazobenzene could be valuable for use in anode materials in alkali-ion (e.g. Li-ion) batteries due to the highly anodic (negative) redox potential of azo groups[217]. To identify whether azo groups were formed during PDA/MoCl5 oMLD, we performed nonaqueous electrochemical measurements on PGS substrates subjected to Ani/MoCl5 and PDA/MoCl5 oMLD

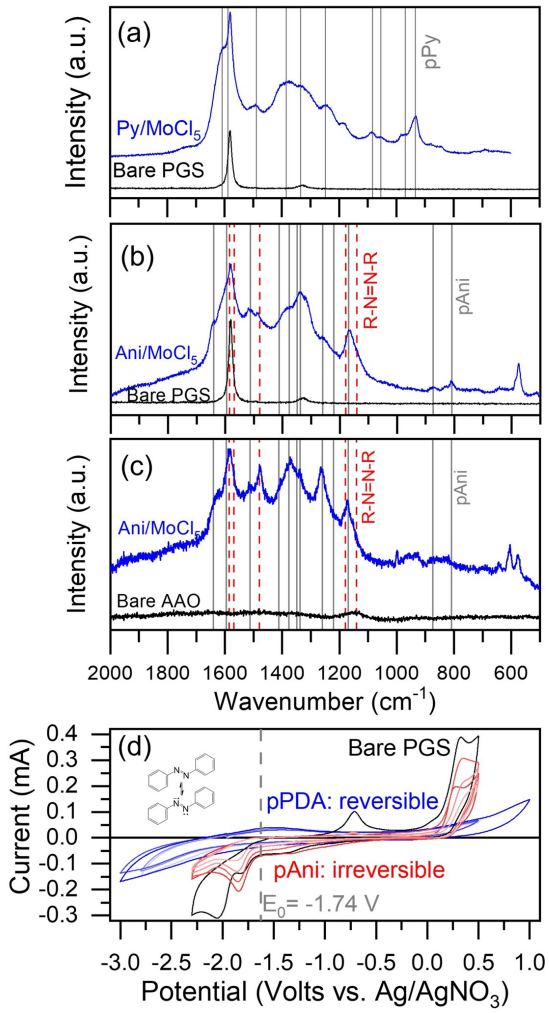

Figure 3.7: Raman spectroscopy results for (a) Py/MoCl5 oMLD film on PGS, (b) Ani/MoCl5 oMLD film on PGS, (c) Ani/MoCl5 oMLD film on AAO. Also shown are (d) CV experiments in nonaqueous acetonitrile electrolyte at a sweep rate of 50 mV/s for a 121 nm Ani/MoCl5 oMLD film on PGS (red), a 40.3 nm PDA/MoCl5 oMLD film on PGS (blue), and bare PGS substrate (black).

processes as depicted in Figure 6d to look for electrochemical signatures consistent with azo groups. We find that both Ani/MoCl5 and PDA/MoCl5 oMLD films exhibit electrochemical reduction at -1.74 V vs. Ag/AgNO3, consistent with reduction of azo groups to form anion radicals.. [86,87] This redox process is reversible in pPDA films with a capacity of 185 mAh/g measured on the oxidizing sweep (vs. 500 mAh/g max theoretical), and initial cycling results up to 10 CV cycles suggest that the azo groups are stable in the condensed phase formed by PDA/MoCl5 oMLD. We note that the electrochemical redox process at -1.74 V vs. Ag/AgNO3 is irreversible for Ani/MoCl5 oMLD films and decreases with repeated cycling. We attribute this decrease to the dissolution of azobenzene molecules upon electrochemical reduction to form azobenzene radicals. Because each Ani monomer has only one amine group, the reaction of two Ani molecules is expected to form azobenzene or short-chain azo oligomers that easily dissolve. This was confirmed by UV-Vis spectroscopy (not shown) of the electrolyte after CV cycling of the Ani/MoCl5 oMLD films, which showed an absorption peak at 300-350 nm, consistent with the presence of azobenzene.[88] We also observed visible loss of the deposited Ani/MoCl5 layer from PGS following electrochemical cycling for the area of the PGS sample exposed to the electrolyte. We note that the presence of redox activity in pPDA films under more positive potentials (-0.75 – 0.75 V vs. Ag/AgCl) in Figure 5e suggests that not all amine R-NH2 groups on PDA have reacted to form azo (R-N=N-R) groups during PDA/MoCl5 oMLD, instead producing a blend of both azo moieties (depicted in the inset of Figure 6d), and phenazine-like moieties (depicted as the product in Figure 5c). Based on the measured electrochemical capacities corresponding to phenazine (Figure 5e - 100 mAh/g) and azo (Figure 6d – 185 mAh/g) moieties, we expect that these groups exist in a 1:2 phenazine:azo molar ratio within PDA/MoCl5 oMLD films.

3.4.4 Formation of Molecularly Mixed Py/PDA Copolymers by oMLD

Based on the above understanding of the oMLD mechanism, we were interested whether introducing Py monomers during PDA/MoCl5 oMLD growth would result in molecularly mixed copolymers that block azo-formation and direct PDA to react to form phenazine-like moieties. As a first step to examine this, we examined whether oMLD growth using blended monomers was viable. For this, we performed oMLD growth while alternating between Py and PDA monomers in 1:1 cycle ratio and compared against Py-only and PDA-only oMLD growth as depicted in Figure 7. In Figure 7a, we depict QCM results during nucleation and growth of 20 Py/MoCl5 oMLD cycles and seven (Py/MoCl5):(PDA/MoCl5) super-cycles of the 1:1 cycle ratio at 150°C. The Py/MoCl5 oMLD chemistry exhibits a nucleation delay of 20 oMLD cycles and has a steady-state MGPC of 62 ng/cm2.

From the QCM data above in Figure 5b, PDA/MoCl5 oMLD has a steady state MGPC of 251 ng/cm2 at this growth temperature and exhibits no nucleation delay. The Py/PDA copolymer formed using a 1:1 cycle ratio exhibits no nucleation delay in Figure 7a and has a steady state MGPC of 299 ng/cm2 (on a supercycle basis). This MGPC for the 1:1 Py:PDA cycle ratio is 20% higher than the MGPC for pure pPDA oMLD, indicating that the Py monomers introduce additional mass onto the growth surface. If Py and PDA monomers reacted equivalently when blended as when grown individually, we would expect the MGPC for the 1:1 cycle ratio to equal the sum of the MGPCs for each of the growth chemistries separately, or 313 ng/cm2/cycle. The value we observe for the 1:1 cycle ratio is 5% lower than this, suggesting that these monomers do not react as readily when alternating monomers as when using one monomer. Overall, we identify from Figure 7a that forming intimately mixed monomer blends by oMLD is viable through alternating monomer doses. In addition to the in-situ QCM study of Py/PDA copolymer formation in Figure 7a, we also deposited Py, PDA, and 1:1 cycle ratio Py:PDA copolymer films on Si wafers and measured their thicknesses ex-situ to confirm growth. In Figure 7b-d we plot the thickness vs. sample position down the length of the reactor for Py/MoCl5 oMLD (Figure 7b), PDA/MoCl5 oMLD (Figure 7c) and a Py:PDA copolymer formed in a 1:1 cycle ratio (Figure 7d), all at 150°C. Based on the data in Figure 7b-d, the average growth rates at 150 °C were 0.09 nm/cycle, 1.35 nm/cycle, and 1.39 nm/cycle, respectively for pPy, pPDA,

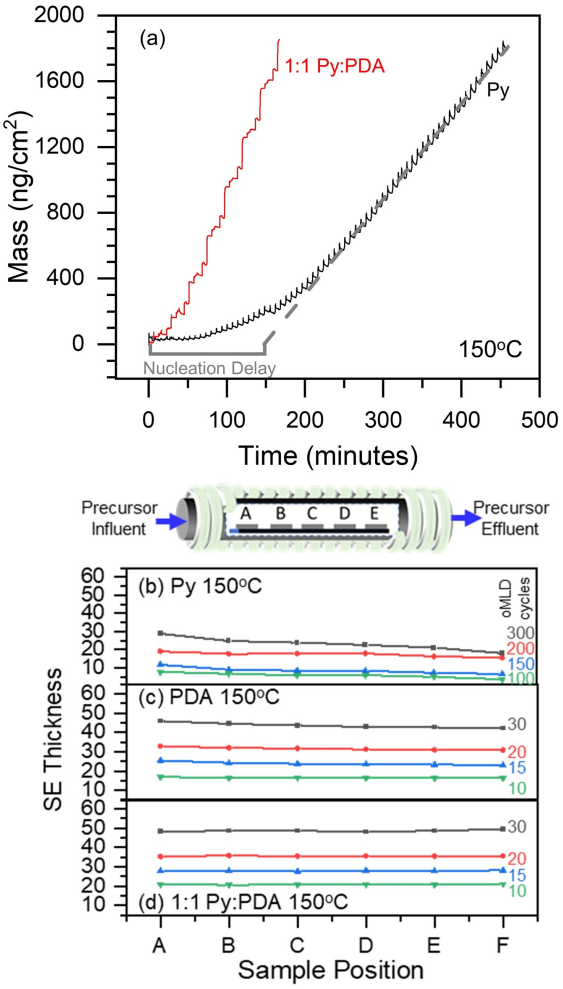

Figure 3.8: Growth enhancement by mixing Py and PDA monomers during oMLD growth cycles including, (a) QCM growth of initial oMLD pPy and enhanced deposition alternating between Py and PDA monomers, as well as ex-situ SE thickness measurements on Si vs. position down reactor body for (b) pPy film samples deposited at 150o C, (c) pPDA film samples deposited at 150o C, (d) copolymer films formed by alternating cycles of Py/MoCl5 and PDA/MoCl5 oMLD, deposited at 150o C.

and 1:1 Py/PDA copolymer. These growth rates were confirmed by NR measurements (not shown), indicating growth rates of 0.09 nm/cycle, 1.39 nm/cycle, and 1.43 nm/cycle, respectively for pPy, pPDA, and 1:1 Py/PDA copolymer. The N-N distance within each PDA monomer is 5.657 Å, so the growth rate of 1.35 nm/cycle for PDA/MoCl5 oMLD indicates that 2.4 monolayers of PDA are formed per oMLD cycle. We attribute the more rapid nucleation and growth and improved uniformity of PDA and Py:PDA copolymer films to excess amine groups introduced onto the growth surface by the PDA monomer. We expect that PDA produces an effect that is analogous to previous reports of metal-organic MLD reactions where the use of a reactant with an excess of functional groups (e.g. glycerol) provides enhanced growth over a reactant with fewer functional groups (e.g. ethylene glycol).[89,90] Interestingly, in addition to the more rapid nucleation and growth provided by PDA monomers, we also observe improved film uniformity when blending Py and PDA monomers in oMLD films. In Figure 7b-d we depict the film thickness at different numbers of oMLD growth cycles for samples positioned at 8 cm spacing down the length of the 50 cm reactor tube. Here, sample A is positioned closest to the precursor influent, and sample F is positioned closest to the precursor effluent out of the reactor tube. For the Py/MoCl5 oMLD chemistry in Figure 7b, we observe variation in film thickness as a function of sample position for all numbers of oMLD growth cycles. 300 oMLD cycles of Py/MoCl5 yields a maximum film thickness of 38 nm at the entrance of the reactor, with a monotonic decrease in thickness in the direction of flow, yielding a 24 nm film thickness at the exit of the reactor. This corresponds to a 37% drop in thickness over the reactor length. 30 oMLD cycles of the PDA/MoCl5 chemistry produces a more uniform deposition of 42.2±1.4 nm total thickness, with only a 2% loss in thickness over the reactor length. The 1:1 Py:PDA cycle ratio copolymer exhibits no gradient in thickness for all numbers of oMLD cycles. 30 1:1 Py:PDA oMLD supercycles yielded films with 48.59 ± 0.47 nm thickness, and no sample deviated from the average thickness by more than 0.81 nm. After establishing that oMLD growth readily proceeds when blending monomer cycles to form copolymer films, we employed CV measurements to identify how blending these monomers impacted the redox features for azo, phenazine, and Py moieities. In Figure 8a, we depict aqueous CV experiments of oMLD films grown using 1:1, 5:1, and 20:1 cycle ratios of Py:PDA oMLD cycles. If the monomers were to form discrete pPDA and pPy domains, we would expect that the redox activity for the oMLD copolymers would appear as a superposition of pPy and pPDA electrochemical responses. Instead, we observe a response where the qualitative shape of the CV changes depending on the Py:PDA cycle ratio in Figure 8a. This indicates that by alternating doses of the Py and PDA monomers during oMLD growth in different ratios, we intimately mix these monomers to form qualitatively different local molecular structures

with different electrochemical properties. For the 1:1 Py:PDA cycle ratio, we observe a CV in Figure 8a that is similar to PDA-only oMLD films, but with enhanced redox-activity on the oxidizing sweep at +0.5 V and on the reducing sweep at -0.7 V vs. Ag/AgCl relative to PDA-only oMLD. Although the redox potential of each monomer may be expected to shift based on blending of molecular orbitals from these mixed monomers, it appears that at this 1:1 cycle ratio, the redox potentials of pPDA are unshifted, and the electrochemical activity from pPy is only observed after fully oxidizing or reducing the pPDA component of the film. We note that this hysteresis effect for charge transfer observed for the 1:1 cycle ratio of Py:PDA in Figure 8a is of interest for neuromorphic computing elements,[91,92] and other electronics applications (e.g. diodes).[93] We attribute the origins of this hysteresis effect to branching effects from mixing monomers into a copolymer. We note that for this 1:1 cycle ratio, the fraction of pPy in the film is expected to be small – the growth rate of pPy oMLD at 150°C is only 0.09 nm/cycle, corresponding to 0.23 monolayers of pPy, whereas the growth rate of pPDA oMLD at 150°C is 1.35 nm/cycle, corresponding to 2.4 monolayers of pPDA. Based on the relative growth rates for the two monomers, we expect that the polymer films for the 1:1 cycle ratio contain 90% PDA monomers and 10% Py monomers. At this low molar ratio of Py, we expect that Py monomers react on PDA in the most favorable ortho position as depicted in Figure 8b such that electrons initially flow in/out of the connected pPDA network, and only transfer to branching Py monomers after oxidizing/reducing the PDA molecular constituents, giving rise to the irreversible electrochemical behavior observed for the 1:1 Py:PDA cycle ratio in Figure 8a.

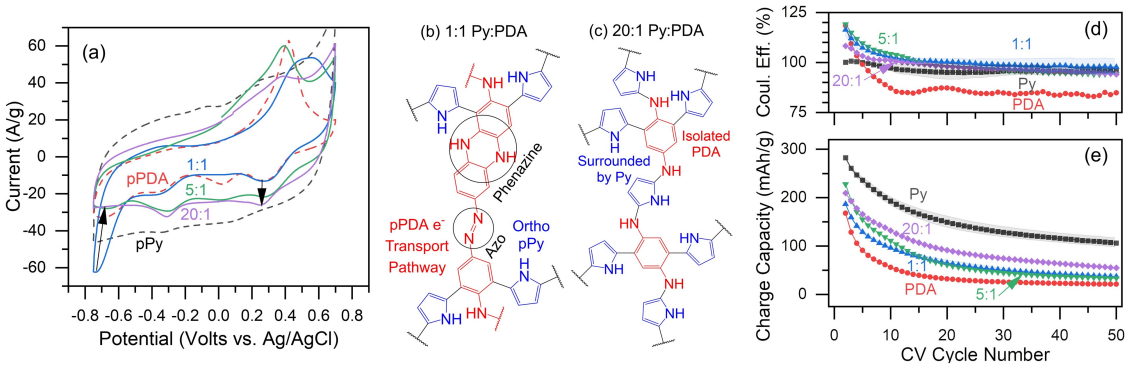

Figure 3.9: Comparison of (a) cyclic voltammograms of pPy (20.4 nm thickness), pPDA (40.3 nm thickness), 1:1 pPy:pPDA copolymer (48.5 nm thickness), 5:1 pPy:pPDA copolymer (49.7 nm thickness) and 20:1 pPy:pPDA copolymer (29.5 nm thickness) at a sweep rate of 50 mV/s in aqueous electrolyte tuned to a pH of 3.5. A low Py content for the 1:1 cycle ratio drives irreversible charge storage, which we attribute to Py branching from pPDA domains as depicted in (b), whereas a high Py content leads to more reversible charge storage for the Py constituent which we attribute to isolated PDA monomers surrounded by PDA as depicted in (c). This interpretation is corroborated by the (d) coulombic efficiency and (e) specific capacity during extended cycling. The shaded areas around each data set in (d) and (e) represent the standard deviation from replicate measurements.

To confirm this interpretation, we increased the cycle ratio of Py:PDA from 1:1 to 5:1 and 20:1. The film thicknesses for the data reported in Figure 8 were 20.4, 40.3, 48.5, 49.7, and 29.5 nm for Py, PDA, and 1:1, 5:1, 20:1 Py/PDA copolymer films, after 150, 30, 30, 150, and 210 total oMLD cycles (sum of Py/MoCl5 and PDA/MoCl5 cycles), respectively. Based on the growth rates of the independent Py/MoCl5 and PDA/MoCl5 oMLD chemistries, the 5:1 and 20:1 cycle ratios correspond to 1:2 and 2:1 molar ratios of Py:PDA monomers, respectively, within the mixed monomer film. In Figure 8a, we see that as the number of Py oMLD cycles increases, the redox process arising from the pPy constituent of the film (E0 = -0.2 V vs. Ag/AgCl) becomes more reversible. On the oxidizing sweep, the additional charge storage capacity provided from introducing Py into pPDA shifts from a redox potential of >0.4 V at a 1:1 cycle ratio (higher potential than the oxidation peak for pPDA) to a potential of <0.3 V at a 20:1 cycle ratio (lower potential than the oxidation peak for pPDA). Likewise, on the reducing sweep, as the amount of Py within the film increases, the amount of cathodic current at a potential of -0.7 V decreases, and the amount of anodic current between +0.3 and -0.5 increases – as highlighted with arrows in Figure 8a. Under the 20:1 cycle ratio condition, we expect that Py monomers are more intimately blended and surround PDA monomers within the copolymer film, as depicted in Figure 8c. The 5:1 and 20:1 cycle ratios (with 1:2 and 2:1 molar ratios of each monomer) exhibit qualitatively different redox features from either the PDA-only or Py-only polymers, indicating that intimately blending the monomers causes different reactions and/or molecular orbital mixing for adjacent monomers, impacting the equilibrium redox potentials we observe. By adjusting the cycle ratio of the two monomers, we achieve different molecular structure and monomer interaction effects, yielding different redox properties for each blend. The interpretation of differences in molecular branching character depending on the Py content in the Py:PDA copolymers depicted in Figure 8b and 8c is corroborated by the coulombic efficiency and stability of the films in Figure 8d and 8e. Phenazine moieties are susceptible to oxidative decomposition and disproportionation in the presence of hydroxyls,[77] leading to a low coulombic efficiency in Figure 8d and rapid decay in electrochemical capacity vs. cycle number in Figure 8e for pure PDA/MoCl5 oMLD films. By introducing just 10 mol% Py into the pPDA film using a 1:1 Py:PDA cycle ratio, the coulombic efficiency increases from 80% to >95% and the electrochemical cycling stability improves relative to pure pPDA. We attribute this to branching Py monomers that interconnect pPDA domains and prevent oxidative decomposition. This improvement in coulombic efficiency is observed for the 5:1 and 20:1 cycle ratios as well. The 5:1 and 20:1 cycle ratios would be expected to result in the highest electrochemical capacity in aqueous electrolyte by disrupting azo formation, but we expect that the hydrophilic nature of the resulting branched

structure depicted schematically in Figure 8c may facilitate dissolution in the aqueous electrolyte employed in Figure 8, giving rise to the lower capacity and more rapid capacity loss for these cycle ratios in Figure 8e. We note that the capacity loss we observe for all of the compositions in Figure 8e is common for redox-active polymers and is typically attributed to densification and/or chemical decomposition.[94,95] The capacity loss may be addressed in future work by adjusting the potential window,[27,96,97] introducing monomer substituents,[98] and/or modifying the polymer surface.[95]

To further confirm our understanding of how altering the Py:PDA cycle ratio impacts the molecular structure within the polymer films, we performed nonaqueous CV measurements on pure PDA/MoCl5 oMLD films (0:1 Py:PDA cycle ratio) and the 1:1 and 5:1 cycle ratio copolymers as depicted in Figure 9. In these measurements, we observe that as we increase the number of Py cycles, we observe a decrease in the redox activity in the potential window for azo formation (i.e. more reducing potentials of 1.7 to 0.9 V vs. Na/Na+ in Figure 9). We find that the specific capacity on the cathodic sweep from 1.7 to 0.9 V vs. Na/Na+ arising from azo functionality is 204 mAh/g, 116 mAh/g, and 113 mAh/g for the 0:1, 1:1, and 5:1 Py:PDA cycle ratios, respectively, This indicates that increasing the amount of Py oMLD cycles disrupts formation of azo groups within the blended polymer films as we depict in Figure 8c. Likewise, as the number of Py cycles increases from a 0:1 to 5:1 Py:PDA ratio, we observe an increase in the redox activity at more oxidizing potentials of 1.5 to 3.3 V vs. Na/Na+, which corresponds to the potential window for phenazine and pyrrole functionality. whereas the specific capacity on the anodic sweep arising from pPy/phenazine character is 115 mAh/g, 86 mAh/g, and 182 mAh/g for the 0:1, 1:1, and 5:1 cycle ratios, respectively. We note that this potential window of 1.5-3.3 V vs. Na/Na+ was selected for this analysis to not include the solvent decomposition peak observed at more oxidizing potentials for the 5:1 Py:PDA cycle ratio. We also note that the 20:1 cycle ratio sample was not included in this analysis because irreversible peaks under both oxidizing (-1.3 V vs. Na/Na+) and reducing (0.5 V vs. Na/Na+) potentials consistent with solvent decomposition

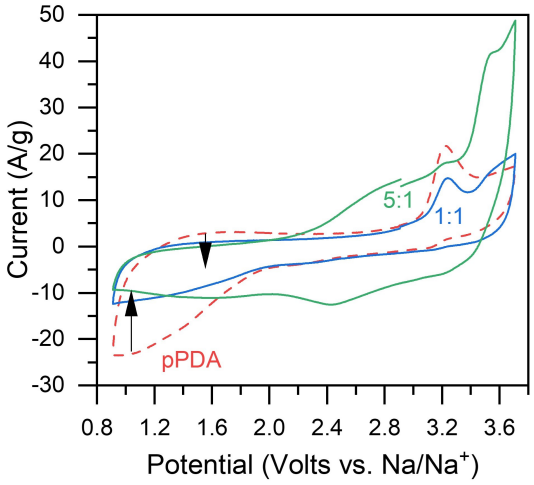

Figure 3.10: Nonaqueous cyclic voltammetry at a sweep rate of 20 mV/s in 0.1 M NaClO4 in acetonitrile for 40.3 nm thick pPDA (dashed red), 48.5 nm thick 1:1 Py:PDA cycle ratio (blue) and 49.7 nm thick 5:1 Py:PDA cycle ratio (green) films grown by oMLD on PGS substrates.

dominate the electrochemical behavior for this cycle ratio. The origins of the irreversible processes in nonaqueous electrolyte for the Py-rich films may arise from catalytic decomposition of the electrolyte or from dissolution/decomposition of the polymer films, but this is unclear with the present data. Overall, these nonaqueous electrochemical results support the control over the molecular composition of the oMLD films using different oMLD cycle ratios outlined in Figure 8b and 8c.

3.5 Conclusion

In this work, we report the first demonstration of oMLD of conjugated amine polymers. We find that oMLD of amine-containing monomers proceeds via irreversible chemisorption of each precursor to produce redox-active films with molecular-scale thickness control. This oMLD approach allows for the formation of conformal and uniform films of pPy on 3D substrates, as demonstrated by uniform coating into porous channels to an aspect ratio of 200:1. The ability to form conjugated amine polymers by oMLD provides a route to deliver thin films of redox-active polymers onto 3D electrode surfaces. We also identify that thin-film oMLD pPy exhibits capacities up to 282 mAh/g – 68% of pPy's theoretical capacity, and maintains 50% of the theoretical capacity of pPy, even when charging in under 3 s. These specific capacities are up to 2× higher than values of 140 mAh/g observed for pPy synthesized by other methods,[6] which we attribute to the ultrathin (<10 nm) films obtained using oMLD. Previous work has reported similar gains for thin-film inorganic redox-active layers formed by ALD, where the reduction in length-scale for solid-state diffusion yields high rate charge storage for energy storage and desalination applications.[60–63] However, the barrier preventing the adoption of ALD coatings has been the high-cost organometallic precursors needed to form inorganic active layers by ALD. Here, we demonstrate the formation of of redox-active polymer layers with high electrochemical capacities[64,65], using low-cost organic precursors. This provides a more economically viable route for the use of an ALD-like process (here, oMLD) to deliver high-performance materials in a thin-film geometry for redox-active electrodes. In particular, the high capacity of pPy films in aqueous electrolytes makes them of interest as electrode materials for aqueous batteries, as supercapacitor electrodes, and/or as ion-uptake uptake in electrochemical desalination.[12,99,100] We also identify that while oMLD of Py/MoCl5 produces pPy films, oMLD of Ani/MoCl5 and PDA/MoCl5 chemistries produce azo moieties. We attribute this behavior to the coordination of the MoCl5 oxidant to nucleophilic amine groups on the growth surface, driving reactions adjacent to the amine, and leading to the formation of azo groups for primary amines. This result opens avenues to harness this mechanism to direct surface polymerization and control the

molecular structure of conjugated polymer films using oMLD. The azo-containing films produced by PDA/MoCl5 oMLD exhibit redox activity at -1.7 V vs. Ag/AgNO3 (+1.5 V vs. Na/Na+) in nonaqueous electrolyte. This reversible redox activity at highly anodic (negative) potentials through electrochemical reduction of azo groups makes these PDA/MoCl5 oMLD films of interest as anode materials for alkali ion batteries.[82] Finally, we report the molecular mixing of Py and PDA monomers by alternating between oMLD cycles of Py/MoCl5 and PDA/MoCl5 chemistries during oMLD growth. These molecularly-mixed Py/PDA oMLD films exhibit qualitatively different electrochemical behavior from the films formed using the isolated constituent monomers. We demonstrate control over molecular constituents within the film by alternating the ratio of oMLD cycles of each monomer, yielding different electrochemical responses. The intimate molecular mixing of monomers we demonstrate here using sequential surface reactions via oMLD provides a route to achieve pristine control over the molecular structure of conjugated polymers, and will allow us to examine how molecular structure impacts electrical and electrochemical properties in future work. This is of particular interest considering recent work establishing understanding of the semi-localized charge transport in conducting polymers,[101] where control over monomer ordering in polymer chains will allow us to examine the molecular origins of charge transport physics in conjugated polymers.

Chapter 4

MECHANISTIC INSIGHTS INTO OXIDATIVE MOLECULAR LAYER DEPOSITION OF CONJUGATED POLYMERS

4.1 Abstract

Oxidative molecular layer deposition (oMLD) promises to enable molecular-level control of polymer structure through monomer-by-monomer growth via sequential, self-limiting, gas-phase surface reactions of monomer(s) and oxidant(s). However, only a few oMLD growth chemistries have been demonstrated to date and limited mechanistic understanding is impairing progress in this field. Here, we establish key insights into the surface reaction mechanisms underlying oMLD growth. We identify the importance of a two-electron chemical oxidant with sufficient oxidation strength to oxidize both a surface and a gas-phase monomer to enable oMLD growth. The mechanistic insights we report will support rational molecular assembly of copolymer structures to starkly improve the electrochemical capacity. This work is foundational to unlock molecular-level control of redox-active polymer structure and will enable the study of previously intractable questions regarding the molecular origins of polymer properties, allowing us to control and optimize polymer properties for energy storage, water desalination, and sensors.

4.2 Introduction

Oxidative molecular layer deposition (oMLD) is a relatively new deposition technique used to form electrically (semi)conductive and redox-active conjugated polymers. oMLD is of growing interest because it provides molecular-level control of conjugated polymer film thickness, yielding

uniform thin film polymers that are useful for electrochemical energy conversion and storage[46, 207, 39], sensors[221, 222] and textiles[223, 224, 46, 225]. The oMLD technique is a sub-category of molecular layer deposition (MLD), in which complementary bifunctional organic molecules are dosed in alternating exposures to form polymer films[226, 178] and is akin to common atomic layer deposition (ALD) processes used to form inorganic films[175]. The oMLD process uses the same monomers and oxidants that are used in conventional solution phase polymerization, but doses these species in the gas phase in sequential chemical exposures. oMLD is distinct from vapor-phase polymerization (VPP) studies in which an oxidant and monomer are co-dosed in the gas phase to produce polymer films[227, 228, 50, 227, 229, 230], because it separates the gas phase chemical precursors into sequential exposure steps. To date, oMLD processes have been demonstrated using ethylenedioxythiophene (EDOT)[46, 231, 232], pyrrole (Py)[207], paraphenylenediamine (PDA)[207], and 3-hexylthiophene (3HT)[222] monomers and MoCl5[46], ReCl5[232], and SbCl5[231] chemical oxidants. These species undergo self-limiting surface reactions to grow thin-film polymers monomer-by-monomer. Because oMLD proceeds via surface reactions from vapor phase precursors, it does not require the use of side-chains or copolymer additives necessary for solution-based polymer processing. This allows for the formation of chemically pure polymers and enables a fundamental shift in polymer material development (and scientific inquiry), in which polymer properties are dictated by local structure, rather than microstructure or defects. As an example of this, pEDOT coatings formed by oMLD routinely achieve high electrical conductivities of >2000 S/cm8[232, 231], and in some reports have achieved conductivities of $>$ 6000 S/cm.[231] In recent work, our group has also expanded beyond oMLD of pEDOT and demonstrated the deposition of pPy by oMLD, achieving record electrochemical capacities of up to 282 mAh/g.[207] This specific capacity is 2 times higher than the highest capacities of 140 mAh/g measured for pPy[233, 234] and is on-par with the electrochemical capacities of next-generation alkali-ion battery materials[235, 151]. The high electrochemical capacity of oMLD pPy (and high electronic conductivity of oMLD pEDOT described above) are attributed to the chemical purity and molecular structure control provided by oMLD growth. In early studies, the oMLD mechanism has been described as equivalent to homogeneous oxidative polymerization reactions, but spatially constrained to a substrate surface[46, 232, 231]. However, recent work has demonstrated that this picture is incomplete. Some combinations of monomers and oxidants that successfully polymerize in homogenous mixtures do not yield polymers in sequential oMLD doses. For example, EDOT and Br^2 yield pEDOT when mixed homogeneously in vapor or liquid[236, 237], but do not yield pEDOT films when dosed in sequential pulses[232]. Additionally, some reactions do not yield the same products as observed from homogeneous mixtures. For example, primary amines

in Ani react to form azo species (e.g. azobenzene) during sequential oMLD doses[207] instead of forming pAni observed by homogeneous oxidation. Here, we (1) establish key insights into the oMLD growth mechanism that help to explain these unexpected phenomena, (2) identify design rules to guide future development of new oMLD chemistries and processes, and (3) use this understanding to control the molecular assembly of copolymers with record electrochemical capacity.

4.3 Materials And Methods

4.3.1 Oxidative Molecular layer Deposition

Deposition of polymer thin-films by oMLD was carried following previously established conditions[238]. Briefly, the oMLD reactor chamber was held at 150°C using PID temperature controllers. The reactor chamber operated under a continuous stream of 250 SCCM of ultra-high purity argon carrier gas at reduced pressure (0.85 Torr). Thiophene (Thi, 98%, Fischer Scientific) and, Furan (Fu, 99%, Fischer Scientific) were held at room temp, while ethylenedioxythiophene (EDOT, 98%, 1PlusChem), paraphenylenediamine (PDA, >97%, Fischer Scientific), and molybdenum pentachloride (MoCl5, 99.6%, Fischer Scientific) were held at 100 °C, each in a jacketed flow-over precursor bubbler held at a fixed temperature with PID temperature control. A peak dose pressure of at least 100 mTorr above base pressure was observed for each monomer precursor dose under these conditions. The reactor chamber, QCM holder, and sample tray were passivated with the target oMLD chemistry before performing each experiment. Films for ex-situ analysis were deposited on Si wafers (Silicon Valley Microelectronics) and pyrolytic graphite sheets (PGS, Newark). The samples were preheated prior to depositions under inert argon flow for at least 30 min. A typical growth sequence consisted of an A/B dose sequence where the monomer chemical precursor (A) was dosed for 10 s followed by 100 s of carrier gas purge time, then the MoCl5 chemical oxidant (B) was dosed for 150 s followed by 100 s of carrier gas purge time, unless otherwise noted. These A/B cycles were repeated to increase the thickness of the resulting polymer films.

4.3.2 Electrochemical Characterization, Cyclic Voltammetry (CV)

Polymers deposited onto PGS substrates were characterized by CV with a Biologic SP-150 potentiostat using a 3 electrode custom glass electrochemical cell, as described previously.1,2 Aqueous electrochemical measurements were performed in 0.1 M NaCl aqueous electrolyte degassed using argon purge at circumneutral pH using an Ag/AgCl reference electrode (BASi) and graphite rod

counter electrode (99.999%, Fischer Scientific). CV experiments were performed at a sweep rate of 50 mV/s over a potential range of 1.00 to +1.00 V vs Ag/AgCl, unless otherwise noted.

4.3.3 Raman Spectroscopy

Raman Spectra acquisition was conducted utilizing a Renishaw inVia Raman spectrometer with 633 nm excitation laser. Data was collected over 500–2000 cm–1 with sweeping scan of 10 cm–1/s and a laser power of 10.1 mW.

4.3.4 X-ray photoelectron spectroscopy (XPS)

oMLD deposited polymer films (Py, Py/Fu, Py/Thi) were analyzed via XPS using a Thermo Scientific Nexsa instrument with a monochromatic Al K X-ray source. These XPS measurements were used to measure incorporation of Fu and Thi into pPy during alternating oMLD exposures. High-resolution scans (200 s acquisition time, 500 ms dwell time, 40 eV pass energy, and 100 meV step size) of O 1s, N 1s and S 2p regions were performed to observe S (Thi) or O (Fu) incorporation into pPy. The peak locations used in this work were charge-corrected to the C 1s peak, centered at an energy of 284.6 eV. The final XPS spectra was analyzed using CasaXPS and plotted using Origin Lab Software.

4.3.5 B: Measurements of Monomer Oxidation Onset Potentials

To measure the onset potential for monomer oxidation, nonaqueous linear sweep voltammetry electrochemical measurements were performed in acetonitrile with 0.1 M (Py, PDA, EDOT, Thi, Fu) and 1.0 mM NaNO3 supporting electrolyte salt using a graphite counter electrode and Ag/AgNO3 reference electrode. Each monomer was measured sweeping at 17 mV/min starting at -0.5 V vs. Ag/AgNO3. The results from this linear sweep voltammetry are presented in Figure S1.

Figure S1. Linear sweep voltammetry results for the measurement of the onset potential for oxidation of Py, PDA, EDOT, Thi, and Fu. (0.1 M Monomer (acetonitrile), sweep Rate 17 mV/s.

The onset potential was calculated as the extrapolation from a linear fit of current vs voltage to the intersection with the X-axis after the onset of oxidation. These results are reported in the second column of Table S1. The Ag/AgNO3 reference electrode was calibrated using sublimated ferrocene and found to have a potential of 0.51 V vs standard hydrogen electrode (SHE), in agreement with previous reports for a 0.01 M Ag/AgNO3 reference electrode in acetonitrile.3 Using this calibrated potential shift of Ag/AgNO3 vs SHE, we report the onset potentials vs SHE for each monomer in the third column of Table S1. These values are in close agreement with previously reported literature

values as summarized in the fourth column of Table S1, with the corresponding references in the fifth column of Table S1.

Table S1. Oxidation onset potentials as measured by linear sweep voltammetry and compared against literature values.

4.3.6 C: Density Functional Theory (DFT) Calculations

To be a successful in an oMLD reaction, an oxidant must have sufficient oxidation strength to oxidize the target monomer(s). For the MoCl5 oxidant used in this work, the Mo(V)Cl5/Mo(IV)Cl4 and Mo(IV)Cl4/Mo(III)Cl3 redox couples are relevant to the oMLD reactions. However, to our knowledge, the standard oxidation potential for the Mo(V)Cl5/Mo(IV)Cl4 redox couple has not been reported in the literature, and the only value known to the authors for the oxidation potential of the Mo(IV)Cl4/Mo(III)Cl3 redox couple was measured in molten salt electrolytes at elevated temperature.10 Here, we calculate the standard oxidation for both redox couples using DFT.

The standard potential of a redox reaction can be determined by Nernst equation

$$E^{\circ} = \frac{\Delta G^{\circ}_{(R/O)}}{n_e F} - E_{ABS} \tag{4.1}$$

where $\Delta G^{\circ}_{(R/O)}$ is the free energy changes of a redox reaction at standard conditions, n_e is the number of electrons transferred, F is the faraday constant, and E_{ABS} is the absolute potential of the reference electrode.

To calculate the equilibrium reduction potential for the Mo(V)Cl5/Mo(IV)Cl4 and Mo(IV)Cl4/Mo(III)Cl3 redox couples (indicated in general as MoCln + e- MoCln-1 + Cl-) we coupled each of these reactions with the Cl- oxidation reaction 2Cl- Cl2 + 2e- (E0 = 1.3589 V vs. SHE) and calculated the energy change for the overall reaction 2MoCln + 2Cl 2MoCln-1 + Cl2. The change in Gibbs free energy, $G^{\circ}{}_{(}R/O), for this overall reaction is calculated as$

$$\Delta G^{\circ}_{(R/O)} = G_{products} - G_{reactants} \tag{4.2}$$

$$G = H - TS \tag{4.3}$$

$$H = U + k_b T \tag{4.4}$$

$$U = E_{el} + E_{ZPE} + E_{vib} + E_{rot} + E_{trans)} \tag{4.5}$$

where G is the absolute Gibbs free energy, H is the absolute enthalpy, and U is the absolute internal

energy. E(el) is the electronic energy . E(ZPE) is the zero-point vibrational energy. E(vib) is the finite temperature correction to E(ZPE) due to population of excited vibrational states. E(rot) and E(trans) are the rotational and translational thermal energy, respectively. To calculate the necessary quantities in Eq. 1-5, DFT calculations were performed for the molybdenum species . These calculations were performed following the guidelines in a benchmark study of DFT reduction and oxidation potentials by Neugebauer et al.11 A geometry optimization was performed to find the minimum-energy geometry for each species, followed by a final single-point energy and Hessian calculation. The lowest energy spin states for the MoCl5, MoCl4, and MoCl3 species were found to be doublet, triplet, and quartet, respectively. All DFT calculations used the ORCA 4.2.1 program,.12,13 All calculations used the B97x-D3 exchange-correlation functional,14 and the ma-def2-qzvpp basis set,.15,16 The calculations used effective core potential core potentials for molybdenum as implemented in ORCA,.17,18 and The DFT calculations use an atom-pairwise dispersion correction with zero damping scheme.19 All The calculations all used the tightscf, grid5, and finalgrid6 keywords in ORCA. $\Delta G^{\circ}_{(R/O)}$ values for the overall reaction 2MoCln + 2Cl 2MoCln-1 + Cl2 with the Mo(V)Cl5/Mo(IV)Cl4 and Mo(IV)Cl4/Mo(III)Cl3 redox couples were calculated to be 3.96 eV and 0.206 eV, respectively. Taking ne = 2 for the overall reaction and shifting from the Cl-/Cl2 reference to SHE, these $\Delta G^{\circ}_{(R/O)}$ values correspond to 3.34 V vs. SHE for the Mo(V)Cl5/Mo(IV)Cl4 couple and 1.46 V vs. SHE for the Mo(IV)Cl4/Mo(III)Cl3. As mentioned above, to the authors' knowledge, no standard oxidation potential values for the Mo(V)Cl5/Mo(IV)Cl4 have been reported in the literature, and the only oxidation potential for the Mo(IV)Cl4/Mo(III)Cl3 redox couple is reported to be 0.67 V vs SHE in molten salt electrolyte at 900 K. Assuming a temperature coefficient of -1 mV/K for this oxidation reaction based on other temperature coefficients for MoOx oxidation reactions in water,20 this potential of 0.67 V vs SHE at 900 K corresponds to an oxidation potential of 1.27 V vs. SHE, in close agreement with the value of 1.46 V vs SHE calculated here by DFT. We note that a difference of 200 mV in the oxidation potentials for the Mo(V)Cl5/Mo(IV)Cl4 and Mo(IV)Cl4/Mo(III)Cl3 redox couples does not impact the interpretation of the relative oxidation potentials depicted in Figure 4 of the main text.

4.4 Results And Discussion

To highlight the shortfall of current oMLD mechanistic understanding, we compare in situ quartz crystal microbalance (QCM) data acquired during oMLD growth using EDOT vs thiophene (Thi) monomers in Figure 1a. Here, each monomer is dosed in alternating exposures with the MoCl5

oxidant at 150 oC under 0.85 Torr (250 sccm) of continuous argon purge in a A:purge:B:purge timing sequence of 10 s: 150 s: 130 s: 150 s. For further information on the Materials and Methods for this growth, please refer to the Supporting Information (SI) Section A. As reported in previous studies, oMLD growth readily proceeds using the EDOT monomer, here exhibiting a mass gain per cycle (MGPC) of 300 ng/cm2/cycle. But, surprisingly, we do not observe oMLD growth using the Thi monomer (MGPC $<$ 2 ng/cm2/cycle). As shown in the inset of Figure 1a, the Thi monomer represents the core functional structure of EDOT, but without the ethylene-dioxyl substituent. Considering the successful oMLD growth of EDOT:MoCl5, as well as recent reports of successful oMLD of Py:MoCl5¬ and 3HT:MoCl5,[222] one would expect that the Thi monomer would undergo oMLD growth, but it does not. This highlights a gap in mechanistic understanding of the oMLD growth mechanism.

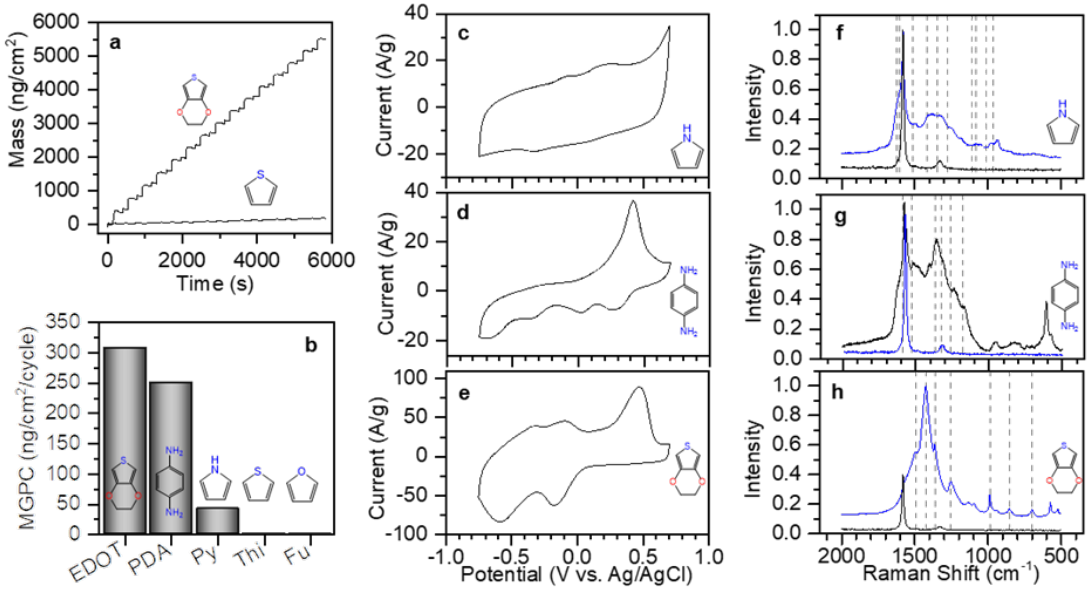

Figure 4.1: oMLD using EDOT, PDA, Py produced the expected polymers, but surprisingly did not produce polymer films using Thi or Fu monomers. (a) A comparison of EDOT and Thi growth under the same conditions (Dose:Purge, 10s:100s). (b) oMLD steady-state mass gain per cycle (MGPC) of each monomer used with MoCl5 oxidant. (c-e) Cyclic voltammetry (CV) of (c) Pyrrole, (d) PDA, (e) EDOT. (f-h) Raman spectroscopy with literature reference lines for (f) pPy29, (g) pPDA 30, (h) pEDOT31

In Figure 1b we report the MGPC measured under these same growth conditions for three monomers that have been previously demonstrated by oMLD: EDOT (300 ng/cm2), PDA (250 ng/cm2/cycle), and Py (45 ng/cm2/cycle). We also report the MGPC values measured for furan (Fu), and Thi monomers in Figure 1b. Fu and Thi do not produce appreciable film growth in QCM experiments. To confirm these results, we also performed depositions on flat samples for ex situ

characterization. Spectroscopic ellipsometry (SE) on films deposited on Si witness wafers (not shown) confirmed the growth behavior in Figure 1b, where EDOT, PDA, and Py exhibited growth rates of 0.5, 0.98, and 0.3 nm/cycle, respectively, after 100 oMLD cycles, but Fu and Thi produced no detectable films. Raman spectroscopy of the EDOT/MoCl5 and Py/MoCl5 oMLD films exhibited characteristic spectra for polypyrrole (pPy), polyparaphenyelenediamine (pPDA)and polyethylenedioxythiophene (pEDOT), respectively (Figure 1c-d), and no Raman response was observed above the background when using Fu and Thi monomers. Likewise, cyclic voltammetry (CV) electrochemical measurements in 0.1 M NaCl electrolyte yielded characteristic electrochemical response consistent with pPy and pEDOT (Figure 1e-g). As reported in recent work, PDA/MoCl5 produces a blend of phenazine and azo functionality with corresponding mixed redox activity[207]. We observed no electrochemical response above the bare substrate signal for Fu and Thi monomers (not shown). Considering the molecular structures of the five monomers studied in Figure 1, there is not a clear pattern as to why Thi and Fu do not exhibit oMLD growth To understand the failure of oMLD growth using the Fu and Thi monomers, we more carefully examined the QCM data collected during oMLD growth of pEDOT as presented in Figure 2. By examining mass changes during precursor exposures, the mechanistic details of surface reactions can be elucidated[239, 240, 177]. The EDOT monomer was used for these mechanistic studies because polymerization is constrained to the C positions due to the ethylene dioxyl ligand, simplifying interpretation. The goal of these QCM studies was to determine the specific monomer and oxidant surface reaction processes and extend this understanding of EDOT reaction mechanisms to understand why Thi and Fu do not react to form polymer films. In Figure 2a we steadily increased the dose times and purge times over the course of the experiment until fully saturating behavior was observed for the EDOT/MoCl5 growth chemistry. Initial growth conditions reflected previously reported dose/purge times for EDOT (5s/60s) and MoCl5 (5s/60s), and we observed an MGPC of 20 ng/cm2 under these conditions. However, recent studies indicate that these dose and purge times may be insufficient for saturation[207, 241]. When increasing dose/purge times from condition (i) to condition (iii) in Figure 2a, we observe an increase in MGPC from 20 ng/cm2/cycle to 300 ng/cm2/cycle. Further increasing the dose and purge times from condition (iii) to condition (iv) in Figure 2a did not lead to an increase in MGPC, indicating sufficient dose and purge times at condition (iii). Using condition (iii) from Figure 2a, we then examined the steady-state mass changes during each precursor dose as depicted in Figure 2b (MoCl5) and Figure 2c (EDOT). We identified a mass gain from the MoCl5 dose (m1) of 278 $\pm$5.8 ng/cm2 and a mass gain from the EDOT dose (m2) of 71 $\pm$2.7 ng/cm2. Taking the ratio of m2/m1 to normalize against the number of growth sites yields a value R = 0.255. Using this ratio, R, we can then compare against hypothesized

mechanisms to establish a mechanistic picture for EDOT/MoCl5 oMLD surface reactions.

In Figure 3, we propose a reaction mechanism for pEDOT oMLD that is supported by the QCM data collected in Figure 2. In this reaction scheme, MoCl5 forms a surface adduct with EDOT during the MoCl5 dose (Figure 2a), and upon subsequent EDOT dose, gas-phase EDOT coordinates to this adduct and MoCl5 performs a two-electron oxidation via Mo(V)Cl5 + 2e- Mo(III)Cl3 + 2Cl-; oxidizing both the surface EDOT monomer and the gas-phase monomer and linking the gas-phase monomer to the surface EDOT (Figure 2b). The net reaction generates 2HCl and MoCl3, where the MoCl3 byproduct that remains in the pEDOT film. This reaction scheme corresponds to a theoretical mass gain ratio of R=0.254, which is consistent with the experimentally measured value of R=0.255 from Figure 2. We note that in previous reports, the EDOT/MoCl5 oMLD process is described to proceed via a surface-based polymerization reaction in which the MoCl5 oxidant reacts with surface EDOT monomers to produce EDOT+• + HCl + MoCl4. In this alternate scheme, one interprets that the HCl and MoCl4 are inert volatile by-products and the surface EDOT+• drives reaction with gas-phase EDOT on the next EDOT exposure. However, this reaction scheme produces a theoretical ratio of R = 2.954 which is not consistent with the value of R=0.255 measured in Figure 2. Furthermore, for surface polymerization to proceed, the gas-phase EDOT must undergo oxidation to form EDOT+•, and this previously reported mechanistic picture does not explain how this occurs. We also note that we examined various other potential reaction schemes and calculated the corresponding R values, and the mechanism we report in Figure 3 is the only mechanism we found that is consistent with our experimental results. For example, coordination of a Mo2Cl10 dimer to each surface EDOT yields a ratio of R=0.127, only

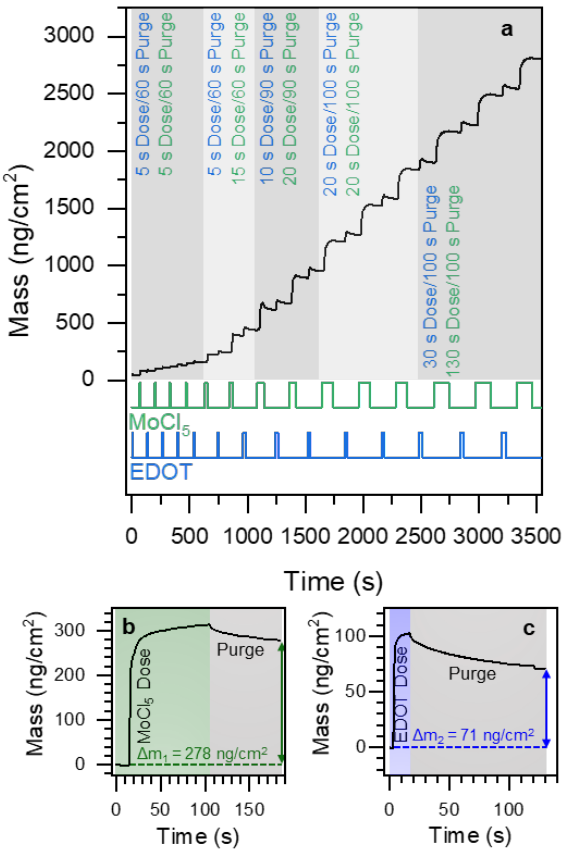

Figure 4.2: Experimental mass changes during steady-state and saturating oMLD growth of EDOT/MoCl5 provide mechanistic insights. (a) QCM of oMLD of EDOT/MoCl5 with increasing dose and purge time of oxidant and monomer until complete saturation is achieved. At steady state, we observe (b) single cycle mass gain for MoCl5 of 278 ng/cm2 and (c) single cycle mass gain for EDOT of 71 ng/cm2.

50% of the measured value. Furthermore, previous reports of a stoichiometric amount of Mo:S in the resulting pEDOT films8 are consistent with the mechanism we describe here.

The reaction scheme in Figure 3 reveals multiple key properties of monomers and oxidants that are necessary for a successful oMLD chemistry. For oMLD growth to proceed, an oxidant must be used which exhibits multiple oxidation states (i.e. Mo, Re, Sb used to date)8,21,22 and must undergo two reduction reactions, where both electron uptake processes occur at high enough oxidation potentials to oxidize both a surface monomer and a gas-phase monomer to link them together. In the case of the proposed oMLD EDOT reaction scheme, the oxidant (MoCl5), oxidizes two EDOT monomers, propagating polymerization by linking the surface EDOT (terminating a pEDOT chain) to the next gas-phase EDOT monomer. One can conceptually separate this into two one-electron oxidation steps for the MoCl5 oxidant: Mo(V)Cl5 + e- Mo(IV)Cl4 + Cl- and Mo(VI)Cl4 + e- Mo(III)Cl3 + Cl-. These two reactions must together have strong enough oxidation potentials to oxidize both the surface and gas-phase monomers. We propose that this two-electron oxidation process is the underlying reason for the failure of the oMLD process for the Fu and Thi monomers, where the oxidation power of Mo(IV)Cl4 is insufficient to oxidize Fu or Thi monomers. To explore this possibility, we examined the equilibrium redox potentials of the five monomers examined in Figure 1 as well as the equilibrium redox potential of Mo(V)Cl5/Mo(IV)Cl4 and Mo(IV)Cl4/Mo(III)Cl3. We employed nonaqueous linear sweep voltammetry measurements to measure monomer oxidation potentials as described in SI Section B. We measured onset monomer oxidation potentials of 0.87, 0.74, 1.21, 1.72, and 1.91 V vs. standard hydrogen electrode (SHE) for Py, PDA, EDOT, Thi, and Fu, respectively. We also performed density functional

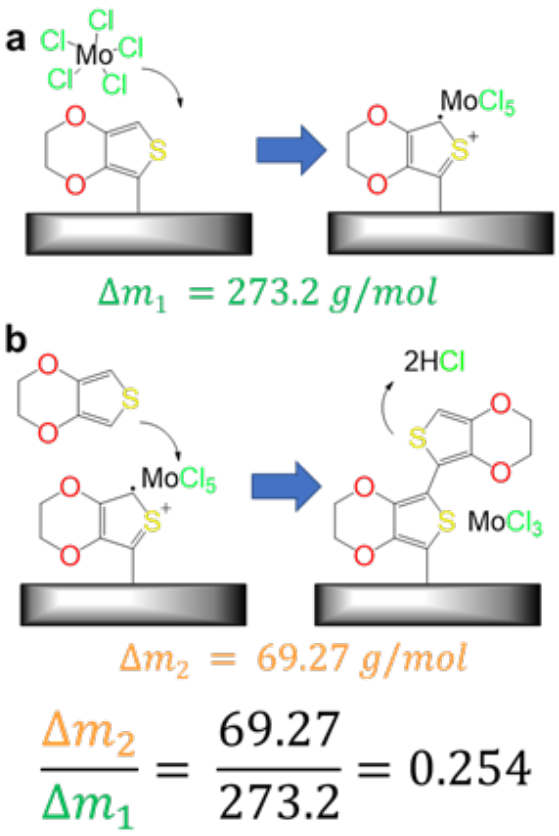

Figure 4.3: Proposed mechanism for oMLD surface reactions during sequential (a) MoCl5 and (b) EDOT exposures, where (a) MoCl5 complexes with a surface monomer (m1=273.2), then (b) during EDOT dose, a surface Mo (IV) species oxidizes both a surface and a gas-phase EDOT monomer and links them together (m2=69.27), producing nonvolatile MoCl3 and volatile HCl byproducts. Taking the ratio m2/ m1 = 0.254 vs. experimentally measured value of 0.255 from Figure 2.

theory (DFT) calculations to determine the oxidation potentials of the Mo(V)Cl5/Mo(IV)Cl4 and Mo(IV)Cl4/Mo(III)Cl3 redox couples as described in SI Section C. We calculated oxidation potentials of 3[240], and 1.46 V vs. SHE for the Mo(V)Cl5/Mo(IV)Cl4 and Mo(IV)Cl4/Mo(III)Cl3 redox couples, respectively. A subset of the monomer and oxidant redox potential values have been reported in previous literature and we compare our results against prior reports in SI Sections B and C. An energy diagram of these cumulative results is presented in Figure 4.

In Figure 4, we use the relative oxidation potentials at room temperature from nonaqueous electrochemical measurements and DFT calculations within a vacuum corrected to room temperature as surrogates to identify qualitative trends in the relative oxidation/reduction strength of the monomers and oxidant. Although the oMLD process is carried out at elevated temperature in the gas phase, these reference values provide a conceptual view of the driving forces for oMLD reaction. In Figure 4, the oxidation potentials of Fu and Thi monomers are 1.91 V and 1.72 V vs SHE, respectively[242], which are higher than the oxidation power of Mo(IV)Cl4 →Mo(III)Cl3 (1.46 V vs SHE). Although the Mo(V)Cl5/Mo(IV)Cl4 redox couple is capable of oxidizing one Fu or Thi monomer, the Mo(IV)Cl4/Mo(III)Cl3 couple has insufficient oxidizing power to oxidize a second monomer and drive surface polymerization, preventing the oMLD reaction from propagating further. Conversely, the oxidation potentials of EDOT, PDA, and Py of 1.21, 0.74 and 0.87 V vs. SHE fall below the oxidation power of Mo(V)Cl5→Mo(IV)Cl4 and Mo(IV)Cl4 →Mo(III)Cl3 , allowing for continued polymer growth of pEDOT, pPDA, and pPy. We also note that oMLD using the 3HT monomer5 is viable due to the electron withdrawing hexyl group which lowers the onset potential for oxidation, similar to the

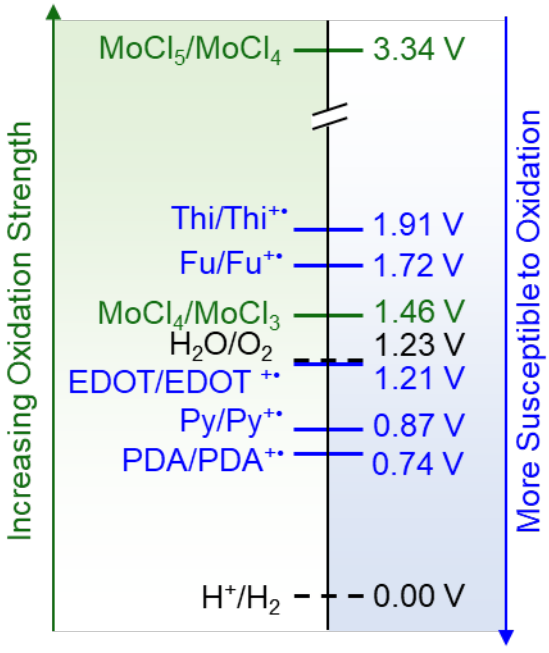

Figure 4.4: We identify that relative oxidation/reduction potentials can be used as a descriptor to predict the success of a monomer/oxidant combination for an oMLD chemistry. In this schematic depiction, the reduction potentials of oxidants and monomers studied in this work are plotted vs SHE. Oxidants are shown in green and monomers are in blue. Stronger oxidants appear at higher (more positive) potentials and monomers that are more susceptible to oxidation appear at lower (more negative) potentials. The Mo(IV)Cl4/Mo(III)Cl3 redox couple does not have sufficient oxidation strength to oxidize Fu or Thi monomers.

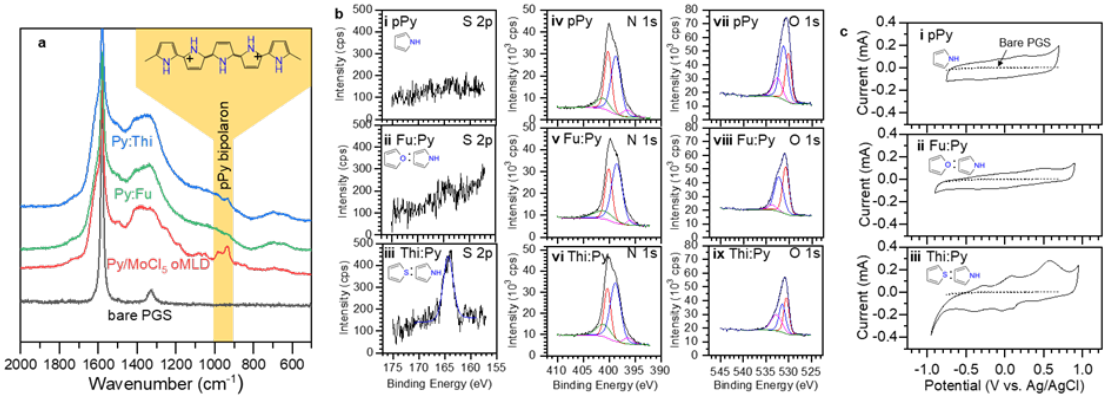

Figure 4.5: Alternating between Py and Fu/Thi monomer doses allows for incorporation of Fu and Thi into oMLD pPy films. (a) Raman spectroscopy of oMLD pPy as well as pPy:Fu and pPy:Thi formed by alternating 10 cycles Py and 10 cycles Fu or Thi oMLD chemistries. pPy bipolaron bands at 900-1000 cm-1 are removed by Fu/Thi incorporation. (b) XPS analysis after Fu/Thi incorporation into pPy oMLD films showing S 2p (i-iii), N 1s (iv-vi), and O 1s (vii-ix) bands analyzed for pPy (i:S, iv:N, vii:O), pPy:Fu (ii:S, v:N, viii:O), and pPy:Thi (iii:S, vi:N, ix:O). Broadening and shifting of the O 1s peak confirmed incorporation of O from Fu in (viii), while S from Thi was confirmed to incorporate into pPy:Thi in (iii). (c) CV of (i) oMLD pPy (ii) pPy:Fu, and (iii) pPy:Thi on PGS substrate, where incorporating Fu and Thi enhances the electrochemical capacity and potential window for activity.

ethylene dioxyl group on EDOT. While the mechanistic insights provided above explain why pure pThi and pFu polymers are inaccessible by oMLD using the MoCl5 oxidant, this mechanistic picture also suggests that Thi or Fu monomers could be incorporated into pEDOT, pPy or pPDA polymers through controlled molecular assembly. Specifically, if a Py-MoCl5 adduct is present on the growth surface, based on the conceptual picture in Figure 4, the MoCl5 oxidant is expected to have enough oxidizing power to oxidize a gas-phase Thi (or Fu) monomer, as well as the surface Py monomer, allowing Thi (or Fu) to link to the surface Py and incorporate into the polymer structure. To confirm this, we performed oMLD in a two-stage series of 10 cycles each, alternating between a high oxidation potential monomer (Thi or Fu) and Py monomer doses for a total of 200 oMLD growth cycles. The resulting polymer films were analyzed by Raman, XPS, and CV in Figure 5.

In Figure 5a, the Raman bipolaron band at 900-1000 cm-1 indicating long-range order in oMLD pPy[243, 244] is disrupted through the addition of Fu and Thi monomers, indicating that the Fu and Thi monomers have incorporated into the film and are disrupting long-range order in the pPy films. The bipolaron molecular unit of pPy is depicted in the inset of Figure 5a for reference. Incorporation of Fu and Thi into pPy films was confirmed using XPS analysis in Figure 5b. Here, S 2p, N 1s, and O 1s peaks were used to analyze the incorporation of Fu (C4H4O) and Thi (C4H4S) monomers into pPy (C4H5N) polymer films. The clear presence of a shoulder in the O 1s peak for the Fu:Py

copolymer in Figure 5b.viii and the appearance of S in the Thi:Py copolymers in Figure 5b.iii provide strong support for the incorporation of Fu and Thi into pPy polymers through alternating chemical exposures. This further validates the mechanistic picture described above.

In Figure 5c, we observe a qualitative shift in the number and location of CV peaks when using only Py monomers (Figure 5c.i, 14.3 nm film thickness by SE) vs alternating between Py and Fu monomers (Figure 5c.ii, 15.4 nm film thickness by SE) and Py and Thi monomers (Figure 5c.iii 17.7 nm film thickness by SE). This further supports that Fu and Thi incorporate into the pPy polymer structure and suggests that the incorporation of these monomers impacts the thermodynamics for electron insertion/extraction into the pPy. The addition of Fu monomers to pPy through controlled molecular assembly through oMLD increases the voltage window of electrochemical activity by 0.45 V, and enhances the redox capacity from 267 mAh/g for pPy to 313 mAh/g for pPy:Fu. Likewise, the addition of Thi monomers to pPy through controlled molecular assembly through oMLD increases the voltage window for electrochemical activity by 0.15 V, and enhances the redox capacity from 267 mAh/g to 369 mAh/g. By assembling Py and Thi monomers together by oMLD we achieve a 38% enhancement in electrochemical capacity vs. oMLD pPy and achieve 90% of the maximum theoretical charge storage capacity of pPy of 411 mAh/g.24 This 369 mAh/g capacity exceeds the highest capacities reported for pPy to date[207, 245, 202] and represents a higher capacity than materials currently under consideration for next-generation materials for lithium-ion batteries[235, 151].

4.5 Conclusion

This work establishes a mechanistic picture for the surface reactions responsible for oMLD growth consisting of (1) complexation of a two-electron oxidant to a surface monomer and (2) the oxidation of both a surface and gas-phase monomer by the same oxidant molecule to link the gas-phase monomer to the surface. This mechanistic picture helps explain the success of two-electron metal pentachloride oxidants for oMLD and establishes a conceptual picture to guide future exploration of new oMLD growth processes, narrowing the focus to combinations of monomers and oxidants with complimentary oxidation potentials. New two-electron oxidants with higher oxidation strength may enable oMLD of Thi, Fu, and other monomers which are not as readily oxidized as Py, EDOT, PDA, or 3HT. Furthermore, our results suggest that a wide range of monomers with varying substituents can be used with established MoCl5, ReCl5, and SbCl5 oxidants to form polymers by oMLD. Additionally, the demonstration of molecularly assembled copolymers of Py with Fu and Thi monomers with enhanced electrochemical capacity over pure pPy provides a platform for tuning the molecular structure of

polymers to access improved electrochemical properties for applications including energy storage, water desalination, and sensing.

Chapter 5

ELECTROCHEMICAL PROPERTIES OF NANOSCALE POLYETHYLENEDIOXYTHIOPHENE (PEDOT) THIN-FILMS GROWN BY OXIDATIVE MOLECULAR LAYER DEPOSITION (OMLD)

5.1 Abstract

Poly(3,4-ethylene dioxythiophene) (pEDOT) exhibits high electrical conductivity and has a high theoretical charge storage capacity, making it of interest for electrochemical applications including energy storage, separation processes, and sensors. In this work, we employ vapor phase polymerization via oxidative molecular layer deposition (oMLD) to form nanoscale thin films of pEDOT and examine the effect of film thickness on microstructure and electrochemical properties. We identify changes in orientation of ordered pEDOT domains with film thickness that impact ion transport to and from liquid electrolyte and thereby influence charge storage capacity. We measure a low electrochemical capacity for 30 nm pEDOT films deposited using 60 oMLD cycles at 150°C. At this thickness, we identify that pEDOT adopts a predominantly face-on orientation that limits ion insertion due to poor access of ions into the interplanar space within pEDOT. We observe a transition to oblique (off-angle) orientations at higher thickness, in line with prior reports. We also observe an additional population of off-angle domains for thinner ($<$ 10 nm) pEDOT films. We posit that this mixed orientation allows for more facile anion insertion from the electrolyte into the pEDOT film, which, coupled with reduced length scales for solid state ion transport in these thinner films, yields high electrochemical capacities of $>$ 120 mAh/g for pEDOT thicknesses $<$ 10 nm. The insights we provide here into process-structure-property relationships for nanoscale thin films of pEDOT informs the

vapor growth of pEDOT thin films for advanced electrochemical devices and guides the development of new polymer structures to control electrochemical properties.

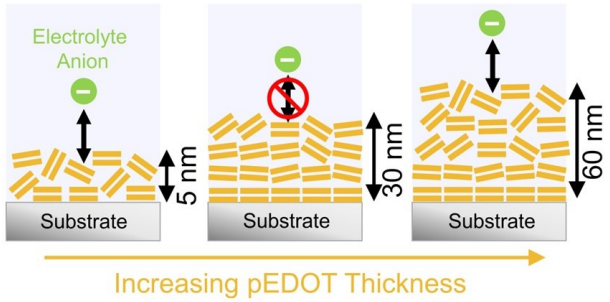

5.2 Introduction

The first recorded conjugated polymers were discovered more than 100 years ago: polyaniline (pAni) in 1832[246], and polypyrrole (pPy) in 1915[247]. Since these initial discoveries, conjugated polymers have been under continuous development, leading to a Nobel prize in chemistry in the year 2000 for the control of electrical conductivity over many orders of magnitude by tuning chemical doping in these polymers. In the late 1980s, poly(3,4-ethylene dioxythiophene) (pEDOT) was demonstrated to be highly electrically conductive, stable at elevated temperatures, and easily processable[248, 249, 250]. The electrical conductivity of pEDOT often surpassed previous conjugated polymers due to ethylene oxide groups on each 3,4-ethylene dioxythiophene (EDOT) monomer, which served to block reaction at the C positions of thiophene, and to act as electron donating groups to increase the susceptibility to oxidative doping[251]. In recent years, pEDOT has been used for bioelectronic devices, optoelectronics, thermoelectrics, light emitting diodes (LEDs), chemical sensors, electrochemical energy storage, organic photovoltaics, desalination, nanoelectronics, and much more[236, 252, 232, 253, 234]. Many of these advanced technologies require control of matter at the nanoscale, which has motivated the development of new synthesis techniques to precisely form nanoscale pEDOT films. In early reports, the most common techniques to synthesize pEDOT were through (a) homogeneous oxidative chemical polymerization using a chemical oxidant such as iron(III) chloride (FeCl3),[249] or (b) electrochemical oxidation[254]. However, these synthesis methods cannot easily deliver uniform nanoscale films of < 100 nm. In the last thirty years, gas phase polymerization techniques have been developed to form pEDOT and other polymers as conformal films with nanoscale thickness control[255, 230, 256]. Gas phase polymerization of pEDOT has

been performed using vapor phase polymerization (VPP) starting in 2003[257], oxidative chemical vapor deposition (oCVD)[258] starting in 2006, and oxidative molecular layer deposition (oMLD)[46] starting in 2014. In VPP, a gas-phase monomer (EDOT) is delivered to a substrate coated with a non-volatile chemical oxidant, where it reacts to form polymer films. In oCVD, EDOT and a choice of oxidant (e.g. FeCl3) are mixed simultaneously in the gas phase and react to form polymer chains. In oMLD, the monomer (EDOT) and a volatile chemical oxidant such as molybdenum pentachloride (MoCl5) are dosed in alternating vapor-phase exposures with an inert carrier gas purge between each precursor pulse. Similar to other molecular layer deposition (MLD) processes[259, 178, 226], oMLD provides high uniformity and conformality when forming coatings on 3D substrates because it progresses via self-limiting reactions on material surfaces[46, **?**]. Because oCVD and oMLD do not require the use of side-chains or additives common in solution processing, they allow for the formation of chemically pure pEDOT thin films, and have been used to produce record electrical conductivities for pEDOT in excess of 6000 S/cm[231, 260]. In this study, we examine the electrochemical properties of thin-film pEDOT formed by oMLD. pEDOT undergoes reversible electrochemical oxidation under applied potential, forming cation radicals on the polymer backbone and concomitantly binding anions from solution to balance charge. Thin films of polymers reduce the length scale for solid state ion diffusion through the polymer films, which is expected to enhance the specific electrochemical charge storage capacity over bulk polymer films. For example, prior work examining nanoscale pAni formed by pulsed electrodeposition measured specific charge capacities of >130 mAh/g at thicknesses of < 30 nm[**?**], and studies of oMLD of pPy identified record capacities of 282 mAh/g for < 30 nm thick pPy films. Although the electronic properties of pEDOT formed by oCVD and oMLD have been studied extensively[46, 260, 232, 231, 229], only a few studies have examined the electrochemical charge storage properties of these pEDOT films[228, 238, 261, 262]. The impact of thickness on charge storage properties at these nanoscale thicknesses is important to inform the use of pEDOT films as protective coatings for Li-ion and other alkali-ion batteries[263, 264, 265], as active materials for supercapacitor electrodes for high power energy storage[234, 136], or as electrode materials for electrochemical water desalination[266, 267], among other applications.

5.3 Materials And Methods

5.3.1 Oxidative Molecular Layer Deposition

We employed a hot-walled viscous flow reactor64 with precursor configurations for oMLD deposition described previously.39,65 The reactor was held at 150°C using PID temperature control and 0.85 torr of inert argon carrier gas baseline pressure (UHP, 99.999% Ar) is maintained using a mass flow controllers. EDOT (A) and MoCl5 (B) were each held at 100 °C in stainless steel flow-over bubblers. Unless otherwise noted, one oMLD cycle consisted of an A:Purge:B:Purge dosing sequence employed a timing of 20:100:100:100, with each value in units of seconds. pEDOT was deposited onto PGS and 2 cm by 2 cm silicon flats. To perform each deposition, samples are placed on a stainless steel tray and loaded into the reactor chamber. The samples are heated under continuous argon purge in the reactor for at least 60 minutes prior to deposition.

5.3.2 Spectroscopic Ellipsometry

After oMLD, silicon flat samples were analyzed using spectroscopic ellipsometry (SE) with the J.A. Wollam Alpha-SE ellipsometer at wavelengths of between 300-800 nm at an incident angle 65 and analyzed using the CompleteEASE software package. The pEDOT thin films with thicknesses of 0-60 nm (0-100 oMLD cycles) were fit using a Cauchy model and then confirmed with neutron reflectivity (NR). Films $>$ 60 nm (150 and 175 oMLD cycles) were modelled using three Lorentz Oscillators centered at 2.14, 3.06, and 5.07 eV.

5.3.3 Neutron Reflectivity

Neutron reflectivity data was collected using the Grazing Incidence Neutron Spectrometer (GANS)66 with a wavelength of 2.35 Å at the University of Missouri research Reactor (MURR). Data analysis was performed using the Reflpak software, which utilizes the Parrat Method, accounting for the substrate, film layers, and layer interfaces to compute a fit curve to match the raw reflectivity data. Layer thickness(es) are obtained from Reflpak model fits.

5.3.4 Electrochemical Measurements

After oMLD deposition, PGS samples are cut into 2 by 2 cm square which is place in a custom glass electrochemical cell with a surface o-ring seal to expose 1.27 cm2 of sample surface area

to the electrolyte. A 6 mm graphite rod (99.9995%, Alfa Aeser) is used as a counter electrode with an Ag/AgCl reference electrode (BASi). Fresh electrolyte solutions of 0.1 M aqueous NaCl or 0.1 M Na2SO4 are mixed using 18.2 M deionized water for each electrochemical measurement, degassed by argon for 30 minutes and then pipetted into the cell under blanket Ar carrier gas purge. Electrochemical measurements are performed using a Biologic SP-150 potentiostat.

5.3.5 Raman Spectroscopy

Raman spectroscopy was conducted on PGS samples using a Renishaw inVia Raman Spectrometer with a 633 nm excitation laser. Data was collected over 500-2000 $cm^(-1) with a sweeping scan of 10 cm^(-1) / sand a laser power of 10.1 mW.$

5.3.6 Scanning Electron Microscopy

Following oMLD deposition, film thickness measurements were performed on cleaved PGS samples using a ThermoScientific Helios 5 Hydra operated in immersion mode at 2kV.

5.3.7 Grazing incidence wide angle X-ray measurement

Samples for GIWAXS were prepared on doped Si substrates. Measurements were performed at Brookhaven National Laboratory at the 12-ID Soft Matter Interfaces (SMI) beamline of the National Synchrotron Light Source II (NSLS-II) with a beam energy of 12 keV. The 2D scattering patterns were collected at an X-ray incidence angle of 0.1° with a Pilatus 900 KW detector with a pixel size of 172 µm placed at 279 mm from the sample.

5.4 Results And Discussion

Prior studies of pEDOT oMLD established saturating dose conditions for sequential pulses of EDOT and MoCl5 at 150°C using in situ quartz crystal microbalance (QCM) measurements[**?**]. These saturating conditions consisted of an MoCl5 dose time of 100 s, an EDOT dose time of 20 s, and 100 s purge times after each precursor dose. Here, we employ these growth conditions to deposit pEDOT thin films on Si and pyrolytic graphite sheet (PGS) samples using between 20 and 175 oMLD cycles. In Figure 1a, we report neutron reflectivity (NR) data for between 20 and 100 oMLD cycles on Si wafers. Overall, as the number of oMLD cycles increases, we observe narrower Kiessig fringes in the NR data, consistent with the formation of thicker pEDOT layers. The NR traces in Figure

1a for between 20 and 80 oMLD cycles were modeled using Reflpak[268], which utilizes the Parrat Method[187], and the fitted traces are shown in red in Figure 1a. These model fits account for the substrate, native oxide, and pEDOT film layers. Thickness values from these model fits agree with estimates using the Kiessig fringe widths visible in Figure 1a. At 20 oMLD cycles, the NR scattering data is indistinguishable from a bare Si wafer, corresponding to a 0.0 nm pEDOT thickness. We observe clear Kiessig fringes for samples formed by 40, 60, and 80 oMLD cycles, corresponding to fitted model thicknesses of 3.9, 27.1, and 39.8 nm, respectively. At 100 oMLD cycles, the Kiessig fringes are not well-defined, and the NR data is noisy, indicating the formation of a multi-phase or rough surface after 60 oMLD cycles.

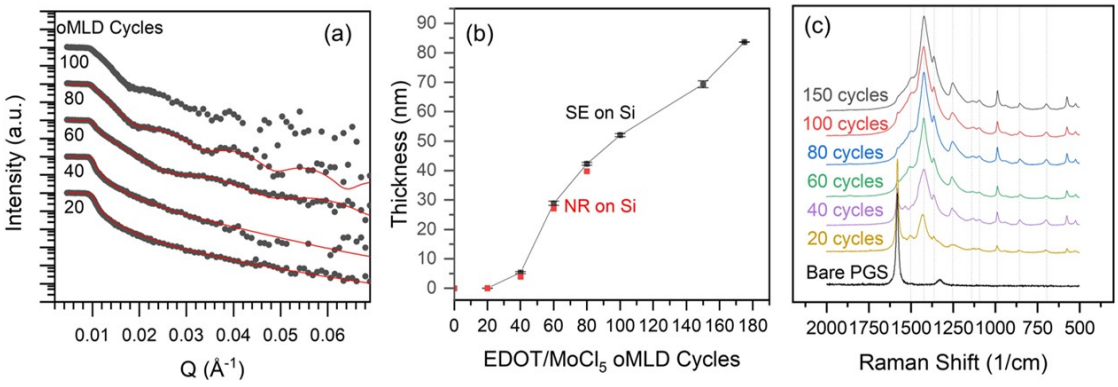

Figure 5.1: Growth behavior of pEDOT by EDOT/MoCl5 oMLD including (a) neutron reflectivity (NR) data for pEDOT thin films on Si using various numbers of oMLD cycles where the black circles are raw NR data and the red lines are model fits, (b) comparison between NR fitted thicknesses and spectroscopic ellipsometry (SE) model thickness for pEDOT, and (c) Raman spectra of pEDOT oMLD deposited films with reference lines for pEDOT.42 The Raman spectra in (c) are scaled to emphasize the pEDOT Raman peaks in each sample.

Increased roughness of films deposited using 100 or more oMLD cycles prevented measurement of film thickness by NR, so we employed spectroscopic ellipsometry (SE) to determine the thickness for these thicker films of pEDOT. Here, we established the optical properties pEDOT films by performing SE measurements on the NR samples in Figure 1a. The pEDOT film was fitted using a Cauchy model for thicknesses from 0 - 60 nm. This SE fitting yielded a refractive index of 1[269]. at a wavelength of

589 nm, consistent with a value of n = 1.6 reported previously[270]. The thicknesses from SE agreed with NR thicknesses within 3 nm. Using SE, we measured thickness values of 5.3, 28.9, 42.3, and 52.0 nm for 40, 60, 80, and 100 oMLD cycles, respectively. This Cauchy model did not provide a good fit for thicker oMLD pEDOT films formed using 150 and 175 oMLD cycles, which we attribute to decrease in the state of oxidation of the as-deposited pEDOT films at higher film thicknesses[271, 272]. To determine the thicknesses of these thicker films from the SE data, we employed an optical model comprising three Lorentz oscillators which captured the optical absorption observed in SE data for thicker films, yielding film thicknesses of 69.3 and 83.6 nm for 150 and 175 oMLD cycles, respectively. We observe a thickness of only 5 nm after 40 oMLD cycles, which we attribute to a nucleation delay in formation of the pEDOT films. After 40 oMLD cycles we observe a steep increase in thickness vs. number of oMLD cycles, and then a gradual levelling off to a steady-state growth rate of 0.45 nm/cycle between 60 and 175 oMLD cycles. We note that one EDOT monomer is 0.4 nm in width and 0.7 nm in length, such that a growth rate of 0.45 nm/cycle corresponds to the addition of 1 monomer per growth cycle in a vertical growth direction[273, 274]. To confirm the formation of pEDOT films, we employed Raman spectroscopy as depicted in Figure 1c. The vertical dashed lines in Figure 1c are reference Raman lines for pEDOT[275]. We observe the dominant Raman peaks for pEDOT at 1422, 1362, 1253, and 988 cm-1, corresponding to symmetric C=C(-O) stretch, C-C stretch, C-C'(inter-ring) stretch, and ethoxylene ring deformation, respectively[275]. We also observe minor peaks at 1503, 1139, 1092, 856, and 694 cm-1, corresponding to asymmetric C=C stretch, C-O-C deformation, and symmetric C-S-C deformation in pEDOT, respectively[275]. The Raman spectra for pEDOT films in Figure 1c are also consistent with previous oMLD and oCVD literature[232, 261, 269, 231] Raman spectra in Figure 1c were measured on PGS substrates used for electrochemical measurements below. We note that although 20 oMLD cycles yielded a thickness of 0 nm on Si, we see a clear Raman signal for pEDOT after 20 oMLD cycles in Figure 1c. The peak at 1580 cm-1 corresponds to the graphitic G-band from the PGS substrate[276, 277]. As the number of oMLD cycles increases, this G-band peak at 1580 cm-1 is attenuated, indicating that the pEDOT film thickness is increasing and preventing Raman sampling from the underlying PGS substrate. Here, we calculate the thickness of films deposited using $<$ 60 oMLD cycles using the attenuated Raman signal53 from the PGS substrate at 1580 cm-1.53 For this analysis, we calibrate the attenuated Raman signal assuming the pEDOT thickness is 33 nm after 60 oMLD cycles based on SEM analysis (vide infra), and we calculate thicknesses of 4.0 nm and 9.2 nm for pEDOT films grown on PGS using 20 and 40 oMLD cycles, respectively. After establishing control over the thickness of nanoscale oMLD pEDOT films in Figure 1, we examined the electrochemical charge storage capacity

at different film thicknesses using cyclic voltammetry (CV) in Figure 2a. This CV data is collected in 0.1 M Na2SO4 at circumneutral pH at a sweep rate of 50 mV/s for pEDOT thin films formed using 20-150 oMLD cycles (i-v, respectively) on PGS substrates. The charge storage on the oxidizing sweep, Qox, can be calculated as the area under the curve $Q_o x = 1/v_(V_0)^(V_f) i(V)$ dV where V0 is the lower limit of voltage (here -0.75 V vs. Ag/AgCl), Vf is the upper limit of voltage (here 0.75 V vs. Ag/AgCl), i(V) is the current measured at each voltage, and v is the sweep rate, e.g. in mV/s. As expected, we observe an increase in the amount of charge stored (listed as Q in each panel of Figure 2a) with an increasing number of oMLD cycles, where the largest amount of stored charge is observed for the 150 oMLD cycles sample. As the film thickness increases, we also observe the emergence of typical CV character expected for pEDOT, with two equilibrium potentials at -0.4 and 0.1 V vs. Ag/AgCl,12 corresponding to anion insertion redox processes and structural reconfiguration[278, 279]. However, surprisingly, the sample deposited using 60 oMLD cycles stores less charge than the sample deposited using 40 oMLD cycles. Typically, one would expect that a thicker film would yield a higher charge capacity at a fixed sweep rate due to a larger mass of redox-active material present on the electrode, as has been observed for organic and inorganic redox-active thin films in previous work[**?**, **?**, 280, 281, 282].

To put the decrease in capacity at 60 oMLD cycles in perspective, it is useful to examine the specific charge capacity (capacity per unit mass) at each film thickness. For this, we first confirmed the thickness of pEDOT films on PGS substrates using scanning electron microscopy (SEM) on cleaved samples. After 60 and 100 oMLD cycles we measured mean pEDOT thicknesses of 33 ± 3 nm and 66 ± 3 nm, respectively, each based on five SEM measurements on each sample as depicted in Figure 2b. These mean thickness values are 4 and 11 nm higher, respectively, than the thicknesses of 28.9 and 52.0 nm measured on Si wafers after 60 and 100 oMLD cycles in Figure 1b. We note that Si wafers were included in the same deposition runs along with the PGS substrates and the thicknesses on these Si witness wafers were consistent with the thickness values presented in Figure 1b. We attribute the (up to) 21 % higher thickness on PGS substrates to differences in adsorption and growth characteristics of -aromatic molecules onto graphitic carbon surfaces compared with the native silicon oxide present on Si substrates. For comparison, the adsorption of benzene onto SiO2 has been measured to have an adsorption energy of -16 kJ/mol[283], whereas the adsorption of benzene onto graphene has an adsorption energy of -22 kJ/mol by DFT calculations[284]. As noted in Figure 1b above, deposition of pEDOT oMLD on Si wafers exhibits a nucleation delay of >20 oMLD cycles, consistent with the weaker adsorption of EDOT onto native SiO2 on Si wafers. In Figure 2c, we plot

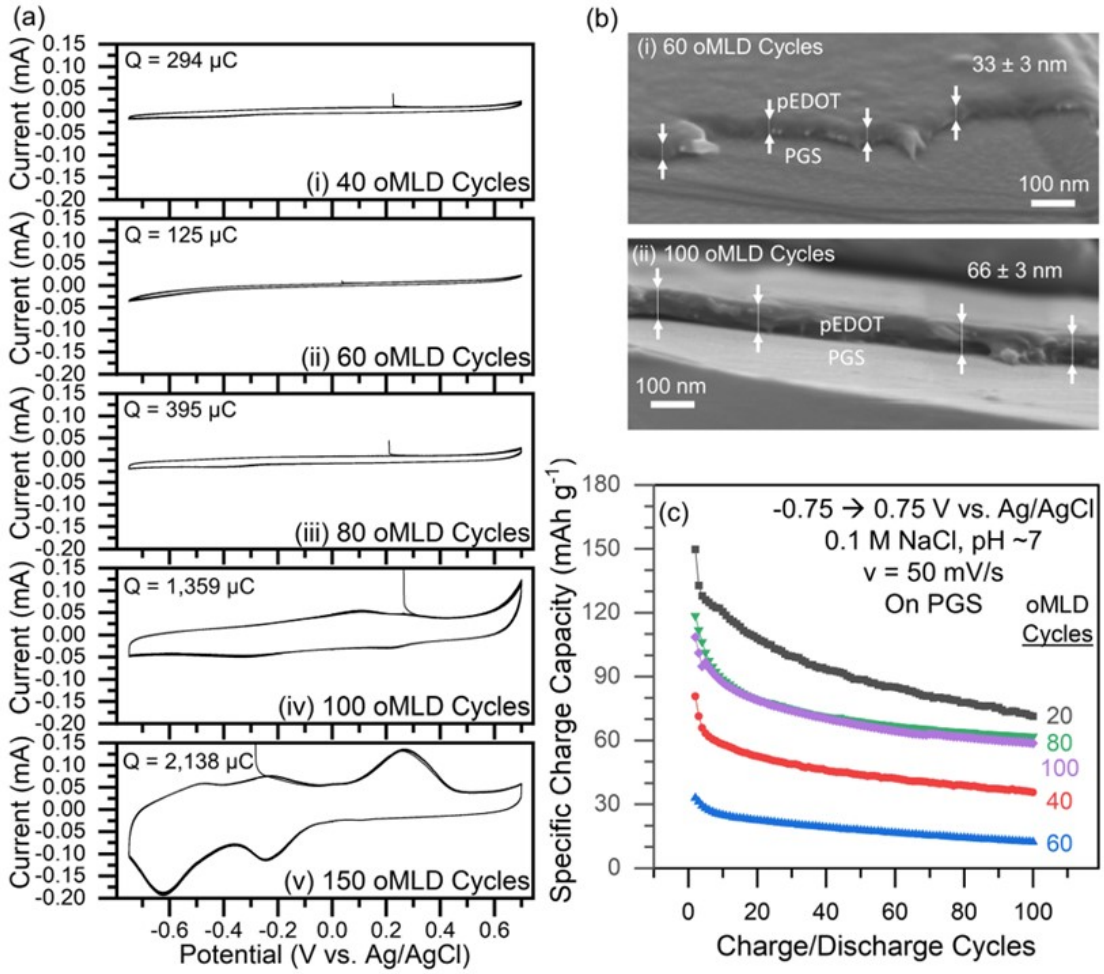

Figure 5.2: (a) Electrochemical response curves (cyclic voltammetry) of oMLD deposited pEDOT films (i 40, ii 60, iii 80, iv 100, v 150 Cycles) on PGS (substrate) over a 1.5 V (-0.75 0.75 V) potential window in 0.1 M Na2SO4 solution with 50 mV/s sweep rate. (b) SEM images (i) 60 and (ii) 100 oMLD cycles of pEDOT film thicknesses (33 ± 3 nm and 66 ± 6 nm) on PGS substrate. (c) Specific charge capacity of 40, 60, 80, 100 oMLD cycles pEDOT films in 0.1 M NaCl vs. charge/discharge cycles over 100 cycles, where 60 pEDOT oMLD cycles has lowest charge capacity.

the specific charge storage capacities vs. cycle number from CV data collected up to 100 CV cycles at a sweep rate of 50 mV/s. Here we calculate the net charge arising from redox reactions in the pEDOT film as Qnet = QOx-QPGS, where QPGS is the capacity arising from double layer charge storage measured on a bare PGS substrate from a control experiment (QPGS = 22.63 nAh at a sweep rate of 50 mV/s). We then divide Qnet in each CV cycle by the total mass of pEDOT at each number of oMLD cycles. The mass of the pEDOT film, m, is calculated as m=V, where = 1.5 g/cm3 is taken as the density of pEDOT,46,47 and the volume of the film is $V = tr^2$, where t is the thickness of the film, and r = 0.635 cm is the radius of the circular area exposed to the electrolyte for these CV measurements. The thickness, t, of the 60 and 100 oMLD cycle films were taken to be 33 and 66 nm,

respectively based on SEM imaging in Figure 2b. The thicknesses of the 20 and 40 oMLD cycle films were taken to be 4.0 and 9.2 nm, respectively based on Raman spectroscopy analysis calibrated to the 60 oMLD cycle sample SEM thickness (described above in Figure 1c). The thickness of the 80 oMLD cycle sample was taken to be 50 nm – the average of the 60 and 100 oMLD cycle films measured by SEM in Figure 2b. Using these thickness values, the highest specific charge capacity (133 mAh/g on the third CV cycle) is observed for the thinnest (4 nm) pEDOT film grown using 20 oMLD cycles. This observation is consistent with previous reports showing that thinner films of redox active films (both organic and inorganic) yield higher electrochemical capacities arising from a shorter length scale for solid state ion diffusion. 22,25,56–58 we calculate specific mass capacities on the third CV cycle for 40, 80, and 100 pEDOT oMLD cycle films of 71, 112, and 101 mAh/g, respectively. After 100 CV cycles, we measure specific charge capacities of 71, 36, 62, and 59 mAh/g at a sweep rate of 50 mV/s for 20, 40, 80, and 100 oMLD cycles, respectively, which are consistent with specific mass capacities of 65 mAh/g reported previously for pEDOT.11 We note that the specific capacities of 100-140 mAh/g we measure during initial CV cycling for 20, 80 and 100 oMLD cycle pEDOT films are a factor of 2 higher than typical values.11 These values are 60% of the theoretical limit of 190 mAh/g for pEDOT,11 and are similar to capacities of 120 mAh/g measured for thicker (200-300 nm) films of pEDOT grown by oCVD.31 Consistent with the lower charge capacity measured in Figure 2.a.ii, we also observe the lowest specific charge capacity for the 60 oMLD cycle condition in Figure 2c. The specific capacity on the third CV cycle is only 31 mAh/g, and decreases after 100 CV cycles to 12 mAh/g. On average, over 100 CV cycles the 60 oMLD cycle film (33 nm) exhibits a specific charge capacity that is 60 ± 3% lower than the 40 oMLD cycle (9 nm) film, and 74 ± 3% lower than the 100 oMLD cycle (66 nm film). As shown in Figure 1c, the Raman features observed for the pEDOT film deposited at 60 oMLD cycles are equivalent to the pEDOT formed using 40 or 100 oMLD cycles. Therefore, we do not expect that these lower capacities arise from differences in chemical structure. Instead, we hypothesize that the decrease in electrochemical capacity for the 60 oMLD cycle film originates from differences in ion transport behavior due to microstructure changes within the pEDOT film at different film thicknesses. Specifically, we hypothesized that the orientation of pEDOT domains within oMLD films varies with film thickness and impacts the rate of anion uptake from the electrolyte into the pEDOT interchain spacing. This concept was based on observations in prior work on oCVD pEDOT showing that orientation varies with deposition temperature,24 and that the charge capacity in pEDOT varies with molecular and microstructure orientation.31 To examine this hypothesis, we performed grazing incidence wide-angle X-ray scattering (GIWAXS). Shown in Figure 3 are GIWAXS data for oMLD films grown on Si wafers using (a) 40 oMLD cycles,

(b) 60 oMLD cycles) and (c) 100 oMLD cycles. Here, Si wafer substrates were employed to provide an optically flat surface for GIWAXS measurements and increase signal quality. Each panel in Figure 3 shows both (i) the raw two-dimensional (2D) GIWAXS scattering data and (ii) line scans of the raw GIWAXS data at each of three azimuthal angle () values. The line scans at each value are depicted in (i) of each panel. In the raw 2D data for 40 oMLD pEDOT cycles, we observe a broad scattering peak in the vertical scattering direction at q = 1.82 Å-1, corresponding to the (020) lattice spacing for pEDOT[260, 261, 269, 282]. The surface of each sample is aligned horizontally in the xy plane, and scattering in the vertical direction at qz = 1.82 Å-1 indicates that the (020) lattice plane is parallel with the sample surface, i.e. in a face-on orientation. The dashed red arc in Figure 3a traces the constant value of q = 1.82 Å-1, and we observe that the scattering is not limited to the vertical direction, but is spread out at a range of angles around this ring at q=1.82 Å-1. This indicates that after 40 oMLD cycles some of the pEDOT is oriented in an oblique orientation (i.e. tilted at an angle with respect to the substrate surface).

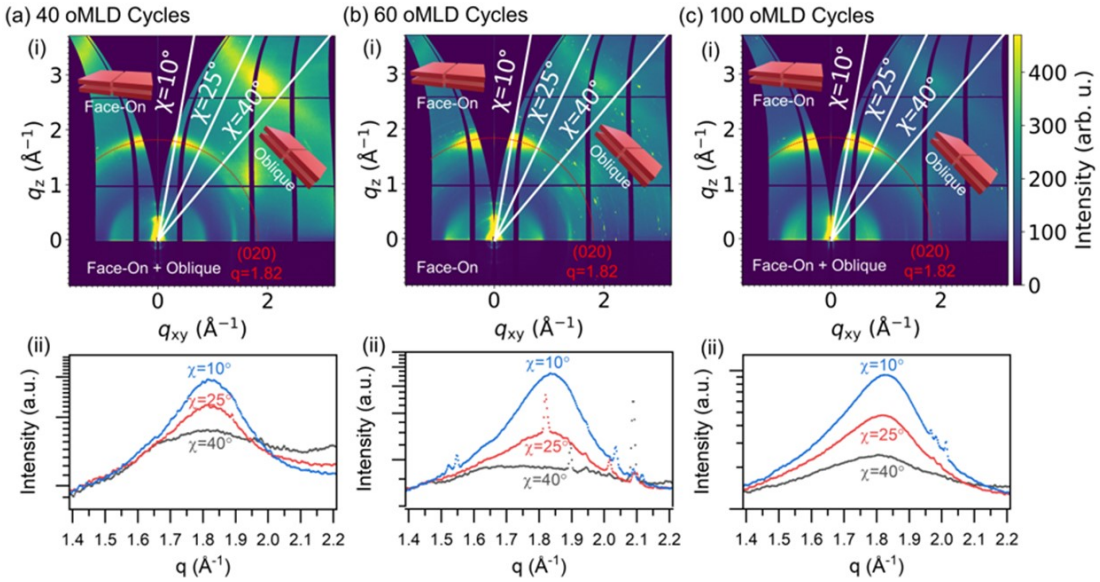

Figure 5.3: GIWAXS data indicates that pEDOT domain orientation changes with the number of oMLD cycles. Raw 2D GIWAXS data (top row), showing primarily face-on orientation of pEDOT oMLD films of 40, 60, and 100 oMLD cycles, with some domains at oblique angles to the surface. Further GIWAXS data analysis (bottom row) of peak height at radial position of q=1.82 Å-1 corresponding to the (020) pEDOT plane at azimuthal angles of = 10°, = 25°, and = 40° (indicated with white lines in the top row) showing more oriented face-on domains for 60 oMLD cycles compared with 40 and 100 oMLD cycles.

In Figure 3a.ii, we plot the scattering peak around q = 1.82 Å-1 for each of three azimuthal angles, = 10°, = 25°, and = 40°. For each of these line scans, the scattering data was integrated over a

range of 5 degrees centered on the indicated angle. In Figure 3a, we observe the strongest scattering intensity at = 10°, but we observe only a small decrease in peak intensity at = 25°, and significant scattering intensity remains at = 40°. Compared to = 10°, the scattering intensities above the baseline at = 25° and = 40° are 28% and 60% lower in intensity for the 40 oMLD cycle pEDOT film (calculated using the peak height above a linear baseline for each data set). This indicates that a portion of pEDOT domains are oriented at oblique angles of up to 40° relative to the plane of the surface. Scattering signal at > 40° from oblique ordered pEDOT domains is obfuscated by scattering signal arising from the bare Si substrate, which is visible in Figure 3a.i as a spot centered at the coordinates qz = 1.2 Å-1 , qxy = 1.7 Å-1. We expect that the presence of pEDOT at oblique angles of up to 40° allows anions to insert into the edges of the ordered pEDOT domains from the electrolyte, giving rise to higher electrochemical capacity for the 40 and 20 oMLD cycle films relative to the 60 oMLD cycle film in Figure 2c. After 60 EDOT/MoCl5 cycles, we observe predominantly face-on orientation of the (020) peak in the vertical (qz) direction in the raw GIWAXS data in Figure 3b.i. To further confirm this observation, in Figure 3b.ii we plot the scattering intensity after 60 oMLD cycles along each of the same azimuthal angles examined above in Figure 3a. For the 60 oMLD cycle sample, we observe that the scattering intensity around q=1.82 Å-1 is highest at = 10°, and exhibits a sharp drop-off in intensity for = 25°, and no distinguishable peak at = 40°. The scattering intensities above the baseline at q=1.82 Å-1 for = 25° and = 40° are 51 % and 86 % lower than at = 10° for the 60 oMLD cycle condition Figure 3b.ii. These decreases in intensity are 23 % and 26 % greater, respectively, than we observed for the 40 oMLD cycle pEDOT film in Figure 3a. These data further confirm that the ordered pEDOT domains at the 60 cycle oMLD condition consist of a greater degree of preferred face-on orientation relative to the 40 oMLD condition. The increased face-on orientation of the pEDOT film helps to explain the lower electrochemical capacity observed after 60 oMLD cycles in Figure 2c. Anions from the electrolyte are expected to transport through edge planes into the interplane space between pEDOT chains. Face-on pEDOT domains are expected to have fewer edge planes exposed to the electrolyte, which restricts anion transport and reduces electrochemical capacity in Figure 2c. After 100 oMLD cycles, we again observe more diffuse scattering intensity for the (020) scattering peak in the raw GIWAXS data in Figure 3c.i, similar to the behavior observed for 40 oMLD cycles in Figure 3a.i. This indicates that the pEDOT domains are again in a mixed orientation, with some face-on and some at oblique angles relative to the sample surface. In Figure 3c.ii we plot the scattering intensity after 100 oMLD cycles along azimuthal angles of = 10°, = 25° and = 40°. For the 100 oMLD cycle sample, we observe less of a decrease in peak intensity at q=1.82 Å-1 for = 25° and we still observe a substantial scattering peak at = 40°. Compared to = 10°, the

scattering intensities above the baseline at q=1.82 Å-1 for = 25° and = 40° are 33 % and 70 % lower in Figure 3c.ii. These decreases in intensity are similar to the values we measured for the 40 oMLD cycle pEDOT film in Figure 3a. These data indicate that the pEDOT domains are primarily aligned in a face-on orientation at 60 oMLD cycles, but this oriented alignment is lost with an increased film thickness. This trend is consistent with the electrochemical capacities observed in Figure 2c, where the 60 oMLD cycle film has the lowest electrochemical capacity, and the samples with 40 and 100 oMLD cycles both exhibit higher specific charge capacities. We expect that the formation of more oriented face-on pEDOT films at 60 oMLD cycles (30 nm) arises because this thickness corresponds to a point at which the thermodynamic driving forces transition from nucleation/surface effects to bulk film growth. In prior studies, the orientation of pEDOT domains in thin films has been found to vary with of film thickness and temperature for films deposited using vapor deposition (oCVD).24 In general, the orientation of pEDOT films transitions from (a) a face-on orientation for thinner (< 50 nm) pEDOT films and higher deposition temperatures to (b) a edge-on orientation for thicker (> 100 nm) pEDOT films and lower deposition temperatures.24 This prior work indicates that the formation of edge-on films is kinetically controlled, where thicker films are kinetically trapped in an edge-on orientation, and the formation of face-on films is thermodynamically preferred if sufficient thermal energy is provided and the polymer chains are susceptible to reconfiguration to organize in a face-on orientation. Interestingly, here we identify a new regime for films < 10 nm where the pEDOT ordered domains transition away from face-on orientation and exhibit oblique character in Figure 3a. We propose that this mixed orientation occurs due to energetic effects surrounding early nucleation. We note that density functional theory studies identify that heteroatom-containing -aromatic small molecules prefer a T-shaped dimer geometry by 10-20 kJ/mol over a parallel stacked geometry.60 Furthermore, thiophene has been found to prefer oblique-angle configurations when clustering in three or four molecule units over two molecule clusters due to additional stabilization from intermolecular interactions[260]. Based on these trends in small molecule interactions, we attribute the mixed orientation (Figure 3a) and higher electrochemical capacity (Figure 2c) we observe for pEDOT at 40 oMLD cycles to noncovalent intermolecular effects among pEDOT chains within a confined nanoscale film geometry at < 10 nm thickness. We note that one EDOT monomer is 0.4 nm in width and 0.7 nm in length.41,42 Assuming that the thickness of the film corresponds to polymer chain length, a 9 nm thick pEDOT film corresponds to oligomers comprised of 15 monomer units. 46,47 After establishing a conceptual picture for the trends in specific charge capacity vs. thickness we observed in Figure 2, we now examine the charge rate capability at varying sweep rates of 10-200 mV/s for pEDOT films deposited using between 20 and 100 oMLD cycles (4-66 nm) in Figure 4. We note

that, with the exception of the 20 and 40 nm films in Na2SO4 electrolyte, 100 CV cycles at 50 mV/s were performed on each of these samples prior to sweep rate analysis to bring the films to their steady-state electrochemical performance (see Figure 2c). The two thinnest films (20 and 40 oMLD cycles) were measured here without 100 CV pre-cycles to evaluate the ion insertion kinetics in the as-formed films. In Figure 4a and 4b, we compare the specific charge capacity vs. sweep rate in NaCl and Na2SO4 electrolyte. In general, we find that the trends in electrochemical capacity agree closely between the two electrolytes. We attribute the lower charge capacities for 20 and 40 oMLD cycles in 0.1 NaCl vs Na2SO4 to degradation in capacity during the 100 CV precycles (see Figure 2c). In Figure 4a and 4b, we observe specific charge capacities of 60 mAh/g at moderate sweep rates (50-200 mV/s) for films formed using 20, 80 and 100 oMLD cycles in NaCl electrolyte and for films formed using 80 and 100 oMLD cycles in Na2SO4 electrolyte. These electrochemical capacities in line with typical charge capacities measured for pEDOT.11 We observe maximum specific charge capacities at a sweep rate of 10 mV/s for the 20 oMLD cycle (4 nm) pEDOT film. At this film thickness and sweep rate, we measure specific charge capacities of 116 mAh/g in NaCl after 100 CV cycles, and 151 mAh/g in Na2SO4 with no CV pre-cycling in Figure 4a and 4b, respectively. This suggests that thinner (< 10 nm) pEDOT films should be used to maximize specific mass capacity, in line with prior reports of high capacities for thin-film redox-active materials. 22,25,56–58

Consistent with measurements at a sweep rate of 50 mV/s in Figure 2c, we observe the lowest values of specific charge capacities for the 60 oMLD cycle (33 nm) film thickness at all sweep rates in Figure 4a and 4b. At the highest sweep rate of 200 mV/s we observe minimum specific charge capacities for the 60 oMLD cycle (33 nm) film of 9 mAh/g in NaCl and 2 mAh/g in Na2SO4. These values are more than 10 and 70 times smaller, respectively, than the maximum values of specific mass capacity observed for the 4 nm oMLD films deposited using 20 oMLD cycles. To further confirm that these low capacities for the 60 oMLD cycle film arise from a diffusion limitation originating from face-on oriented pEDOT domains, we perform a log-log analysis of average current (iavg) vs. sweep rate () in Figure 4c. Here, the capacitive properties of pEDOT redox reactions are described by a constant phase element (CPE) according to the linear relationship $log(i_{avg}) = (1 - 0.5F_d)$ $log(V) + log(A)$ where fd is the fraction of diffusive charge storage character and A is a constant related to the specific capacitance of the CPE.56 Thus, in a plot of log(iavg) vs. log(), the slope, m = (1 – 0.5fd), can be used to quantify the capacitive or diffusive charge storage behavior, where at m = 1, the charge storage is purely capacitive and at m = 0.5 the charge storage is purely diffusive (restricted by diffusion). In Figure 4c, we observe that the 80 and 100 oMLD cycle films exhibit

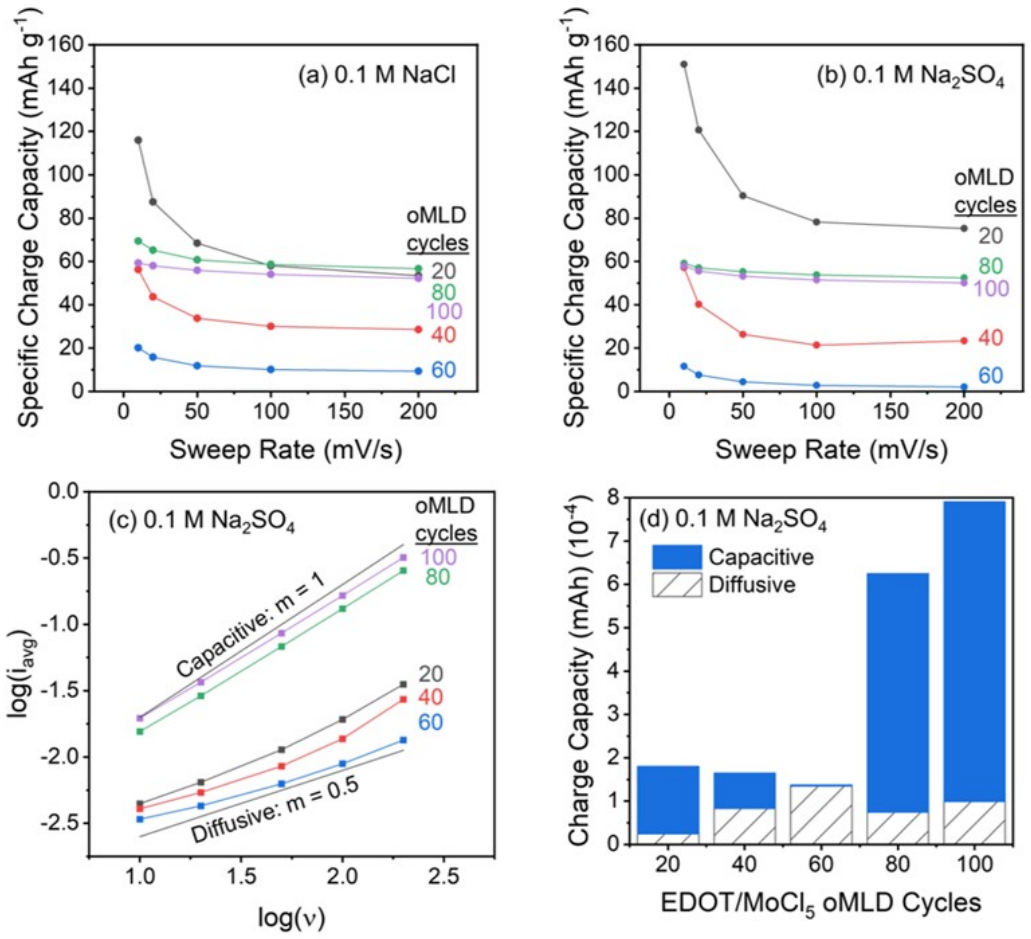

Figure 5.4: Charge rate analysis of nanoscale thin films of pEDOT including in (a) 0.1 M NaCl and (b) 0.1 M Na2SO4. We analyze the data in (b) using (c) a log-log plot to separate the capacitive and diffusive contributions to charge storage, and (d) plot the relative fractions of capacitive and diffusive contributions to the total charge capacities measured at a sweep rate of 10 mV/s.

nearly ideal capacitive behavior, whereas the 60 oMLD cycle film exhibits nearly ideal diffusive behavior. From Equation 1, we calculate fd = 0.62 for 20 oMLD cycles, fd = 0.76 for 40 oMLD cycles, fd = 0.98 for 60 oMLD cycles, and fd = 0.12 for both 80 and 100 oMLD cycles. We represent this data graphically in Figure 4d, where we plot the charge capacity measured at a sweep rate of 10 mV/s vs. the number of oMLD cycles with the capacity separated into capacitive and diffusive components. The lowest capacity is observed for the 60 oMLD cycle film and is restricted by diffusion limitations (fd = 0.98). This supports the mechanistic picture described above, where the face-on orientation of pEDOT domains at 60 oMLD cycles limits the number of edge-planes exposed to the electrolyte and prevents ion transport between the pEDOT film and the liquid electrolyte. Diffusion also restricts transport in the thinner 20 and 40 oMLD cycle films (fd = 0.5), but these films have

sufficient edge-planes exposed to the electrolyte to achieve a higher electrochemical capacity than at 60 oMLD cycles, despite having a smaller mass of pEDOT.

5.5 Conclusion

This work establishes electrochemical charge storage properties of nanoscale (< 100 nm) thin films of pEDOT grown using oMLD, a vapor phase deposition approach employing sequential surface reactions. We identify the formation of oriented face-on pEDOT films at a thickness of 30 nm on Si and PGS substrates. These oriented pEDOT films limit ion transport into the pEDOT layer during aqueous electrochemical measurements and restrict charge storage capacity to less than half of typical charge storage capacities observed for pEDOT. We find that increasing the pEDOT thickness to > 50 nm leads to a greater distribution of off-angle pEDOT orientations, allowing ions to diffuse from the electrolyte into the pEDOT film through edge-planes and increasing electrochemical capacity, consistent with previous studies on > 200 nm pEDOT films[261]. Surprisingly, we also observe that decreasing the thickness from 30 nm to < 10 nm also leads to oblique pEDOT domain orientations, while simultaneously reducing the length scale for ion transport, allowing pEDOT films of < 10 nm to achieve specific capacities of > 120 mAh/g after 100 electrochemical cycles, approximately two times higher than the value typically reported for pEDOT capacity[234].11 This report contributes to a growing number of studies[207, 261, **?**] demonstrating that vapor-phase polymerization (oMLD and oCVD) can be used to exceed commonly observed fractions of 30-50% of theoretical capacity that have long been considered upper limits on the electrochemical capacity of redox-active polymers[234]. We attribute the mixed orientation of pEDOT domains we observe for ultrathin (< 10 nm) pEDOT films to the energetics of molecular interactions in confined nanoscale pEDOT films during early nucleation, analogous to differences in geometric configuration observed as a function of the number of monomers in small-molecule clusters[50]. Recent work has begun to demonstrate the use of oMLD to control molecular-level assembly of monomer ordering copolymer structures[207, **?**]. As this work expands, new fundamental understanding of noncovalent intermolecular interactions between these polymer structures with varying molecular ordering will be critical to understand and control the electrochemical properties of these materials to achieve desired electronic and ion-insertion properties. Broadly, control over the electronic and ion-insertion electrochemical properties of these polymers promises to enable high-energy supercapacitors[234, 136] protective coatings for electrode materials in advanced (e.g. Li-ion) batteries[263, 264, 265], electrochemical separations[266, 267], electrochemical sensors to target trace contaminants, and much more[236, 252, 232, 253, 234].

BIBLIOGRAPHY

[1] D. Hinrichsen and J. Rowley, "Planet earth 2025. a look into a future world of 8 billion humans," *People & the planet*, vol. 8, no. 4, pp. 14–15, 1999.

[2] S. L. Postel, "Water and world population growth," *Journal-American Water Works Association*, vol. 92, no. 4, pp. 131–138, 2000.

[3] A. Maddocks, R. S. Young, and P. Reig, "Ranking the world's most water-stressed countries in 2040," 2015.

[4] J. Best, "Anthropogenic stresses on the world's big rivers," *Nature Geoscience*, vol. 12, no. 1, pp. 7–21, 2019.

[5] E. Curry, "Water scarcity and the recognition of the human right to safe freshwater," *Nw. UJ Int'l Hum. Rts.*, vol. 9, p. 103, 2010.

[6] F. Roudi-Fahimi, L. Creel, and R.-M. De Souza, *Finding the balance: Population and water scarcity in the Middle East and North Africa*. Population Reference Bureau Washington, DC, 2002.

[7] L. Zhang, M. R. Hipsey, G. Zhang, B. Busch, and H. Li, "Simulation of multiple water source ecological replenishment for chagan lake based on coupled hydrodynamic and water quality models," *Water Science and Technology: Water Supply*, vol. 17, no. 6, pp. 1774–1784, 2017.

[8] A. Maxmen, "As cape town water crisis deepens, scientists prepare for'day zero'." *Nature*, vol. 554, no. 7690, pp. 13–15, 2018.

[9] N. W. Arnell, "Climate change and global water resources: Sres emissions and socio-economic scenarios," *Global environmental change*, vol. 14, no. 1, pp. 31–52, 2004.

[10] R. Jain, "Providing safe drinking water: a challenge for humanity," pp. 1–4, 2012.

[11] C. Emenike, I. Tenebe, D. Omole, B. Ngene, B. Oniemayin, O. Maxwell, and B. Onoka, "Accessing safe drinking water in sub-saharan africa: Issues and challenges in south–west nigeria," *Sustainable cities and society*, vol. 30, pp. 263–272, 2017.

[12] O. C. Nweke and W. H. Sanders III, "Modern environmental health hazards: a public health issue of increasing significance in africa," *Environmental health perspectives*, vol. 117, no. 6, pp. 863–870, 2009.

[13] J.-A. Walker, "Achieving health sdg 3 in africa through ngo capacity building-insights from the gates foundation investment in partnership in advocacy for child and family health (pacfah) project," *African Journal of Reproductive Health*, vol. 20, no. 3, pp. 55–61, 2016.

[14] A.-E. Birn, "Philanthrocapitalism, past and present: The rockefeller foundation, the gates foundation, and the setting (s) of the international/global health agenda," *Hypothesis*, vol. 12, no. 1, p. e8, 2014.

[15] V. A. Tzanakakis, N. V. Paranychianakis, and A. N. Angelakis, "Water supply and water scarcity," p. 2347, 2020.

[16] F. Ntengwe, "Pollutant loads and water quality in streams of heavily populated and industrialised towns," *Physics and Chemistry of the Earth, Parts A/B/C*, vol. 31, no. 15-16, pp. 832–839, 2006.

[17] C. Fritzmann, J. Löwenberg, T. Wintgens, and T. Melin, "State-of-the-art of reverse osmosis desalination," *Desalination*, vol. 216, no. 1-3, pp. 1–76, 2007.

[18] M. N. Soliman, F. Z. Guen, S. A. Ahmed, H. Saleem, M. J. Khalil, and S. J. Zaidi, "Energy consumption and environmental impact assessment of desalination plants and brine disposal strategies," *Process Safety and Environmental Protection*, vol. 147, pp. 589–608, 2021.

[19] N. Drouiche, N. Ghaffour, M. W. Naceur, H. Mahmoudi, and T. Ouslimane, "Reasons for the fast growing seawater desalination capacity in algeria," *Water resources management*, vol. 25, no. 11, pp. 2743–2754, 2011.

[20] J. Imbrogno and G. Belfort, "Membrane desalination: where are we, and what can we learn from fundamentals?" *Annual review of chemical and biomolecular engineering*, vol. 7, pp. 29–64, 2016.

[21] M. T. Ali, H. E. Fath, and P. R. Armstrong, "A comprehensive techno-economical review of indirect solar desalination," *Renewable and Sustainable Energy Reviews*, vol. 15, no. 8, pp. 4187–4199, 2011.

[22] N. Ghaffour, J. Bundschuh, H. Mahmoudi, and M. F. Goosen, "Renewable energy-driven desalination technologies: A comprehensive review on challenges and potential applications of integrated systems," *Desalination*, vol. 356, pp. 94–114, 2015.

[23] M. Qasim, M. Badrelzaman, N. N. Darwish, N. A. Darwish, and N. Hilal, "Reverse osmosis desalination: A state-of-the-art review," *Desalination*, vol. 459, pp. 59–104, 2019.

[24] A. Karabelas, C. Koutsou, M. Kostoglou, and D. Sioutopoulos, "Analysis of specific energy consumption in reverse osmosis desalination processes," *Desalination*, vol. 431, pp. 15–21, 2018.

[25] Q. Wu, D. Liang, S. Lu, H. Wang, Y. Xiang, D. Aurbach, E. Avraham, and I. Cohen, "Advances and perspectives in integrated membrane capacitive deionization for water desalination," *Desalination*, vol. 542, p. 116043, 2022.

[26] K. Maheshwari and M. Agrawal, "Advances in capacitive deionization as an effective technique for reverse osmosis reject stream treatment," *Journal of Environmental Chemical Engineering*, vol. 8, no. 6, p. 104413, 2020.

[27] M. Al Radi, E. T. Sayed, H. Alawadhi, and M. A. Abdelkareem, "Progress in energy recovery and graphene usage in capacitive deionization," *Critical Reviews in Environmental Science and Technology*, pp. 1–57, 2021.

[28] H. Liang, F. Chen, R. Li, L. Wang, and Z. Deng, "Electrochemical study of activated carbon-semiconducting oxide composites as electrode materials of double-layer capacitors," *Electrochimica Acta*, vol. 49, no. 21, pp. 3463–3467, 2004.

[29] C. Tan, C. He, J. Fletcher, and T. D. Waite, "Energy recovery in pilot scale membrane cdi treatment of brackish waters," *Water Research*, vol. 168, p. 115146, 2020.

[30] L. Kistner, F. L. Schubert, C. Minke, A. Bensmann, and R. Hanke-Rauschenbach, "Techno-economic and environmental comparison of internal combustion engines and solid oxide fuel cells for ship applications," *Journal of Power Sources*, vol. 508, p. 230328, 2021.

[31] S. Porada, L. Borchardt, M. Oschatz, M. Bryjak, J. Atchison, K. Keesman, S. Kaskel, P. Biesheuvel, and V. Presser, "Direct prediction of the desalination performance of porous

carbon electrodes for capacitive deionization," *Energy & Environmental Science*, vol. 6, no. 12, pp. 3700–3712, 2013.

[32] F. He, P. Biesheuvel, M. Z. Bazant, and T. A. Hatton, "Theory of water treatment by capacitive deionization with redox active porous electrodes," *Water research*, vol. 132, pp. 282–291, 2018.

[33] W. Zhao, M. Ding, L. Guo, and H. Y. Yang, "Dual-ion electrochemical deionization system with binder-free aerogel electrodes," *Small*, vol. 15, no. 9, p. 1805505, 2019.

[34] T. Zhang and F. Ran, "Design strategies of 3d carbon-based electrodes for charge/ion transport in lithium ion battery and sodium ion battery," *Advanced Functional Materials*, vol. 31, no. 17, p. 2010041, 2021.

[35] K. M. Pelzer, L. Cheng, and L. A. Curtiss, "Effects of functional groups in redox-active organic molecules: A high-throughput screening approach," *The Journal of Physical Chemistry C*, vol. 121, no. 1, pp. 237–245, 2017.

[36] O. Zandi and T. W. Hamann, "The potential versus current state of water splitting with hematite," *Physical Chemistry Chemical Physics*, vol. 17, no. 35, pp. 22 485–22 503, 2015.

[37] S. Wren and D. Donaldson, "How does deposition of gas phase species affect ph at frozen salty interfaces?" *Atmospheric Chemistry and Physics*, vol. 12, no. 21, pp. 10 065–10 073, 2012.

[38] S. Wang, G. Wang, X. Che, S. Wang, C. Li, D. Li, Y. Zhang, Q. Dong, and J. Qiu, "Enhancing the capacitive deionization performance of namno 2 by interface engineering and redox-reaction," *Environmental Science: Nano*, vol. 6, no. 8, pp. 2379–2388, 2019.

[39] Q. K. Wyatt and M. J. Young, "Pulsed electrodeposition of ultrathin polyaniline films and mechanistic understanding of their anion-mediated electrochemical behavior," *Journal of The Electrochemical Society*, vol. 167, no. 11, p. 110548, 2020.

[40] K. M. Barcelos, K. S. Oliveira, and L. A. Ruotolo, "Insights on the role of interparticle porosity and electrode thickness on capacitive deionization performance for desalination," *Desalination*, vol. 492, p. 114594, 2020.

[41] X. Li, J. Liu, X. Meng, Y. Tang, M. N. Banis, J. Yang, Y. Hu, R. Li, M. Cai, and X. Sun, "Significant impact on cathode performance of lithium-ion batteries by precisely controlled metal oxide nanocoatings via atomic layer deposition," *Journal of Power Sources*, vol. 247, pp. 57–69, 2014.

[42] L. I. Krishtalik, "ph-dependent redox potential: how to use it correctly in the activation energy analysis," *Biochimica et Biophysica Acta (BBA)-Bioenergetics*, vol. 1604, no. 1, pp. 13–21, 2003.

[43] J. H. Shim, S. Kang, S.-W. Cha, W. Lee, Y. B. Kim, J. S. Park, T. M. Guer, F. B. Prinz, C.-C. Chao, and J. An, "Atomic layer deposition of thin-film ceramic electrolytes for high-performance fuel cells," *Journal of Materials Chemistry A*, vol. 1, no. 41, pp. 12 695–12 705, 2013.

[44] R. W. Johnson, A. Hultqvist, and S. F. Bent, "A brief review of atomic layer deposition: from fundamentals to applications," *Materials today*, vol. 17, no. 5, pp. 236–246, 2014.

[45] P. Sundberg and M. Karppinen, "Organic and inorganic–organic thin film structures by molecular layer deposition: A review," *Beilstein journal of nanotechnology*, vol. 5, no. 1, pp. 1104–1136, 2014.

[46] S. E. Atanasov, M. D. Losego, B. Gong, E. Sachet, J.-P. Maria, P. S. Williams, and G. N. Parsons, "Highly conductive and conformal poly(3,4-ethylenedioxythiophene) (pedot) thin films via oxidative molecular layer deposition," *Chemistry of Materials*, vol. 26, no. 11, pp. 3471–3478, 2014. [Online]. Available: https://doi.org/10.1021/cm500825b

[47] B. Winther-Jensen, O. Winther-Jensen, M. Forsyth, and D. R. MacFarlane, "High rates of oxygen reduction over a vapor phase–polymerized pedot electrode," *Science*, vol. 321, no. 5889, pp. 671–674, 2008.

[48] J.-S. Kim and G. N. Parsons, "Nanopatterned area-selective vapor deposition of pedot on sio2 vs si-h: Improved selectivity using chemical vapor deposition vs molecular layer deposition," *Chemistry of Materials*, vol. 33, no. 23, pp. 9221–9230, 2021.

[49] A. Kurek, P. G. Gordon, S. Karle, A. Devi, and S. T. Barry, "Recent advances using guanidinate ligands for chemical vapour deposition (cvd) and atomic layer deposition (ald) applications," *Australian Journal of Chemistry*, vol. 67, no. 7, pp. 989–996, 2014.

[50] X. Wang, X. Zhang, L. Sun, D. Lee, S. Lee, M. Wang, J. Zhao, Y. Shao-Horn, M. Dincă, T. Palacios *et al.*, "High electrical conductivity and carrier mobility in ocvd pedot thin films by engineered crystallization and acid treatment," *Science Advances*, vol. 4, no. 9, p. eaat5780, 2018.

[51] J. B. You, S. Y. Kim, Y. J. Park, Y. G. Ko, and S. G. Im, "A vapor-phase deposited polymer film to improve the adhesion of electroless-deposited copper layer onto various kinds of substrates," *Langmuir*, vol. 30, no. 3, pp. 916–921, 2014.

[52] M. S. Newman and P. F. Beal III, "An improved wolff rearrangement in homogeneous medium1," *Journal of the American Chemical Society*, vol. 72, no. 11, pp. 5163–5165, 1950.

[53] M. Nomura, M. Miyake, H. Sakashita, and S. Kikkawa, "Hydrogenation of yūbari coal coated with zncl2-mcln (cucl, crcl3 and mocl5) catalyst melts," *Fuel*, vol. 61, no. 1, pp. 18–20, 1982.

[54] X. Zhang, Y. Tang, F. Zhang, and C. S. Lee, *Adv. Energy Mater.*, vol. 6, p. 1502588, 2016. [Online]. Available: https://doi.org/10.1002/aenm.201502588

[55] M. Sheng, F. Zhang, B. Ji, X. Tong, and Y. Tang, *Adv. Energy Mater.*, vol. 7, p. 1601963, 2017. [Online]. Available: https://doi.org/10.1002/aenm.201601963

[56] B. Ji, F. Zhang, X. Song, and Y. Tang, *Adv. Mater.*, vol. 29, p. 1700519, 2017. [Online]. Available: https://doi.org/10.1002/adma.201700519

[57] M. Wang, C. Jiang, S. Zhang, X. Song, Y. Tang, and H. M. Cheng, *Nat. Chem.*, vol. 10, p. 667, 2018. [Online]. Available: https://doi.org/10.1038/s41557-018-0045-4

[58] M. E. Suss, S. Porada, X. Sun, P. M. Biesheuvel, J. Yoon, and V. Presser, *Energy Environ. Sci.*, vol. 8, p. 2296, 2015. [Online]. Available: https://doi.org/10.1039/C5EE00519A

[59] S. Porada, R. Zhao, A. V. D. Wal, V. Presser, and P. M. Biesheuvel, *Prog. Mater Sci.*, vol. 58, p. 1388, 2013. [Online]. Available: https://doi.org/10.1016/j.pmatsci.2013.03.005

[60] M. Pasta, C. D. Wessells, Y. Cui, and F. L. Mantia, *Nano Lett.*, vol. 12, p. 839, 2012. [Online]. Available: https://doi.org/10.1021/nl203889e

[61] J. M. Wallas, M. J. Young, H. Sun, and S. M. George, *J. Electrochem. Soc.*, vol. 165, p. A2330, 2018. [Online]. Available: https://doi.org/10.1149/2.0751810jes

[62] M. J. Young, T. Kiryutina, N. M. Bedford, T. J. Woehl, and C. U. Segre, *Sci. Rep.*, vol. 9, p. 1, 2019. [Online]. Available: https://doi.org/10.1038/s41598-018-37186-2

[63] M. E. E. Alahi, S. C. Mukhopadhyay, and L. Burkitt, *Sensors Actuators, B Chem.*, vol. 259, p. 753, 2018. [Online]. Available: https://doi.org/10.1016/j.snb.2017.12.104

[64] E. C. Venancio, P. C. Wang, and A. G. MacDiarmid, *Synth. Met.*, vol. 156, p. 357, 2006. [Online]. Available: https://doi.org/10.1016/j.synthmet.2005.08.035

[65] S. Sharma and A. Bhattacharya, *Appl. Water Sci.*, vol. 7, p. 1043, 2017. [Online]. Available: https://doi.org/10.1007/s13201-016-0455-7

[66] J. M. Baker and T. J. Griffis, *J. Environ. Qual.*, vol. 46, p. 1528, 2017. [Online]. Available: https://doi.org/10.2134/jeq2017.05.0215

[67] G. Liao, Q. Li, and Z. Xu, *Prog. Org. Coatings*, vol. 126, p. 35, 2019. [Online]. Available: https://doi.org/10.1016/j.porgcoat.2018.10.018

[68] P. J. Hall, M. Mirzaeian, S. I. Fletcher, F. B. Sillars, A. J. R. Rennie, G. O. Shitta-Bey, G. Wilson, A. Cruden, and R. Carter, *Energy Environ. Sci.*, vol. 3, p. 1238, 2010. [Online]. Available: https://doi.org/10.1039/c0ee00004c

[69] J. Zang, S.-J. Bao, C. M. Li, H. Bian, X. Cui, Q. Bao, C. Q. Sun, J. Guo, and K. Lian, *J. Phys. Chem. C*, vol. 112, p. 14843, 2008. [Online]. Available: https://doi.org/10.1021/jp8049558

[70] C. Peng, D. Hu, and G. Z. Chen, *Chem. Commun.*, vol. 47, p. 4105, 2011. [Online]. Available: https://doi.org/10.1039/c1cc10675a

[71] K. D. Fong, T. Wang, and S. K. Smoukov, *Sustain. Energy Fuels*, vol. 1, p. 1857, 2017. [Online]. Available: https://doi.org/10.1039/C7SE00339K

[72] M. Kim, C. Lee, and J. Jang, *Adv. Funct. Mater.*, vol. 24, p. 2489, 2014. [Online]. Available: https://doi.org/10.1002/adfm.201303282

[73] J. Ma *et al.*, *J. Electroanal. Chem.*, vol. 835, p. 346, 2019. [Online]. Available: https://doi.org/10.1016/j.jelechem.2018.12.025

[74] J. Zhao, L. Sun, Q. Chen, H. Lu, and J. Wang, *J. Memb. Sci.*, vol. 582, p. 211, 2019. [Online]. Available: https://doi.org/10.1016/j.memsci.2019.03.043

[75] S. F. Evans, M. R. Ivancevic, D. J. Wilson, Z. D. Hood, S. P. Adhikari, A. K. Naskar, C. Tsouris, and M. P. Paranthaman, *Desalination*, vol. 464, p. 25, 2019. [Online]. Available: https://doi.org/10.1016/j.desal.2019.04.002

[76] X. Wang, Z. Li, J. Zhao, T. Xiao, and X. Wang, *J. Alloys Compd.*, vol. 781, p. 101, 2019. [Online]. Available: https://doi.org/10.1016/j.jallcom.2018.12.060

[77] X. Wang, J. Zhao, and Z. Li, *J. Nanopart. Res.*, vol. 21, p. 1, 2019. [Online]. Available: https://doi.org/10.1007/s11051-018-4445-6

[78] V. V. Abalyaeva and O. N. Efimov, *Russ. J. Electrochem.*, vol. 55, p. 953, 2019. [Online]. Available: https://doi.org/10.1134/S1023193519100021

[79] J. Xing, M. Liao, C. Zhang, M. Yin, D. Li, and Y. Song, *Phys. Chem. Chem. Phys.*, vol. 19, p. 14030, 2017. [Online]. Available: https://doi.org/10.1039/C7CP02016C

[80] B. Begum, *Mater. Int.*, vol. 2, p. 054, 2020. [Online]. Available: https://doi.org/10.33263/Materials21.054061

[81] M. Zhang, Q. Zhou, J. Chen, X. Yu, L. Huang, Y. Li, C. Li, and G. Shi, *Energy Environ. Sci.*, vol. 9, p. 2005, 2016. [Online]. Available: https://doi.org/10.1039/C6EE00615A

[82] J. S. Shayeh, P. Norouzi, and M. R. Ganjali, *Russ. J. Electrochem.*, vol. 52, p. 933, 2016. [Online]. Available: https://doi.org/10.1134/S1023193516100128

[83] M. J. Young, M. Neuber, A. C. Cavanagh, H. Sun, C. B. Musgrave, and S. M. George, *J. Electrochem. Soc.*, vol. 162, p. A2753, 2015. [Online]. Available: https://doi.org/10.1149/2.0671514jes

[84] F. F. Runge, *Ann. der Phys. und Chemie*, vol. 107, p. 65, 1834. [Online]. Available: https://doi.org/10.1002/andp.18341070502

[85] H. Letheby, *J. Chem. Soc.*, vol. 15, p. 161, 1862. [Online]. Available: https://doi.org/10.1039/JS8621500161

[86] N. A. Abdul-Manaf, W. Y. W. Yusoff, S. Z. N. Demon, N. A. Shaari, A. Shamshuddin, and N. S. Mohamed, *Mater. Res. Express*, vol. 6, p. 1, 2019. [Online]. Available: https://doi.org/10.1088/2053-1591/ab0259

[87] D. E. Stilwell, *J. Electrochem. Soc.*, vol. 135, p. 2491, 1988. [Online]. Available: https://doi.org/10.1149/1.2095364

[88] G. Ciric-Marjanovic, *Synth. Met.*, vol. 177, p. 1, 2013. [Online]. Available: https://doi.org/10.1016/j.synthmet.2013.06.004

[89] A. G. Macdiarmid, J. C. Chiang, A. F. Richter, and A. J. Epstein, *Synth. Met.*, vol. 18, p. 285, 1987. [Online]. Available: https://doi.org/10.1016/0379-6779(87)90893-9

[90] C. Dalmolin, S. C. Canobre, S. R. Biaggio, R. C. Rocha-Filho, and N. Bocchi, *J. Electroanal. Chem.*, vol. 578, p. 9, 2005. [Online]. Available: https://doi.org/10.1016/j.jelechem.2004.12.011

[91] J. Huang and R. B. Kaner, *Chem. Commun.*, vol. 56, p. 367, 2006. [Online]. Available: https://doi.org/10.1039/B510956F

[92] Q. Huang, X. Wang, J. Li, C. Dai, S. Gamboa, and P. J. Sebastian, *J. Power Sources*, vol. 164, p. 425, 2007. [Online]. Available: https://doi.org/10.1016/j.jpowsour.2006.09.066

[93] X. P. Chen, Q. H. Liang, J. K. Jiang, C. K. Y. Wong, S. Y. Y. Leung, H. Y. Ye, D. G. Yang, and T. L. Ren, *Sci. Rep.*, vol. 6, p. 1, 2016. [Online]. Available: https://doi.org/10.1038/s41598-016-0001-8

[94] H. A. Al-Attar, Q. H. Al-Alawina, and A. P. Monkman, *Thin Solid Films*, vol. 429, p. 286, 2003. [Online]. Available: https://doi.org/10.1016/S0040-6090(03)00279-7

[95] U. Latif, S. Can, O. Hayden, P. Grillberger, and F. L. Dickert, *Sensors Actuators B. Chem.*, vol. 176, p. 825, 2013. [Online]. Available: https://doi.org/10.1016/j.snb.2012.09.064

[96] F. Paquin, J. Rivnay, A. Salleo, N. Stingelin, and C. Silva, *J. Mater. Chem. C*, vol. 3, p. 10715, 2015. [Online]. Available: https://doi.org/10.1039/C5TC02043C

[97] N. C. Maile, S. K. Shinde, K. S. Patil, A. V. Fulari, A. Shahzad, D. S. Lee, and V. J. Fulari, *SN Appl. Sci.*, vol. 1, p. 1, 2019. [Online]. Available: https://doi.org/10.1007/s42452-019-1403-6

[98] P. R. Deshmukh, S. V. Patil, R. N. Bulakhe, S. D. Sartale, and C. D. Lokhande, *Mater. Today Commun.*, vol. 8, p. 205, 2016. [Online]. Available: https://doi.org/10.1016/j.mtcomm.2016.07.002

[99] D. Rehnlund, C. Ihrfors, J. Maibach, and L. Nyholm, *Mater. Today*, vol. 21, p. 1010, 2018. [Online]. Available: https://doi.org/10.1016/j.mattod.2018.08.003

[100] S. Bhadra, D. Khastgir, N. K. Singha, and J. H. Lee, *Prog. Polym. Sci.*, vol. 34, p. 783, 2009. [Online]. Available: https://doi.org/10.1016/j.progpolymsci.2009.04.003

[101] H. Karami, M. G. Asadi, and M. Mansoori, *Electrochim. Acta*, vol. 61, p. 154, 2012. [Online]. Available: https://doi.org/10.1016/j.electacta.2011.11.097

[102] H. D. Tran, J. M. D'Arcy, Y. Wang, P. J. Beltramo, V. A. Strong, and R. B. Kaner, *J. Mater. Chem.*, vol. 21, p. 3534, 2011. [Online]. Available: https://doi.org/10.1039/C0JM02699A

[103] R. Memming, *Semiconductor Electrochemistry*. Wiley-VCH Verlag GmbH Co. KGaA, 2015.

[104] M. J. Young, A. M. Holder, and C. B. Musgrave, *Adv. Funct. Mater.*, vol. 28, p. 1803439, 2018. [Online]. Available: https://doi.org/10.1002/adfm.201803439

[105] J. Stejskal and R. G. Gilbert, *Pure Appl. Chem.*, vol. 74, p. 857, 2002. [Online]. Available: https://doi.org/10.1351/pac200274050857

[106] R. Borjas and D. A. Buttry, *J. Electroanal. Chem. Interfacial Electrochem.*, vol. 280, p. 73, 1990. [Online]. Available: https://doi.org/10.1016/0022-0728(90)87085-X

[107] T. W. Schneider and D. A. Buttry, *J. Am. Chem. Soc.*, vol. 115, p. 12391, 1993. [Online]. Available: https://doi.org/10.1021/ja00079a021

[108] H. Gul, A. U. H. A. Shah, U. Krewer, and S. Bilal, *Nanomaterials*, vol. 10, p. 118, 2020. [Online]. Available: https://doi.org/10.3390/nano10010118

[109] S. Bilal, B. Begum, S. Gul, and A. U. H. A. Shah, *Synth. Met.*, vol. 235, p. 1, 2018. [Online]. Available: https://doi.org/10.1016/j.synthmet.2017.11.004

[110] M. Iram, C. Guo, H. Liu, and A. Ishfaq, *J. Exp. Nanosci.*, vol. 7, p. 27, 2012. [Online]. Available: https://doi.org/10.1080/17458080.2010.498123

[111] M. Boota and Y. Gogotsi, *Adv. Energy Mater.*, vol. 9, p. 1802917, 2019. [Online]. Available: https://doi.org/10.1002/aenm.201802917

[112] Q. Cui, H. Mi, J. Qiu, C. Yu, and Z. Zhao, *J. Mater. Res.*, vol. 29, p. 2408, 2014. [Online]. Available: https://doi.org/10.1557/jmr.2014.263

[113] X. H. Xia, J. P. Tu, J. Zhang, X. L. Wang, W. K. Zhang, and H. Huang, *Nanotechnology*, vol. 19, p. 465701, 2008. [Online]. Available: https://doi.org/10.1088/0957-4484/19/46/465701

[114] E. Song and J.-W. Choi, *Nanomaterials*, vol. 3, p. 498, 2013. [Online]. Available: https://doi.org/10.3390/nano3030498

[115] Y. Wang and K. Levon, *Macromol. Symp.*, vol. 317–318, p. 240, 2012. [Online]. Available: https://doi.org/10.1002/masy.201200008

[116] D. Geethalakshmi, N. Muthukumarasamy, and R. Balasundaraprabhu, *Optik (Stuttg).*, vol. 125, p. 1307, 2014. [Online]. Available: https://doi.org/10.1016/j.ijleo.2013.08.014

[117] I. Rahayu, D. R. Eddy, A. R. Novianty, Rukiah, A. Anggreni, H. Bahti, and S. Hidayat, *IOP Conf. Ser. Mater. Sci. Eng.*, 2019. [Online]. Available: https://doi.org/10.1088/1757-899X/509/1/012051

[118] H. F. Alesary, H. K. Ismail, A. F. Khudhair, and M. Q. Mohammed, *Orient. J. Chem.*, vol. 34, p. 2525, 2018. [Online]. Available: https://doi.org/10.13005/ojc/340539

[119] N. Su, *Polymers (Basel).*, vol. 7, p. 1599, 2015. [Online]. Available: https://doi.org/10.3390/polym7091473

[120] Z. Yang, H. Peng, W. Wang, and T. Liu, *J. Appl. Polym. Sci.*, vol. 116, p. 2658, 2010. [Online]. Available: https://doi.org/10.1002/app.31787

[121] R. Prakash, *J. Appl. Polym. Sci.*, vol. 83, p. 378, 2002. [Online]. Available: https://doi.org/10.1002/app.10025

[122] Y. H. Chen, J. Y. Wu, and Y. C. Chung, *Biosens. Bioelectron.*, vol. 22, p. 489, 2006. [Online]. Available: https://doi.org/10.1016/j.bios.2006.08.001

[123] H. Zhu, S. Peng, and W. Jiang, *Sci. World J.*, vol. 2013, p. 1, 2013. [Online]. Available: https://doi.org/10.1155/2013/940153

[124] J. M. D'Arcy, H. D. Tran, V. C. Tung, A. K. Tucker-Schwartz, R. P. Wong, Y. Yang, and R. B. Kaner, *Proc. Natl. Acad. Sci. U. S. A.*, vol. 107, p. 19673, 2010. [Online]. Available: https://doi.org/10.1073/pnas.1008595107

[125] L. Duić and Z. Mandić, *J. Electroanal. Chem.*, vol. 335, p. 207, 1992. [Online]. Available: https://doi.org/10.1016/0022-0728(92)80243-W

[126] S. Bilal, A. Akbar, and A. U. H. A. Shah, *Polymers (Basel).*, vol. 11, p. 1, 2019. [Online]. Available: https://doi.org/10.3390/polym11081346

[127] L. Nyholm and L. M. Peter, *J. Chem. Soc. Faraday Trans.*, vol. 90, p. 149, 1994. [Online]. Available: https://doi.org/10.1039/ft9949000149

[128] S. J. Choi and S. M. Park, *J. Electrochem. Soc.*, vol. 149, p. 26, 2002. [Online]. Available: https://doi.org/10.1149/1.1432675

[129] A. Khatoon, M. Khalid, and F. Mohammad, *J. Appl. Polym. Sci.*, vol. 108, p. 3769, 2008. [Online]. Available: https://doi.org/10.1002/app.28033

[130] K. Kanamura, Y. Kawai, S. Yonezawa, and Z. Takehara, *J. Phys. Chem.*, vol. 98, p. 2174, 1994. [Online]. Available: https://doi.org/10.1021/j100059a034

[131] M. M. Ayad and E. A. Zaki, *Sci. Technol. Adv. Mater.*, vol. 9, p. 1, 2008. [Online]. Available: https://doi.org/10.1088/1468-6996/9/1/015007

[132] C. Barbero, M. C. Miras, O. Haas, and R. Kötz, *J. Electroanal. Chem.*, vol. 310, p. 437, 1991. [Online]. Available: https://doi.org/10.1016/0022-0728(91)85280-3

[133] S. L. G. Lissy, S. Pitchumani, and K. Jayakumar, *Mater. Chem. Phys.*, vol. 76, p. 143, 2002. [Online]. Available: https://doi.org/10.1016/S0254-0584(01)00512-0

[134] W. C. Chen, T. C. Wen, and A. Gopalan, *Synth. Met.*, vol. 130, p. 61, 2002. [Online]. Available: https://doi.org/10.1016/S0379-6779(02)00111-X

[135] J. M. Nielsen, A. W. Adamson, and J. W. Cobble, *J. Am. Chem. Soc.*, vol. 74, p. 446, 1952. [Online]. Available: https://doi.org/10.1021/ja01122a050

[136] J. Kim, J. H. Kim, and K. Ariga, "Redox-active polymers for energy storage nanoarchitectonics," *Joule*, vol. 1, no. 4, p. 739–768, 2017. [Online]. Available: https://doi.org/10.1016/j.joule.2017.08.018

[137] Q. Li, Y. Zheng, D. Xiao, T. Or, R. Gao, Z. Li, M. Feng, L. Shui, G. Zhou, X. Wang, and Z. Chen, "Faradaic electrodes open a new era for capacitive deionization," *Adv. Sci.*, vol. 7, p. 2002213, 2020.

[138] M. M. Barsan, M. E. Ghica, and C. M. A. Brett, "Electrochemical sensors and biosensors based on redox polymer/carbon nanotube modified electrodes: A review," *Anal. Chim. Acta*, vol. 881, p. 1, 2015.

[139] K. D. Fong, T. Wang, and S. K. Smoukov, "Multidimensional performance optimization of conducting polymer-based supercapacitor electrodes," *Sustainable Energy Fuels*, vol. 1, p. 1857, 2017.

[140] S. Machida, S. Miyata, and A. Techagumpuch, "Chemical synthesis of highly electrically conductive polypyrrole," *Synth. Met.*, vol. 31, p. 311, 1989.

[141] C. O. Yoon, M. Reghu, D. Moses, A. J. Heeger, Y. Cao, T. A. Chen, X. Wu, and R. D. Rieke, "Hopping transport in doped conducting polymers in the insulating regime near the

metal-insulator boundary: Polypyrrole, polyaniline and polyalkylthiophenes," *Synth. Met.*, vol. 75, p. 229, 1995.

[142] X. Wang, X. Zhang, L. Sun, D. Lee, S. Lee, M. Wang, J. Zhao, Y. Shao-Horn, M. Dincă, T. Palacios, and K. K. Gleason, "High electrical conductivity and carrier mobility in ocvd pedot thin films by engineered crystallization and acid treatment," *Sci. Adv.*, vol. 4, p. eaat5780, 2018.

[143] J. P. Lock, S. G. Im, and K. K. Gleason, "Oxidative chemical vapor deposition of electrically conducting poly(3,4-ethylenedioxythiophene) films," *Macromolecules*, vol. 39, p. 5326, 2006.

[144] M. Pasta, C. D. Wessells, Y. Cui, and F. Mantia, "A desalination battery," *Nano Lett.*, vol. 12, p. 839, 2012.

[145] J. Lee, S. Kim, and J. Yoon, "Rocking chair desalination battery based on prussian blue electrodes," *ACS Omega*, vol. 2, p. 1653, 2017.

[146] S. Dühnen, R. Nölle, J. Wrogemann, M. Winter, and T. Placke, "Reversible anion storage in a metal-organic framework for dual-ion battery systems," *J. Electrochem. Soc.*, vol. 166, p. A5474, 2019.

[147] V. K. Davis, C. M. Bates, K. Omichi, B. M. Savoie, N. Momčilović, Q. Xu, W. J. Wolf, M. A. Webb, K. J. Billings, N. H. Chou, S. Alayoglu, R. K. McKenney, I. M. Darolles, N. G. Nair, A. Hightower, D. Rosenberg, M. Ahmed, C. J. Brooks, T. F. Miller, R. H. Grubbs, and S. C. Jones, "Room-temperature cycling of metal fluoride electrodes: Liquid electrolytes for high-energy fluoride ion cells," *Science*, vol. 362, p. 1144, 2018.

[148] F. F. Runge, "Ueber einige produkte der steinkohlendestillation," *Ann. Phys. Chem.*, vol. 107, p. 65, 1834.

[149] H. Letheby, "On the production of a blue substance by the electrolysis of sulphate of aniline," *J. Chem. Soc.*, vol. 15, p. 161, 1862.

[150] Y. Tian, G. Zeng, A. Rutt, T. Shi, H. Kim, J. Wang, J. Koettgen, Y. Sun, B. Ouyang, T. Chen, Z. Lun, Z. Rong, K. Persson, and G. Ceder, "Promises and challenges of next-generation "beyond li-ion" batteries for electric vehicles and grid decarbonization," *Chem. Rev.*, vol. 121, p. 1623, 2021.

[151] M. S. Whittingham, "Special editorial perspective: Beyond li-ion battery chemistry," *Chemical Reviews*, vol. 120, no. 14, p. 6328–6330, 2020.

[152] G. Zotti, "Doping-level dependence of conductivity in polypyrroles and polythiophenes," *Synth. Met.*, vol. 97, p. 267, 1998.

[153] E. R. Holland, S. J. Pomfret, P. N. Adams, and A. P. Monkman, "Conductivity studies of polyaniline doped with csa," *J. Phys.: Condens. Matter*, vol. 8, p. 2991, 1996.

[154] C. Peng, D. Hu, and G. Z. Chen, "Theoretical specific capacitance based on charge storage mechanisms of conducting polymers: Comment on 'vertically oriented arrays of polyaniline nanorods and their super electrochemical properties," *Chem. Commun.*, vol. 47, p. 4105, 2011.

[155] M. M. Ayad and E. A. Zaki, "Quartz crystal microbalance and spectroscopy measurements for acid doping in polyaniline films," *Sci. Technol. Adv. Mater.*, vol. 9, p. 015007, 2008.

[156] A. Khatoon, M. Khalid, and F. Mohammad, "Preparation and electroanalytical characterization of polyaniline: Polyacrylonitrile composite films," *J. Appl. Polym. Sci.*, vol. 108, p. 3769, 2008.

[157] K. Kanamura, Y. Kawai, S. Yonezawa, and Z. Takehara, "Diffusion behavior of anions in polyaniline during electrochemical undoping. 2. effect of the preparation conditions of polyaniline on the diffusion coefficient of bf4," *J. Phys. Chem. A*, vol. 98, p. 2174, 1994.

[158] Y. Wei, X. Tang, Y. Sun, and W. W. Focke, "A study of the mechanism of aniline polymerization," *J. Polym. Sci., Part A: Polym. Chem.*, vol. 27, p. 2385, 1989.

[159] G. Ćirić Marjanović, "Recent advances in polyaniline research: Polymerization mechanisms, structural aspects, properties and applications," *Synth. Met.*, vol. 177, p. 1, 2013.

[160] X. Chen, E. Pomerantseva, K. Gregorczyk, R. Ghodssi, and G. Rubloff, "Cathodic ald v2o5 thin films for high-rate electrochemical energy storage," *RSC Advances*, vol. 3, no. 13, p. 4294, 2013. [Online]. Available: http://xlink.rsc.org/?DOI=c3ra23031g

[161] J. Huang and R. B. Kaner, "Nanofiber formation in the chemical polymerization of aniline: A mechanistic study," *Angew. Chem., Int. Ed.*, vol. 43, p. 5817, 2004.

[162] X. Zhang and S. K. Manohar, "Bulk synthesis of polypyrrole nanofibers by a seeding approach," *J. Am. Chem. Soc.*, vol. 126, p. 12714, 2004.

[163] M. A. Chougule, S. G. Pawar, P. R. Godse, R. N. Mulik, S. Sen, and V. B. Patil, "Synthesis and characterization of polypyrrole (ppy) thin films," *Soft Nanosci. Lett.*, vol. 01, p. 6, 2011.

[164] D. Verma and V. Dutta, "Novel microstructure in spin coated polyaniline thin films," *J. Phys.: Condens. Matter*, vol. 19, p. 186212, 2007.

[165] R. Gettler and M. J. Young, "Multimodal cell with simultaneous electrochemical quartz crystal microbalance and in operando spectroscopic ellipsometry to understand thin film electrochemistry," *Rev. Sci. Instrum.*, vol. 92, p. 053902, 2021.

[166] C. N. Sayre and D. M. Collard, "Electrooxidative deposition of polypyrrole and polyaniline on self-assembled monolayer modified electrodes," *Langmuir*, vol. 13, p. 714, 1997.

[167] A. Mohammadi, I. Lundström, O. Inganäs, and W. R. Salaneck, "Conducting polymers prepared by template polymerization: Polypyrrole," *Polymer*, vol. 31, p. 395, 1990.

[168] D. Bilger, S. Z. Homayounfar, and T. L. Andrew, "A critical review of reactive vapor deposition for conjugated polymer synthesis," *J. Mater. Chem. C*, vol. 7, p. 7159, 2019.

[169] D. Bhattacharyya, R. M. Howden, D. C. Borrelli, and K. K. Gleason, "Vapor phase oxidative synthesis of conjugated polymers and applications," *J. Polym. Sci., Part B: Polym. Phys.*, vol. 50, p. 1329, 2012.

[170] J. E. Lee, Y. Lee, K. J. Ahn, J. Huh, H. W. Shim, G. Sampath, W. Im, Y. bin Huh, and H. il Yoon, "Role of co-vapors in vapor deposition polymerization," *Sci. Rep.*, vol. 5, p. 8420, 2015.

[171] Y. Y. Smolin, M. Soroush, and K. K. S. Lau, "Oxidative chemical vapor deposition of polyaniline thin films," *Beilstein J. Nanotechnol.*, vol. 8, p. 1266, 2017.

[172] Y. Cheng, A. Khlyustova, P. Chen, and R. Yang, "Kinetics of all-dry free radical polymerization under nanoconfinement," *Macromolecules*, vol. 53, p. 10699, 2020.

[173] S. E. Atanasov, M. D. Losego, B. Gong, E. Sachet, J. P. Maria, P. S. Williams, and G. N. Parsons, "Highly conductive and conformal poly(3,4-ethylenedioxythiophene) (pedot) thin films via oxidative molecular layer deposition," *Chem. Mater.*, vol. 26, p. 3471, 2014.

[174] D. H. Kim, S. E. Atanasov, P. Lemaire, K. Lee, and G. N. Parsons, "Platinum-free cathode for dye-sensitized solar cells using poly(3,4-ethylenedioxythiophene) (pedot) formed via oxidative molecular layer deposition," *ACS Appl. Mater. Interfaces*, vol. 7, p. 3866, 2015.

[175] S. M. George, "Atomic layer deposition: An overview," *Chemical Reviews*, vol. 110, no. 1, p. 111–131, Jan 2010.

[176] R. W. Johnson, A. Hultqvist, and S. F. Bent, "A brief review of atomic layer deposition: From fundamentals to applications," *Mater. Today*, vol. 17, p. 236, 2014.

[177] R. L. Puurunen, "Surface chemistry of atomic layer deposition: A case study for the trimethylaluminum/water process," *Journal of Applied Physics*, vol. 97, no. 121301, p. 1–52, 2005.

[178] T. Yoshimura, S. Tatsuura, and W. Sotoyama, "Polymer films formed with monolayer growth steps by molecular layer deposition," *Applied Physics Letters*, vol. 59, no. 4, p. 482–484, 1991.

[179] N. M. Adamczyk, A. A. Dameron, and S. M. George, "Molecular layer deposition of poly(p-phenylene terephthalamide) films using terephthaloyl chloride and p-phenylenediamine," *Langmuir*, vol. 24, p. 2081, 2008.

[180] Y. Du and S. M. George, "Molecular layer deposition of nylon 66 films examined using in situ ftir spectroscopy," *J. Phys. Chem. C*, vol. 111, p. 8509, 2007.

[181] M. J. Young, T. Kiryutina, N. M. Bedford, T. J. Woehl, and C. U. Segre, "Discovery of anion insertion electrochemistry in layered hydroxide nanomaterials," *Sci. Rep.*, vol. 9, p. 2462, 2019.

[182] A. C. Arulrajan, D. L. Ramasamy, M. Sillanpää, A. van der Wal, P. M. Biesheuvel, S. Porada, and J. E. Dykstra, "Exceptional water desalination performance with anion-selective electrodes," *Adv. Mater.*, vol. 31, p. 1806937, 2019.

[183] S. A. Gregory, R. Hanus, A. Atassi, J. M. Rinehart, J. P. Wooding, A. K. Menon, M. D. Losego, G. J. Snyder, and S. K. Yee, "Quantifying charge carrier localization in chemically doped semiconducting polymers," *Nat. Mater.*, vol. 20, p. 1414, 2021.

[184] J. W. Elam, M. D. Groner, and S. M. George, "Viscous flow reactor with quartz crystal microbalance for thin film growth by atomic layer deposition," *Rev. Sci. Instrum.*, vol. 73, p. 2981, 2002.

[185] J. Stejskal and R. G. Gilbert, "Polyaniline. preparation of a conducting polymer (iupac technical report)," *Pure Appl. Chem.*, vol. 74, p. 857, 2002.

[186] H. Kaiser, K. Hamacher, R. Kulasekere, W. T. Lee, J. F. Ankner, B. DeFacio, P. F. Miceli, and D. L. Worcester, "Neutron inverse optics in layered materials," *Inverse Opt. III*, vol. 2241, p. 78, 1994.

[187] L. G. Parratt, "Surface studies of solids by total reflection of x-rays," *Physical Review*, vol. 95, no. 2, p. 359–369, Jul 1954. [Online]. Available: https://link.aps.org/doi/10.1103/PhysRev.95.359

[188] D. M. Piper, J. J. Travis, M. Young, S.-B. Son, S. C. Kim, K. H. Oh, S. M. George, C. Ban, and S.-H. Lee, "Reversible high-capacity si nanocomposite anodes for lithium-ion batteries enabled by molecular layer deposition," *Adv. Mater.*, vol. 26, p. 1596, 2014.

[189] B. Yoon, J. L. O'Patchen, D. Seghete, A. S. Cavanagh, and S. M. George, "Molecular layer deposition of hybrid organic-inorganic polymer films using diethylzinc and ethylene glycol," *Chem. Vap. Deposition*, vol. 15, p. 112, 2009.

[190] A. A. Volk, J.-S. Kim, J. Jamir, E. C. Dickey, and G. N. Parsons, "Oxidative molecular layer deposition of pedot using volatile antimony(v) chloride oxidant," *J. Vac. Sci. Technol. A*, vol. 39, p. 032413, 2021.

[191] S. Ghafourisaleh, G. Popov, M. Leskelä, M. Putkonen, and M. Ritala, "Oxidative mld of conductive pedot thin films with edot and recl5as precursors," *ACS Omega*, vol. 6, p. 17545, 2021.

[192] R. Goddard, O. Heinemann, and C. Krüger, "Pyrrole and a co-crystal of 1h- and 2h-1,2,3-triazole," *Acta Crystallogr., Sect. C: Cryst. Struct. Commun.*, vol. 53, p. 1846, 1997.

[193] P. Poodt, D. C. Cameron, E. Dickey, S. M. George, V. Kuznetsov, G. N. Parsons, F. Roozeboom, G. Sundaram, and A. Vermeer, "Spatial atomic layer deposition: A route towards further industrialization of atomic layer deposition," *J. Vac. Sci. Technol. A*, vol. 30, p. 010802, 2012.

[194] A. W. Weimer, "Particle atomic layer deposition," *J. Nanopart. Res.*, vol. 21, p. 9, 2019.

[195] A. F. Diaz, J. I. Castillo, J. A. Logan, and W.-Y. Lee, "Electrochemistry of conducting polypyrrole films," *J. Electroanal. Chem. Interfacial Electrochem.*, vol. 129, p. 115, 1981.

[196] J. J. L. Cascales and T. F. Otero, "Molecular dynamic simulation of the hydration and diffusion of chloride ions from bulk water to polypyrrole matrix," *J. Chem. Phys.*, vol. 120, p. 1951, 2004.

[197] B. Rajagopalan, B. Kim, S. H. Hur, I. K. Yoo, and J. S. Chung, "Redox synthesis of poly (p–phenylenediamine)–reduced graphene oxide for the improvement of electrochemical performance of lithium titanate in lithium–ion battery anode," *J. Alloys Compd.*, vol. 709, p. 248, 2017.

[198] C. S. Choi and H. Tachikawa, "Electrochemical behavior and characterization of polypyrrole-copper phthalocyanine tetrasulfonate thin film: Cyclic voltammetry and in situ raman spectroscopic investigation," *J. Am. Chem. Soc.*, vol. 112, p. 1757, 1990.

[199] M. J. Young, H.-D. Schnabel, A. M. Holder, S. M. George, and C. B. Musgrave, "Band diagram and rate analysis of thin film spinel limn2o4 formed by electrochemical conversion of ald-grown mno," *Adv. Funct. Mater.*, vol. 26, p. 7895, 2016.

[200] M. J. Young, M. Neuber, A. C. Cavanagh, H. Sun, C. B. Musgrave, and S. M. George, "Sodium charge storage in thin films of mno2 derived by electrochemical oxidation of mno atomic layer deposition films, supplementary material," *J. Electrochem. Soc.*, vol. 162, p. A2753, 2015.

[201] L. Z. Fan and J. Maier, "High-performance polypyrrole electrode materials for redox supercapacitors," *Electrochem. Commun.*, vol. 8, p. 937, 2006.

[202] V. Khomenko and E. Frackowiak, "Determination of the specific capacitance of conducting polymer / nanotubes composite electrodes using different cell configurations," vol. 50, p. 2499–2506, 2005.

[203] R. Prakash, "Electrochemistry of polyaniline: Study of the ph effect and electrochromism," *J. Appl. Polym. Sci.*, vol. 83, p. 378, 2002.

[204] N. Bartalucci, M. Bortoluzzi, F. Marchetti, G. Pampaloni, S. Schoch, and S. Zacchini, "Unusual activation pathways of amines in the reactions with molybdenum pentachloride," *New J. Chem.*, vol. 41, p. 4329, 2017.

[205] M. Hayatifar, F. Marchetti, G. Pampaloni, C. Pinzino, and S. Zacchini, "Reactions of molybdenum pentachloride with oxygen and nitrogen donor ligands," *Polyhedron*, vol. 61, p. 188, 2013.

[206]

[207] Q. K. Wyatt, M. Vaninger, N. C. Paranamana, T. W. Heitmann, H. Kaiser, and M. J. Young, "Oxidative molecular layer deposition of amine-containing conjugated polymer thin films," *ACS Applied Polymer Materials*, vol. 4, no. 8, pp. 6156–6168, 2022.

[208]

[209] J. Kim, J. H. Kim, and K. Ariga, "Redox-active polymers for energy storage nanoarchitectonics," *Joule*, vol. 1, p. 739, 2017.

[210] S. Sen and P. Sarkar, "A novel third-generation xanthine biosensor with enzyme modified glassy carbon electrode using electrodeposited mwcnt and nanogold polymer composite film," *RSC Adv.*, vol. 5, p. 95911, 2015.

[211] D. N. Bailey, D. M. Hercules, and D. K. Roe, "Electrochemistry and photopotentials of phenazine in methanol solutions," *J. Electrochem. Soc.*, vol. 116, p. 190, 1969.

[212] D. T. Sawyer and R. Y. Komai, "Electrochemistry of phenazine at a platinum electrode in aprotic solvents," *Anal. Chem.*, vol. 44, p. 715, 1972.

[213] M. Trchová and J. Stejskal, "Resonance raman spectroscopy of conducting polypyrrole nanotubes: Disordered surface versus ordered body," *J. Phys. Chem. A*, vol. 122, p. 9298, 2018.

[214] M. J. L. Santos, A. G. Brolo, and E. M. Girotto, "Study of polaron and bipolaron states in polypyrrole by in situ raman spectroelectrochemistry," *Electrochim. Acta*, vol. 52, p. 6141, 2007.

[215] C. M. Stuart, R. R. Frontiera, and R. A. Mathies, "Excited-state structure and dynamics of cis- and trans-azobenzene from resonance raman intensity analysis," *J. Phys. Chem. A*, vol. 111, p. 12072, 2007.

[216] C. Luo, O. Borodin, X. Ji, S. Hou, K. J. Gaskell, X. Fan, J. Chen, T. Deng, R. Wang, J. Jiang, and C. Wang, "Azo compounds as a family of organic electrode materials for alkali-ion batteries," *Proc. Natl. Acad. Sci. U.S.A.*, vol. 115, p. 2004, 2018.

[217] Y. Yang, F. Teng, L. Yu, Y. Liu, P. Song, and L. Xia, "Isomerization of p, p-diiodoazobenzene controlled by the surface plasmon-assisted reaction," *ACS Omega*, vol. 4, p. 7076, 2019.

[218] H. C. Bach and H. E. Hinderer, "Aromatic azopolymers with segments of extended conjugation," *Appl. Polym. Symp.*, vol. 2, p. 35, 1973.

[219] S. Han, Y. Cheng, S. Liu, C. Tao, A. Wang, W. Wei, H. Yu, and Y. Wei, "Selective oxidation of anilines to azobenzenes and azoxybenzenes by a molecular mo oxide catalyst," *Angew. Chem., Int. Ed.*, vol. 60, p. 6382, 2021.

[220] N. S. Yadavalli, D. Korolkov, J. F. Moulin, M. Krutyeva, and S. Santer, "Probing optomechanical stresses within azobenzene-containing photosensitive polymer films by a thin metal film placed above," *ACS Appl. Mater. Interfaces*, vol. 6, p. 11333, 2014.

[221] G. Ozaydin-Ince, A. M. Coclite, and K. K. Gleason, "Cvd of polymeric thin films: Applications in sensors, biotechnology, microelectronics/organic electronics, microfluidics, mems, composites and membranes," *Reports on Progress in Physics*, vol. 75, no. 1, Jan 2012.

[222] H. Tan, Y. Chu, X. Wu, W. J. Liu, D. W. Zhang, and S. J. Ding, "High-performance flexible gas sensors based on layer-by-layer assembled polythiophene thin films," *Chemistry of Materials*, vol. 33, no. 19, p. 7785–7794, Oct 2021. [Online]. Available: https://pubs.acs.org/doi/full/10.1021/acs.chemmater.1c02182

[223] Y. Ding, M. A. Invernale, and G. A. Sotzing, "Conductivity trends of pedot-pss impregnated fabric and the effect of conductivity on electrochromic textile," *ACS Applied Materials and Interfaces*, vol. 2, no. 6, p. 1588–1593, Jun 2010.

[224] A. Laforgue, "All-textile flexible supercapacitors using electrospun poly(3,4- ethylenedioxythiophene) nanofibers," *Journal of Power Sources*, vol. 196, no. 1, p. 559–564, Jan 2011.

[225] A. H. Brozena, C. J. Oldham, and G. N. Parsons, "Atomic layer deposition on polymer fibers and fabrics for multifunctional and electronic textiles," *Journal of Vacuum Science Technology A: Vacuum, Surfaces, and Films*, vol. 34, no. 1, p. 010801, 2016. [Online]. Available: http://dx.doi.org/10.1116/1.4938104

[226] S. M. George, A. A. Dameron, and B. Yoon, "Surface chemistry for molecular layer deposition of organic and hybrid organic-inorganic polymers," *Accounts of Chemical Research*, vol. 42, no. 4, p. 498–508, Apr 2009.

[227] Y. Y. Smolin, M. Soroush, and K. K. Lau, "Oxidative chemical vapor deposition of polyaniline thin films," *Beilstein Journal of Nanotechnology*, vol. 8, no. 1, p. 1266–1276, 2017.

[228] J. P. Lock, J. L. Lutkenhaus, N. S. Zacharia, S. G. Im, P. T. Hammond, and K. K. Gleason, "Electrochemical investigation of pedot films deposited via cvd for electrochromic applications," *Synthetic Metals*, vol. 157, no. 22–23, p. 894–898, 2007.

[229] S. G. Im and K. K. Gleason, "Systematic control of the electrical conductivity of poly(3,4-ethylenedioxythiophene) via oxidative chemical vapor deposition," *Macromolecules*, vol. 40, no. 18, p. 6552–6556, 2007.

[230] D. Bilger, S. Z. Homayounfar, and T. L. Andrew, "A critical review of reactive vapor deposition for conjugated polymer synthesis," *Journal of Materials Chemistry C*, vol. 7, no. 24, p. 7159–7174, 2019.

[231] A. A. Volk, J.-S. Kim, J. Jamir, E. C. Dickey, and G. N. Parsons, "Oxidative molecular layer deposition of pedot using volatile antimony(v) chloride oxidant," *Journal of Vacuum Science Technology A*, vol. 39, no. 3, p. 032413, 2021.

[232] S. Ghafourisaleh, G. Popov, M. Leskelä, M. Putkonen, and M. Ritala, "Oxidative mld of conductive pedot thin films with edot and recl5as precursors," *ACS Omega*, vol. 6, no. 27, p. 17545–17554, 2021.

[233] B. Rajagopalan, B. Kim, S. H. Hur, I. K. Yoo, and J. S. Chung, "Redox synthesis of poly (p–phenylenediamine)–reduced graphene oxide for the improvement of electrochemical performance of lithium titanate in lithium–ion battery anode," *Journal of Alloys and Compounds*, vol. 709, p. 248–259, 2017. [Online]. Available: https://www.researchgate.net/publication/315442839_Redox_synthesis_of_poly_p_-phenylenediamine-reduced_graphene_oxide_for_the_improvement_of_electrochemical_performance_of_lithium_titanate_in_lithium-ion_battery_anode

[234] K. D. Fong, T. Wang, and S. K. Smoukov, "Multidimensional performance optimization of conducting polymer-based supercapacitor electrodes," *Sustainable Energy Fuels*, vol. 1, no. 9, p. 1857–1874, 2017.

[235] Y. Tian, G. Zeng, A. Rutt, T. Shi, H. Kim, J. Wang, J. Koettgen, Y. Sun, B. Ouyang, T. Chen, Z. Lun, Z. Rong, K. Persson, and G. Ceder, "Promises and challenges of next-generation "beyond li-ion" batteries for electric vehicles and grid decarbonization," *Chemical Reviews*, vol. 121, no. 3, p. 1623–1669, 2021.

[236] H. Chelawat, S. Vaddiraju, and K. Gleason, "Conformal, conducting poly(3,4-ethylenedioxythiophene) thin films deposited using bromine as the oxidant in a completely dry oxidative chemical vapor deposition process," *Chemistry of Materials*, vol. 22, no. 9, p. 2864–2868, 2010.

[237] "Metal free conducting pedos, pedot, and their analogues via an unusual bromine-catalyzed polymerization," vol. 48.

[238] D. H. Kim, S. E. Atanasov, P. Lemaire, K. Lee, and G. N. Parsons, "Platinum-free cathode for dye-sensitized solar cells using poly(3,4-ethylenedioxythiophene) (pedot) formed via oxidative molecular layer deposition," *ACS Applied Materials and Interfaces*, vol. 7, no. 7, p. 3866–3870, 2015.

[239] Y. Lee, H. Sun, M. J. Young, and S. M. George, "Atomic layer deposition of metal fluorides using hf-pyridine as the fluorine precursor," *Chemistry of Materials*, vol. 28, no. 7, p. 2022–2032, 2016. [Online]. Available: http://www.scopus.com/inward/record.url?eid=2-s2.0-84964742006&partnerID=MN8TOARS

[240] J. W. Elam, M. D. Groner, and S. M. George, "Viscous flow reactor with quartz crystal microbalance for thin film growth by atomic layer deposition," *Review of Scientific Instruments*, vol. 73, no. 8, p. 2981–2987, 2002. [Online]. Available: http://scitation.aip.org/content/aip/journal/rsi/73/8/10.1063/1.1490410

[241] H. Jain and P. Poodt, "About the importance of purge time in molecular layer deposition of alucone films," *Dalton Transactions*, vol. 50, no. 17, p. 5807–5818, 2021.

[242] N. L. Weinberg and H. R. Weinberg, "Electrochemical oxidation of organic compounds," *Chemical Reviews*, vol. 68, no. 4, p. 449–523, 1968.

[243] M. Trchová and J. Stejskal, "Resonance raman spectroscopy of conducting polypyrrole nanotubes: Disordered surface versus ordered body," *Journal of Physical Chemistry A*, vol. 122, no. 48, p. 9298–9306, 2018.

[244] M. J. Santos, A. G. Brolo, and E. M. Girotto, "Study of polaron and bipolaron states in polypyrrole by in situ raman spectroelectrochemistry," *Electrochimica Acta*, vol. 52, no. 20, p. 6141–6145, 2007.

[245] L. Z. Fan and J. Maier, "High-performance polypyrrole electrode materials for redox supercapacitors," *Electrochemistry Communications*, vol. 8, no. 6, p. 937–940, 2006.

[246] F. F. Runge, "Ueber einige produkte der steinkohlendestillation," *Annalen der Physik und Chemie*, vol. 107, no. 5, p. 65–78, 1834.

[247] S. C. Rasmussen, "Early history of polypyrrole: the first conducting organic polymer," *Bull. Hist. Chem.*, vol. 40, no. 1, p. 45–55, 2015.

[248] L. Groenendaal, F. Jonas, D. Freitag, H. Pielartzik, and J. R. Reynolds, "Poly(3,4-ethylenedioxythiophene) and its derivatives: past, present, and future," *Advanced Materials*, vol. 12, no. 7, p. 481–494, 2000.

[249] F. Jonas and L. Schrader, "Conductive modifications of polymers with polypyrroles and polythiophenes," *Synthetic Metals*, vol. 41, no. 3, p. 831–836, 1991.

[250] H. Gerhard and J. Friedrich, "Poly(alkylenedioxythiophene)s - new, very stable conducting polymers," *Advanced Materials*, vol. 4, no. 2, p. 116–118, 1992.

[251] J. F. Ponder, A. K. Menon, R. R. Dasari, S. L. Pittelli, K. J. Thorley, S. K. Yee, S. R. Marder, and J. R. Reynolds, "Conductive, solution-processed dioxythiophene copolymers for thermoelectric and transparent electrode applications," *Advanced Energy Materials*, vol. 9, no. 24, p. 1–7, 2019.

[252] A. Elschner, *PEDOT: principles and applications of an intrinsically conductive polymer*. CRC Press, 2011.

[253]

[254] M. Dietrich, J. Heinze, G. Heywang, and F. Jonas, "Electrochemical and spectroscopic characterization of polyalkylenedioxythiophenes," *Journal of Electroanalytical Chemistry*, vol. 369, no. 1–2, p. 87–92, 1994.

[255] A. Mohammadi, I. Lundström, O. Inganäs, and W. R. Salaneck, "Conducting polymers prepared by template polymerization: polypyrrole," *Polymer*, vol. 31, no. 3, p. 395–399, 1990.

[256] D. Bhattacharyya, R. M. Howden, D. C. Borrelli, and K. K. Gleason, "Vapor phase oxidative synthesis of conjugated polymers and applications," *Journal of Polymer Science, Part B: Polymer Physics*, vol. 50, no. 19, p. 1329–1351, 2012.

[257] J. Kim, E. Kim, Y. Won, H. Lee, and K. Suh, "The preparation and characteristics of conductive poly(3,4-ethylenedioxythiophene) thin film by vapor-phase polymerization," *Synthetic Metals*, vol. 139, no. 2, p. 485–489, 2003.

[258] J. P. Lock, S. G. Im, and K. K. Gleason, "Oxidative chemical vapor deposition of electrically conducting poly(3,4-ethylenedioxythiophene) films," *Macromolecules*, vol. 39, no. 16, p. 5326–5329, 2006.

[259] S. M. George, B. Yoon, R. A. Hall, A. I. Abdulagatov, Z. M. Gibbs, Y. Lee, D. Seghete, and B. H. Lee, "Molecular layer deposition of hybrid organic – inorganic films," 2012.

[260]

[261] P. Moni, J. Lau, A. C. Mohr, T. C. Lin, S. H. Tolbert, B. Dunn, and K. K. Gleason, "Growth temperature and electrochemical performance in vapor-deposited poly(3,4-ethylenedioxythiophene)

thin films for high-rate electrochemical energy storage," *ACS Applied Energy Materials*, vol. 1, no. 12, p. 7093–7105, 2018.

[262] L. Zhang and T. L. Andrew, "Deposition dependent ion transport in doped conjugated polymer films: Insights for creating high-performance electrochemical devices," *Advanced Materials Interfaces*, vol. 4, no. 23, p. 1–9, 2017.

[263] D. M. Piper, J. J. Travis, M. Young, S.-B. S. B. Son, S. C. Kim, K. H. Oh, S. M. George, C. Ban, and S.-H. S. H. Lee, "Reversible high-capacity si nanocomposite anodes for lithium-ion batteries enabled by molecular layer deposition," *Advanced Materials*, vol. 26, p. 1596–1601, 2014. [Online]. Available: http://www.scopus.com/inward/record.url?eid=2-s2.0-84895930789&partnerID=MN8TOARS

[264]

[265] Y. Zhao and X. Sun, "Molecular layer deposition for energy conversion and storage," *ACS Energy Letters*, vol. 3, no. 4, p. 899–914, 2018.

[266]

[267] T. Kim, C. A. Gorski, and B. E. Logan, "Low energy desalination using battery electrode deionization," *Environmental Science and Technology Letters*, vol. 4, no. 10, p. 444–449, 2017.

[268] P. Kienzle, B. Maranville, K. O'Donovan, J. Ankner, N. Berk, and C. Majkrzak, "Refl1d," 2017. [Online]. Available: https://www.nist.gov/ncnr/reflectometry-software

[269]

[270] V. Singh and T. Kumar, "Study of modified pedot:pss for tuning the optical properties of its conductive thin films," *Journal of Science: Advanced Materials and Devices*, vol. 4, no. 4, p. 538–543, 2019.

[271] J. Hwang, I. Schwendeman, B. C. Ihas, R. J. Clark, M. Cornick, M. Nikolou, A. Argun, J. R. Reynolds, and D. B. Tanner, "In situ measurements of the optical absorption of dioxythiophene-based conjugated polymers," *Physical Review B - Condensed Matter and Materials Physics*, vol. 83, no. 19, p. 1–12, 2011.

[272] J. Hwang, D. B. Tanner, I. Schwendeman, and J. R. Reynolds, "Optical properties of nondegenerate ground-state polymers: Three dioxythiophene-based conjugated polymers," *Physical Review B - Condensed Matter and Materials Physics*, vol. 67, no. 11, p. 10, 2003.

[273] L. Niu, C. Kvarnström, K. Fröberg, and A. Ivaska, "Electrochemically controlled surface morphology and crystallinity in poly(3,4-ethylenedioxythiophene) films," *Synthetic Metals*, vol. 122, no. 2, p. 425–429, 2001.

[274] K. E. Aasmundtveit, E. J. Samuelsen, L. A. Pettersson, O. Inganäs, T. Johansson, and R. Feidenhans'l, "Structure of thin films of poly(3,4-ethylenedioxythiophene)," *Synthetic Metals*, vol. 101, no. 1, p. 561–564, 1999.

[275] S. Garreau, G. Louarn, J. P. Buisson, G. Froyer, and S. Lefrant, "In situ spectroelectrochemical raman studies of poly(3,4-ethylenedioxythiophene) (pedt)," *Macromolecules*, vol. 32, no. 20, p. 6807–6812, 1999.

[276] R. Vidano, D. Fischbach, L. Willis, and T. Loehr, "Observation of raman band shifting with excitation wavelength for carbons and graphites," *Solid State Communications*, vol. 39, no. 2, p. 341–344, Jul 1981. [Online]. Available: https://linkinghub.elsevier.com/retrieve/pii/0038109881906864

[277]

[278] A. R. Hillman, S. J. Daisley, and S. Bruckenstein, "Kinetics and mechanism of the electrochemical p-doping of pedot," *Electrochemistry Communications*, vol. 9, no. 6, p. 1316–1322, 2007.

[279] R. A. Hillman, S. J. Daisley, and S. Bruckenstein, "Solvent effects on the electrochemical p-doping of pedot," *Physical Chemistry Chemical Physics*, vol. 9, no. 19, p. 2379–2388, 2007.

[280] M. J. Young, M. Neuber, A. C. Cavanagh, H. Sun, C. B. Musgrave, and S. M. George, "Sodium charge storage in thin films of mno2 derived by electrochemical oxidation of mno atomic layer deposition films, supplementary material," *Journal of The Electrochemical Society*, vol. 162, no. 14, p. A2753–A2761, Oct 2015. [Online]. Available: http://www.scopus.com/inward/record.url?eid=2-s2.0-84946033445&partnerID=MN8TOARS

[281] M. J. Young, H.-D. Schnabel, A. M. Holder, S. M. George, and C. B. Musgrave, "Band diagram and rate analysis of thin film spinel limn2o4 formed by electrochemical conversion of ald-grown mno," *Advanced Functional Materials*, vol. 26, no. 43, p. 7895–7907, Nov 2016. [Online]. Available: http://www.scopus.com/inward/record.url?eid=2-s2.0-84988589069&partnerID=MN8TOARS

[282]

[283] M. A. Hernández, J. A. Velasco, M. Asomoza, S. Solís, F. Rojas, and V. H. Lara, "Adsorption of benzene, toluene, and p-xylene on microporous sio2," *Industrial and Engineering Chemistry Research*, vol. 43, no. 7, p. 1779–1787, 2004.

[284]

VITA

Quinton K. Wyatt was born in Houston, Texas were they graduated from Cypress Creek High School in 2010 before moving to Springfield, Mo in 2012. In Springfield, they attended Evangel University, where they obtained his Bachelors of Science in Chemistry, in May of 2016. The following August they entered Missouri State Univeristy and in August 2018 received the degree of Master's of Science in Chemistry. They entered University of Missouri in 2018 to work towards obtaining Doctor of Philosophy in Chemistry, in December 2022.